sciendo Slovak Journal of Civil Engineering

Vol. 32, 2024, No. 2, 1 – 9
DOI: 10.2478/sjce-2024-0008

PANELS OF COLD-FORMED STEEL PROFILES: POSSIBILITY OF THEIR USE TO REPAIR WAR-DAMAGED LARGE-PANEL BUILDINGS

Volodymyr SEMKO[1*], Olena HRANKO[2], Rudolf ÁROCH[3]

Abstract

In the paper, we present the results of an analysis of data samples of 282 damaged buildings; the samples include the age of the building, the type of vertical bearing structures, the type of construction of the external walls, the method of the insulation of the walls, the number of floors, the buildings' functions, and the extent of the damage. The primary objective of the analysis was to evaluate the possibility of using panels of cold-formed thin-walled steel profiles to repair the damaged structures. The results of a study of typical projects of large panel buildings that were constructed in Ukraine and an analysis of the practical experience of repairing these types of buildings after blast actions can also be found. The research tasks are defined for implementing this technology in the process of repairing large panel buildings.

Address

[1] Dept. of Structural Engineering, Institute of Building Engineering, Faculty of Civil and Transport Engineering, Poznan University of Technology, Poznan, Poland

[2] Private enterprise "Poltava-Project", Poltava, Ukraine

[3] Dept. of Steel and Timber Structures, Faculty of Civil Engineering, Slovak University of Technology in Bratislava, Bratislava, Slovakia

[*] ***Corresponding author:*** volodymyr.semko@put.poznan.pl

Key words

- Large-panel buildings,
- Reinforced concrete panels,
- Cold-formed steel structures,
- Lightweight panels,
- Repairs after a war,
- War damage.

1 INTRODUCTION

As of 1 June 2022 (Lotocka, 2022), approximately 116,000 buildings, including 12,300 multi-storey buildings, have been dam-aged due to the active phase of the war in Ukraine, which started on 24 February 2022. Despite ongoing combat actions in Ukraine, programs for repairing damaged buildings are already on the way. For example, the RepairHouse " programme " (Vidnovidim) from the Energy Efficiency Fund was creat-ed for homeowners' associations to fund repair work on damaged buildings due to the invasion of the Russian Federation in Ukraine. For repairing and renovating damaged buildings, it is expedient to apply technical decisions that allow them to be completed quickly.

At the same time, in Ukraine, DSTU 9194:2022 has been in effect since 1 June 2023. This standard regulates the use of panels made from cold-formed, thin-walled steel profiles (CFSP or PCFSP panels). The application of these panels could be one method to quickly and reliably repair damaged large-panel buildings and frame buildings with already existing hinged reinforced concrete panels. The replacement of damaged reinforced concrete wall panels for PCFSP will permit the production and installation of this type of panel in the fastest amount of time without the need for heavy lifting equipment in dense urban conditions. Using this type of panel does not increase the weight of a wall's structures (versus filling the opening with bricks or lightweight concrete blocks), thereby creating a frame that braces the existing reinforced concrete panels. Additionally, this technical solution is energy efficien and will increase living comfort after the renovation. The primary goal is to estimate the possibility of repairing war-damaged large-panel buildings using panels of cold-formed thin-walled steel profiles

2 MATERIALS AND METHODS

The external walls are the largest envelope structures by area in multi-storey buildings. Therefore, the probability that these walls are damaged after shelling is greater than for other parts of a building. This makes research on the types of wall construction damage very realistic. The exterior walls differ in the type of material, mounting method, and method of load transfer from other structures. Repairability is an important parameter for any structure under the conditions of military operations. Repairability is the ability of a structure to have its serviceability restored after failure, i.e., reparability influences the level of failure and/or size of the damage. In our research, we will distinguish three groups of damage: local damage, destruction of part of a building, and damage in which any repair is not feasible.

The expediency of using PCFSP to repair damaged buildings can be determined from an analysis of the existing damage to buildings in Ukraine. For this analysis, we used a data sample from 282 photos of damaged buildings. These photos come from open sources, news websites, and news channels. The names of the sources and the sites of the photos will not be presented in the article (except for a few with characteristic damage on Fig. 1) to prevent the use of this information for non-scientific purposes. The data sample does not include buildings with fully destroyed structures and buildings with insignificant damage to envelope structures (such as broken windows and doors, damage to the insulation layer, tracks of small fires etc.). In the analysis, the buildings have had significant mechanical damage to the walls. Not included in the data sample were industrial buildings, but some buildings with double functions, warehouses, and shops, were mentioned. All the photos were taken and published in open sources before 1 September 2022.

Each photo was analysed to determine the following parameters of a building:

1. Year of construction (before 1945, 1945-1965, 1965-1980, 1980-1995, 1995-2010, after 2010).
2. Type of vertical bearing structures: full frame, incomplete frame (with load-bearing external walls and internal columns), frameless (with longitudinal and/or transverse bearing walls).
3. Type of external walls: reinforced concrete panels (large panels), bricks, lightweight concrete blocks, steel panels, glass panels, and large concrete blocks.
4. Method of wall insulation: without an insulation layer, External Thermal Insulation Composite Systems (ETICS), ventilated facades.
5. Number of floors
6. Function of the building: dwelling, public, or commercial (warehouse, store, mall).
7. The volume of damages: local (the opening in a wall from a missile; destruction or absence of a panel or concrete block; absence of part of the wall); destruction of

Fig. 1 *Examples of partially destroyed large-panel buildings (sources: a) Information at http://tiny.cc/y4e4vz; b) Information at http://tiny.cc/05e4vz; c) Information at http://surl.li/evqbf)*

Fig. 2 *Diagram of the percentage distribution of damaged buildings by: a) year of construction; b) type of vertical bearing structures; c) type of external walls; d) method of wall insulation; e) number of floors; f) function of the building*

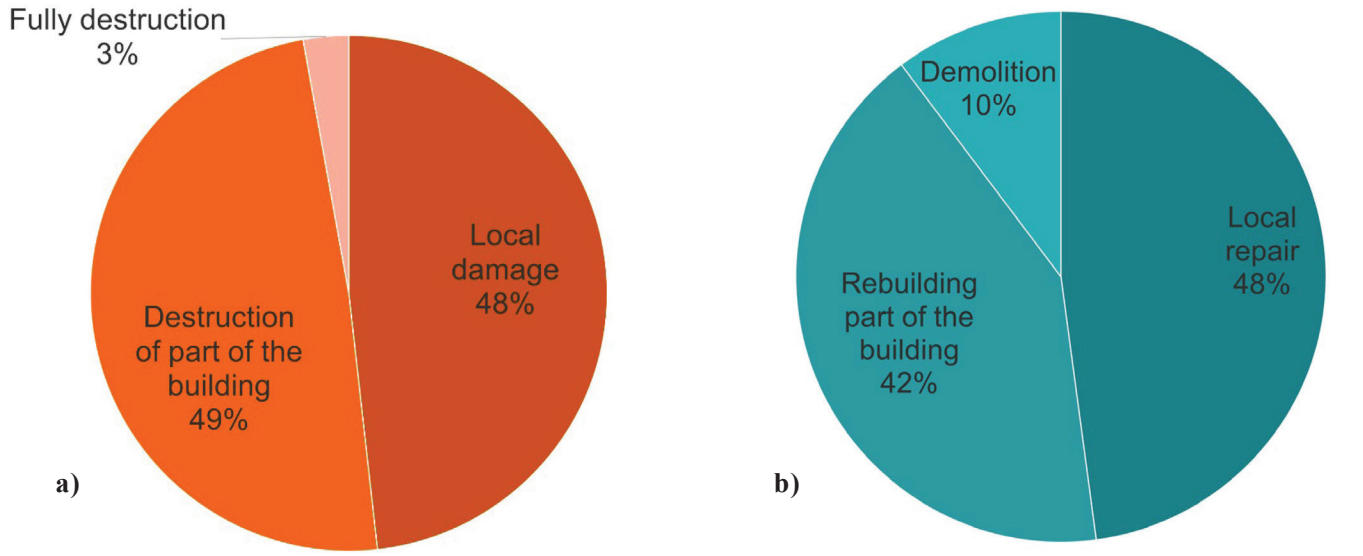

Fig. 3 *Diagram of the percentual distribution of the damaged buildings by: a) extent of damage; b) method and possibility of repair.*

part of the building (partial destruction of two or more types of bearing structures, for example, destruction of part of the wall and part of a floor) and damage in which repair is impractical (this category for the buildings which, after careful analysis, were recognised as dangerous).

8. Method and possibility of repair: local repair, rebuilding a part of the building, and demolition.
9. Conclusion about the possibility of using PCFSP to repair damaged buildings.
10. Solutions for using PCFSP: as a separate panel or as a system of panels.

The results obtained are based on the experience of the authors of the article.

3.1 Research on types of damage to wall constructions of civilian buildings during the war in Ukraine

The distribution of damaged buildings by the year of construction is shown in Fig. 2a. The year of construction was defined by periods. The entry of the building into the period was identified by the architectural planning decisions of the building pictured. The two most massive groups of damaged buildings (a total of 70%) are buildings constructed in 1965-1980 (41%) and 1980-1995 (29%). These are the buildings of the first massive series of construction and their later and improved variants. The third place was for a group of modern buildings that were constructed after 2010 (16%).

The diagram in Fig. 2b shows that most of the damaged buildings are frameless, with bearing walls as the vertical bearing elements. The second largest group is the frame buildings, i.e., 10% of the total amount of damaged buildings. Most of the frame buildings were constructed after 2010.

The largest part of the damaged buildings had walls made from bricks, i.e., 49% of the total quantity (Fig. 2c). The second group had walls made from reinforced concrete panels (32%). The third group (10%) had walls of large concrete blocks. In summary, these three groups covered buildings of all the construction periods. Walls of lightweight concrete blocks (7%), steel panels (1%), and glass panels (1%) were commonly related to buildings constructed after 2010 with a frame structure.

Seventy six percent (76%) of the damaged buildings did not have additional wall insulation (Fig. 2d). However, that is 9% less than the number of buildings constructed before 2010 (before the active implementation of the requirements of the first edition of DBN V.2.6, so we can conclude that from the data sample selected, nearly 10% of the buildings constructed before 2010 were modernised by thermal insulation. Twenty one percent (21%) of the buildings had external thermal insulation composite systems (ETICS), and 3% had ventilated facade systems. One building had three-layer brick walls with a mineral wool insulation middle layer.

Fig. 2e includes a distribution diagram of the damaged buildings by the number of floors. Buildings with 4-6 storeys (39%) and 7-10 storeys (32%) had more damage. Low-rise multi-apartment buildings and public buildings comprised 18% of the damaged buildings. The high-rise buildings amounted to 11%, which is quite a large group. The most significant group of damaged buildings (43%) has more than six storeys and indicates a need to develop lightweight wall systems for the repair of walls of that height.

Residential buildings are the largest group of damaged buildings, i.e., 83% (Fig. 2f); public buildings (schools, play schools) amounted to 13%; and large malls and other commercial buildings amounted to only 4 % of the total.

Despite the prefiltering of the photos of fully destroyed buildings, 3% of the damaged buildings were classified as fully destroyed after a careful analysis of the photos (Fig. 3a). Almost half of the buildings had local damage (48%), and 49% of the buildings had a destroyed part. Based on these data, it is possible to conclude (Fig. 3b) that 48% of damaged buildings can be repaired and that 10% of the damaged buildings have undergone extensive damage and must be demolished without any additional investigation. This means that not all of the buildings with destroyed parts can be rebuilt.

Out of the total quantity of damaged buildings that can be repaired (Fig. 4), it is possible to repair a total of 33 build-

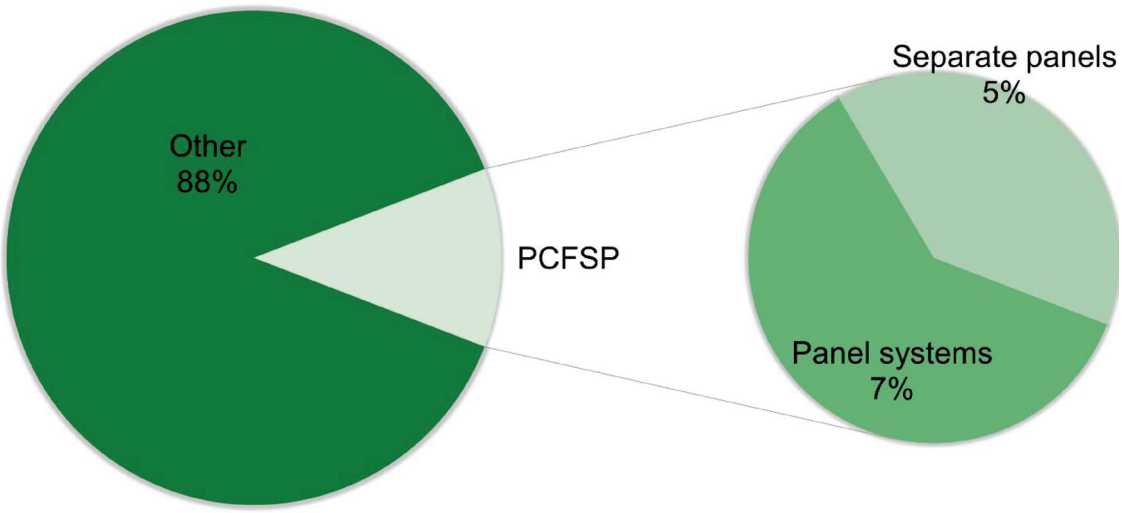

Fig. 4 *Percentual distribution diagram of buildings that could be repaired using panels from cold-formed steel profiles (separate panels or panel systems)*

ings with separate CFSP panels (5%) and CFSP panel system (7%). Of these buildings, 15 buildings were constructed in 1965-1980; 9 buildings were constructed after 2010; and 8 buildings were constructed in 1980-1995. Twenty one (21) buildings have large panel walls; eight buildings have walls made from lightweight concrete blocks; four buildings have steel panels, brick walls and big concrete blocks. Fifteen buildings are frameless; 14 buildings have a frame, and 4 have an incomplete frame.

From the analysis provided, we can conclude there is a possibility of using wall panels from cold-formed thin-walled steel profiles to repair damaged or missing reinforced concrete panels in large-panel buildings, frame buildings with hinged reinforced concrete panels (buildings of schools, public buildings, etc.), and frame buildings with walls made of lightweight concrete blocks.

The general requirements for the manufacture and installation of wall panels from cold-formed thin-walled steel profiles are presented in DSTU 9194:2022 and European Technical Assessment ETA 13/0312. They can be directly used for the renovation and repair of frame buildings. The possibility of using this technology to repair damaged buildings made from large-panel elements requires an additional analysis of the technical documentation for this type of building and an analysis of the experience of the repair of large-panel buildings after blast actions. These analyses are presented below.

3.2 Review of structural solutions for large panel buildings constructed in Ukraine

The issue of using PCFSP in the renovation of existing large-panel buildings was not present before the start of the active phase of the war in Ukraine. Designing PCFSP to repair large panel buildings requires the provision of an analysis of structural solutions for this type of building constructed in Ukraine. We need information on the thickness of the external panels, the methods of mounting panels to the supporting structures, and the function of the panels in the behaviour of all the bearing and enclosure structures.

The construction of the buildings from reinforced concrete panels occurred through typical projects and series that were developed at the end of the 1950s and modernised step-by-step in the following years. According to information from researchers on Kyiv (Agieieva et al., 2021), more than 5000 large panel buildings were constructed in the 1960s to 1970s in Ukraine, the majority of them from series 1-464 (20.85) and 1-480 (18.3%). The same data are presented in Denisenko (2012) and the Report on research work under Contract No. 16-417/2021. As of 2011, Denisenko (2012) reported that large panel buildings constituted 47% of the total number of multi-storey buildings in Ukraine. Series 1-464 was created by the "Giprostroyindustiya" Experimental Institute. The buildings were four and fiv -storeys tall; the building construction scheme had longitudinal and transverse bearing walls. The walls were of two types, i.e., external: three-layer (two external layers of reinforced concrete and a middle insulation layer) or a single layer of lightweight concrete; internal, i.e., single-layer made of reinforced concrete with a thickness of 120 mm. The distance between the transverse walls was 2.6 and 3.2 m. According to (Pleshkanovska and Biriuk, 2020), the buildings of series 1-464 were five and nine-storeys tall. The thickness of the external walls in Kyiv is 350 mm. Series 1-480 was developed by the KyivZDIEP Institute with parameters very close to those of series 1-464.

(Filonenko et al., 2018) noticed that in the 1980s, the building series 111 was actively implemented; it had external concrete panels of keramzit (expanded clay aggregate) with thicknesses of 300 and 350 mm and internal panels with thicknesses of 120 and 160 mm. The external panels consisted of a keramzit concrete core layer with thicknesses of 260 and 310 mm and two external layers of sand-cement mortar with a thickness of 20 mm each.

The analysis of the existing project documentation on multi-storey dwellings from the 1960-1995 construction years was provided by researchers from NDIBK and HNUMG (Album of technical solutions, 2012; Report on research work under Contract No. 16-417/2021). They divided all the enclosed structures of existing buildings by their materials and thicknesses as follows:

– lightweight concrete, lightweight concrete-facing ceramic tiles – external walls with thicknesses of 300, 350 and 400 mm (series 1-480, 1-467, 96, K-134, BPS-6, APPS, T, 87);
– three-layer panels with effecti e insulation material – external walls with thicknesses of 300 and 350 mm (series 1-464, 1-463, KT-12-16, 96);
– double layer - external walls with a thickness of 350 mm (series 1-335);
– aerated concrete - exterior walls with thicknesses of 250 and 300 mm (series 1-468, 1-464Ya);
– ceramic brick or silicate brick – exterior walls with thicknesses of 380 and 510 mm (series 1-438, 1-447, KP, 67, 87);
– lightweight brick masonry – exterior walls with a thickness of 380 mm (series KP, 67, 87).

Based on the above, the thickness of the external panels for large panel buildings varied from 300, 350 and 400 mm, depending on the material, region, and year of construction for a particular building. As a rule, single-layer keramzit concrete panels in Ukraine were used with thicknesses of 300-350 mm. The thicknesses of the internal walls were 120 and 160 mm. The walls were made of B20 concrete (modern analogue: C15/20).

The vertical and horizontal structures of large panel buildings work together through special vertical and horizontal joints. It should be noted that the joints of structures for diffe - ent series (Series 1-464A, 1967; Series 125, 1970, 1978; Series 2.130-1, 1975 a, b; Typical project 1-464A-3, 1963) do not practically diffe . The depth of the support of the floor panels, according to (Series 1-464A, 1967; Series 125, 1970, 1978; Series 2.130-1, 1975 a, b; Typical project 1-464A-3, 1963; Maklakova at al., 1986; Shereshevsky, 1981), on the exterior walls is 90 mm. Panel joints in large panel buildings must have a complex solution considering the requirements of strength, corrosion protection, thermal insulation, permeability to air and moisture, sound insulation, and the possibility of performing work in any season (SN 321-65).

As a rule, the internal wall panels and floor panels in large panel buildings are joined on a horizontal plane as platform joints (the joint when the load from above the lying panel is conducted to the bottom panel via the floor panel). The resistance to the tensile forces in vertical joints is achieved by steel connection elements welded to the steel bars of the panels. The contact of the concrete surfaces transfers the compressive forces in horizontal joints through a layer of mortar or other materials, which ensure the strength and density of the joint.

According to SN 321-65, the connection of transverse and longitudinal wall panels is based on the following principle: if the edge side of the transverse panels enters the joint between the longitudinal wall panels, a connection occurs at two points. If the transverse panel does not reach the joint between the longitudinal wall panels, then the connection must be made with concreted steel bars, at no less than three levels, but at a distance no greater than 10h (where h is the thickness of the wall).

The calculations related to large panel buildings are complicated and multifactorial. If the bearing capacity of the transverse walls is sufficien for their resistance to vertical forces, the external panels can be analysed only for the load from their self-weight (Dykhovichny, 1970).

To conclude our analysis of structural solutions for the large panel buildings that were constructed in Ukraine, we can state:
– The thickness of the external walls is 300-350 mm. The walls are mainly a single layer of keramzit concrete. The dimensions are: width – 2.6 m, 3.2 m (in one room) and 5.9 m or 6.0 m (in two rooms). The height of the panels is 2.7 m;
– The thicknesses of the internal walls from C15/20 concrete are 120 mm and 160 mm;
– External walls according to static function are bearing and(or) self-bearing;
– The external walls resist horizontal forces, which act on the plane of the walls, via a special construction of vertical joints, and can involve a cross-section of the wall when calculating the rigidity of the whole building;
– The external walls are located between two internal walls. They resist the load from the floor plate and from the weight of the panels standing above and transfer part of these loads to vertical panels through vertical monolithic key joints.

Based on the complexity of the structural calculations of large panel buildings and the random character of the probable damage as a result of combat actions, it is recommended that each building be considered as a unique structure and that a decision about the correct retrofit method for a building be based on certain defects and damages that occurred during its erection and exploitation, and during the war conflict

Based on the analysis of literary sources, series and typical projects, we can say that there are no direct objections to the use of lightweight frame panels as external panels in the regulatory documentation and requirements for large panel buildings.

3.3 Analysis of experience in the repair of damaged large panel buildings

Large panel buildings were mainly built in European countries. Most publications on the thermal insulation modernisation of this type of building, for example, have already been cited (Report on research work under Contract No. 16-417/2021; Filonenko et al., 2018; Album of technical solutions, 2012). A comprehensive analysis of papers on the exploitation of large panel buildings of the 21st century was done by (Malazdrewicz et al., 2022). In 1990, a "Recommendation for the repair and strengthening of prefabricated buildings by polymer solution" was developed; it presents recommendations for the repair and strengthening of large panel buildings. However, there is no recommendation about repairing mechanical damage and openings. (Malganov et al., 1990) developed "Atlas schemes and drawings" for the repair and strengthening of building structures. In the Atlas they presented a few examples of strengthening large panel buildings, but none of them cover replacing one or some of the panels in an existing building. (Mackiewicz et al., 2022; Ligęza, 2014; Szulc and Piekarczuk, 2022) dedicate themselves to liquidating operational damage and defects in large panel buildings and provide valuable information on the problem of repairing large panel buildings after explosive action.

(Malakhova and Balakshin, 2014) analysed the damage to a nine-storey building with large external panel walls. As a result of a gas explosion on the eighth floo , the bearing structures of the upper-lying floors were destroyed. As a result of an investigation, it was decided to repair part of the building with monolithic reinforced concrete structures. The same situation, but for a ten-storey building, was described in (Kumpyak et al., 2013). As a result of the explosion of a gas cylinder, the floor and wall panels on the last two floors of a building were destroyed. The building was renovated. First, a part of the attic and the tenth and ninth floors were demolished; then the building was fully rebuilt using new large panels.

(Hryhorovskyi et al., 2022) covers the approach of using BIM to monitor the technical condition of damaged buildings during a war and make decisions about renovation. The approach was approved during the monitoring of the technical situation of a large panel building in Kyiv, which was partially destroyed by a domestic gas explosion. Special attention was paid to strengthening it with load-bearing functions. The damage to the building was critical, so that part of the building was demolished.

The positive experience of the renovation of a large panel building in Kharkiv that was damaged in 2012 by a domestic gas explosion is described in (Reznik et al., 2022). The renovation project included partially replacing the existing large concrete floor plates with new monolithic concrete (on floors 9-11) and to strengthening the existing floor plates and internal bearing wall panels, (Shmukler et al., 2013) described repairing the external wall structures in more detail. For the repair, the enclosed structures used steel frames with rigid joints filled with foam-concrete blocks. The outer part of this structure was insulated with mineral wool with a thin plaster layer. Furthermore, (Reznik et al., 2022) have emphasised the problem of creating a new solution for the repair of large panel buildings because they believe the lack of large panel production capacity will not permit this type of building to be restored according to large panel technology.

You can see photographs of the repair process of buildings, including large panel buildings (Fig. 5). The (Fig. 1a) photo shows the renovation process of a building using the installation of new lightweight self-supporting lightweight concrete walls instead of large panels. The advantages of this method are not evident. This method is not industrial, and it is impossible to repair all of the damaged infrastructure, which includes thousands of multi-apartment buildings. This is why the possibility of developing industrial (or prefabricated) solutions, which enable maximum work to be done on the ground and the erection of panels on any floor using simple lifting mechanisms, is unquestionably realistic.

4 CONCLUSIONS

An analysis of war-damaged buildings in Ukraine shows that damage to wall structures can be repaired using panels from thin-walled cold-formed steel profiles. For 12% of the damaged buildings in the data sample, it is possible to use this technology. For the renovation of frame buildings with panels, the CFSP can use the recommendation of DSTU 9194:2022. The largest group of damaged buildings are large panel buildings (32%). An analysis of typical projects, series, and scientific and normative publications on this issue finds no limitation in the use of lightweight steel frame panels in the technology of large panels. The experience of renovating large panel buildings after gas explosions shows the possibility of recovering buildings by different methods, including using steel

Fig. 5 *The repair process of a large-panel building (sources: Information at https://cdn4.suspilne.media/images/resize/1040x1.78/680874f014cfdd08.jpg)*

frames. The plan for future work includes the development of principal schemes for CFSP panels to repair large panel buildings. The structural solution of the panels must be approved by calculating the requirements of mechanical strength, stability, and energy savings.

Acknowledgements

This research is provided within the project "Cold-formed light gauge steel wall systems for rapid restoration of war-damaged houses in Ukraine", which was funded by the Visegrad Scholarship Programme.

REFERENCES

Agieieva, G. – Kafiev, K. – Kriveljov, L. (2021) *Reconstruction of the first mass series buildings as the principle of the sustainable development of neighbourhoods and residential quarters in cities*. Science and Construction, Vol. 27(1), pp. 32-40. https://doi.org/10.33644/scienceandconstruction.v27i1.5 [in Ukrainian].

Album of technical solutions (2012) *Fundamental technical decisions for the thermal reconstruction of the facades of the dwelling houses of the 1960-1995 building* – Kyiv: NDIBK, 2012, 48 pp. [in Ukrainian].

Denisenko, A. (2012) *Renovation and preservation of the housing stock through the reconstruction of houses of the first period of industrial housing construction.* Bulletin of the Prydniprovska State Academy of Civil Engineering and Architecture, Vol. 1-3 (166-168), pp. 154-165 [in Russian].

DSTU 9194:2022. *Cold-Formed Light Gauge Steel Wall Systems. Requirements for Fabrication and Erection*. Kyiv, 2022 [in Ukrainian].

Dykhovichny Yu. (1970) *Design and calculation of residential and public buildings with an increased number of sto-reys*. Moscow, 1970 [in Russian].

European Technical Assessment ETA 13/0312. *Kits for KNAUF external wall systems WM111C, WM211C, WM311C, WM411C, WM111G, WM211G, WM311G, WM411G.* Available at: https://itec.es/certification/files.aspx?tipus=dite&num=13/0312 (accessed at 14.01.2022).

Filonenko, O. – Yurin, O. – Kodak, O. (2018) *Thermal modernization of the panel buildings external walls*. International Journal of Engineering and Technology (UAE), Vol. 7 (3), pp. 116-122. https://doi.org/10.14419/ijet.v7i3.2.14386

Hryhorovskyi, P. – Osadcha, I. – Jurelionis, A. – Basanskyi, V. – Hryhorovskyi, A. A. (2022) *BIM-Based Method for Structural Stability Assessment and Emergency Repairs of Large-Panel Buildings Damaged by Military Actions and Explosions: Evidence from Ukraine.* Buildings. 2022; Vol. 12(11), 1817. https://doi.org/10.3390/buildings12111817

Kumpyak, O. G. – Galyautdinov, Z. R. – Pakhmurin, O. R. – Samsonov, V. S. (2013). *Practical experience in restoring the survivability of a ten-storey large-panel residential building after a gas cylinder explosion.* Building Structures, Vol. 78 (1), pp.353-358.

Lotocka N. (2022) *In Ukraine, the occupiers destroyed or damaged 116,000 residential buildings.* LB.ua. Accessed June 16, 2022. https://lb.ua/economics/2022/06/16/520202_ukraini_okupanti_zruynuvali_abo.html

Ligęza, W. (2014) *Budownictwo wielkopłytowe po latach. Wybrane problemy remontowe*. Budownictwo i Architektura. 2014, Vol. 13(3), pp. 15–25 [in Polish]

Mackiewicz, M. – Krentowski, J.R. – Knyziak, P. – Wardach, M. (2022) *Consequences of excessive deformation of structural elements in precast buildings*. Engineering Failure Analysis, Vol. 137, 106261, https://doi.org/10.1016/j.engfailanal.2022.106261

Maklakova, T. et al. (1986) *Constructions of civil buildings: textbook for universities*. Moscow: Stroyizdat, 1986 [in Russian].

Malakhova, A.N. – Balakshin, A.S. (2014) *Emergency destruction of a panel residence building. Type series 1-115.* Vestnik MGSU. 2014. No.11. pp.109-117 [in Russian].

Malazdrewicz, S. – Ostrowski, K.A. – Sadowski, Ł. (2022) *Large Panel System Technology in the Second Half of the 20th Century—Literature Review, Recycling Possibilities and Research Gaps.* Buildings, 2022, Vol. 12(11), 1822. https://doi.org/10.3390/buildings12111822

Malganov, A.I. – Plevkov, V.S. – Polishchuk, A.I. (1990) *Restoration and strengthening of the building structures of the emergency and reconstructed buildings. Atlas of schemes and drawings.* Tomsk: TSNTI, 1990, 316 pp. [in Russian].

Pleshkanovska, A. – Biriuk, S. (2020) *Outdated housing stock as an object of complex reconstruction programmes and projects (based on the example of Kyiv city)*. J. Urban Reg. Anal., Vol. 13, pp. 257–280.

Recommendations for the restoration and strengthening of prefabricated buildings with polymer solutions. TbilZNIIEP. Moscow, Stroyizdat, 1990. - 160 pp. [in Russian].

Report on research work under contract No. 16-417/2021 *Analysis of factors influencing the achievement of minimum energy efficiency requirements of commissioned buildings and development of proposals to improve the methodology for determining the economically feasible level of energy efficiency of buildings*, Kharkiv National University of Urban Economy named after O.M. Beketova, 2021 [in Ukrainian].

Reznik, P. – Almohamad, M. – Tenesesku, V. (2022) *Analysis of constructive solutions to existing Kharkiv city buildings of the housing fund on the subject of their performance as a consequence of the influence of combat actions.* Collection of scientific works of the Ukrainian State University of Railway Transport. Kharkiv: UkrDUZT, 2022. No. 201. pp. 41-56. https://doi.org/10.18664/1994-7852.201.2022.267755

Series 1-464A. (1967) *Large-panel houses for construction in II and III building-climatic zones. Album V. Factory-made items. Part 3a-D. Multilayer exterior wall panels.* Moscow, 1967 [in Russian].

Series 125. (1970) *Large-panel residential buildings for construction in building climate zones II and III. Standard projects 111-125-1, 111-125-2. Part 9. Knots and details. Sections 9-2. Mounting units and details.* Moscow, 1970 [in Russian].

Series 125. (1978) *A comprehensive series of standard projects for large-panel residential and public buildings. Part 9. Knots and details. Sections 9-36. Mounting units and details.* Moscow, 1978 [in Russian].

Series 2.130-1. (1975 a) *Details of the walls and partitions of residential buildings. No. 15. External load-bearing walls of reinforced concrete three-layer construction for 5 and 9-storey large-panel buildings.* Moscow, Central Institute for Standard Design, 1975 [in Russian].

Series 2.130-1. (1975 b) *Details of the walls and partitions of residential buildings. Issue 17. Single-layer exterior walls of 5 and 9 storey large-panel buildings*. Moscow, Central Institute for Standard Design, 1975 [in Russian].

Shereshevsky, I. (1981) Design of Civil Buildings: A textbook. Leningrad: Stroyizdat, 1981 [in Russian].

Shmukler, V. – Goncharenko, D. – Konstantinov, A. – Zinchenko, V. (2013) *Restoration of a large-panel building destroyed as a result of a man-made disaster*. Industrial Construction and Engineering Structures. Vol. 2 (2013) pp. 34-39. https://urdisc.com.ua/rl/info/2_13.pdf [in Russian].

SN 321-65. *Guidelines for the design of structures for large-panel residential buildings*. Moscow: Publishing House of Literature on Construction, 1966. 164 pp. [in Russian].

Szulc, J. – Piekarczuk, A. (2022) *Diagnostics and technical condition assessment of large-panel residential buildings in Poland*. Journal of Building Engineering, Vol. 50, 2022, 104144. https://doi.org/10.1016/j.jobe.2022.104144

Typical project 1-464A-3. (1963) *Five-storey building with 60 apartments. Album I.* Moscow, Central Institute for Standard Projects, 1963 [in Russian].

«Vidnovidim» (RepairHouse), https://sites.google.com/view/programa-vidnovidim-ukr

sciendo

Slovak Journal of Civil Engineering

Vol. 32, 2024, No. 2, 10 – 20
DOI: 10.2478/sjce-2024-0009

EXPERIMENTAL ANALYSIS OF THE POST-FRACTURE BEHAVIOUR OF LAMINATED GLASS WITH BOLTED CONNECTIONS

Lucia ONDRUŠKOVÁ[1]*, Ján BRODNIANSKY[1], Ján BRODNIANSKY[1], Tomáš KLAS[1]

Abstract

Ensuring the sufficient residual resistance of glass structures after the failure of one glass ply to the failure of all the glass plies is an integral part of the design of glass structures. This paper presents an experimental study of bolted connections in laminated glass during three stages of a glass specimen: an intact glass specimen, a specimen with one ply of glass broken, and a specimen with both plies of glass broken. The effect of the type of glass was observed. The experiment proved that laminated glass made from thermally-toughened glass with bolted connections in its unfractured state has significantly higher resistance than laminated glass made from annealed glass. In a state of both plies of glass broken, the specimens made from annealed glass showed a higher residual resistance than specimens made from thermally toughened glass. The performance at this stage was also influenced by the temperature and loading speed. The expected strength of the glass was calculated on the basis of numerical models.

Address

[1] Dept. of Steel and Timber Structures, Slovak University of Technology in Bratislava, Slovakia

* ***Corresponding author:*** jan_brodniansky@stuba.sk

Key words

- Laminated glass,
- Bolted connection,
- Residual resistance.

1 INTRODUCTION

Today, there are broad possibilities for the use of glass in buildings, such as facades and roofs, even glass beams and fins or tubular glass members (Wurm, 2007). The mentioned applications lead to higher requirements regarding the resistance and safety of the glass members. Due to the brittle nature of glass, in addition to the unfractured state of a glass member, it is necessary to take safety into consideration during the fracture of glass plies to prevent harm to human health or property and ensure the sufficient resistance of the glass member in a post-fracture state. The proof of sufficient residual resistance will be required by the upcoming standard EN 19100 (Feldmann et al., 2023).

To meet these requirements, the use of laminated glass is necessary. It consists of two or more glass plies joined by a transparent interlayer, which provides for the coupling of glass plies in an unfractured state and plays an important role in the residual resistance of the fractured glass member. The mechanical properties of the interlayer primarily depend on the type of interlayer, temperature, and duration of the load. The most widely used interlayer is the (polyvinyl butyral) PVB interlayer. The shape of the stress-strain curve of the PVB interlayer can differ based on the glass transition temperature T_g; the behaviour above the T_g can be described by a hyperelastic model and by a elasto-viscoplastic below the T_g (Delincé et al., 2008). Another option are ionomer interlayers, which provide higher strength and stiffness compared to a PVB interlayer (S. Bennison et al., 2002).

Kott and Vogel (2004) described the state of laminated glass loaded perpendicularly to its plane (out-of-plane bending) in 3 stages:

Stage I – all the glass plies of the laminated glass are intact,
Stage II – a combination of broken and intact glass plies. The load is carried by the intact glass plies,

Stage III – all the glass plies are broken. Locked-up glass fragments in the compressed zone transfer the internal compression forces, whereas the tension forces are transferred by the interlayer.

The stiffness of laminated glass with all the glass plies broken depends on the mechanical properties of the interlayer (Belis et al., 2009; Delincé et al., 2010), the size and shape of the glass fragments, and the adhesion of the PVB interlayer to the glass (Ferretti et al., 2012). The size and shape of the glass fragments depend on the type of glass (annealed glass / heatstrengthened glass / thermally-toughened glass), but they are also affected by the type of load (impact, quasi-static) and its rate, the type of support (Overend et al., 2007; Zhao et al., 2019) and the thickness of the glass (N. Pourmoghaddam and Schneider, 2018).

Experimental research of the post-fracture state of laminated glass is complemented by theoretical research using analytical and numerical models to describe its post-fracture behaviour. In the analytical approach, the stiffness of laminated glass with both glass plies broken can be described by its effective stiffness. Tensile stiffness is defined by introducing an effective Young's modulus (S. J. Bennison and Stelzer, 2009; Galuppi and Royer-Carfagni, 2016). When dealing with the bending response, it is necessary to distinguish between out-of-plane bending; see stage III (Delincé et al. 2008; Kott and Vogel, 2004; Galuppi and Royer-Carfagni, 2018), and in-plane bending (Galuppi and Royer-Carfagni, 2018).

For modelling the failure of brittle materials **(**glass or ceramics**)** by means of a numerical analysis, the Johnson-Holmquist material model is used, especially for high pressure, shear deformation, and high deformation speed, such as the impacts of projectiles from weapons (Štiglic, 2015) or the impacts of debris carried by the wind and other bodies and explosions (Zhang at al., 2015). The fragmentation of thermally-toughened glass can be modelled by applying the Voronoi tessellation (Pourmoghaddam et al., 2018) or modelling fragments using regular geometric shapes, such as squares or hexagons (D'Ambrosio et al., 2019). An investigation of the structural application of glass also deals with the possibilities of increasing the residual resistance by reinforcement of the edge in tension by steel strips (Louter, 2007; Slivanský, 2012), wood (Kreher, 2004), or carbon fibres (Palumbo, 2005).

After exceeding the value of residual resistance, there is a complete collapse of a glass member, which can be a consequence of the following mechanisms (Delincé et al., 2008; Zhao et al., 2019) rupture of the interlayer (in tension or shear), delamination of glass fragments from the interlayer, splitting up of the glass fragments or their breakage into smaller pieces in the compressed zones, which leads to greater deformations and the slipping out of supports.

The type of support of a glass pane plays an important role in its design, both for its prefracture and post-fracture state. The supporting system must prevent the formation of unexpected additional stresses (Ryan et al., 1997). To prevent high stress peaks in the glass near the supports, glass and steel elements have to be separated by a suitable insert made of plastic or aluminium. Because of the high stress peaks near the bolted connections, the use of heat-strengthened glass or thermally-toughened glass is required. The STN 74 3305 – Ochranné zábradlia standard prescribes the distances from the edge of a point fixing in glass of at least 80 mm and a maximum of 250 mm.

The focus of the research presented is the experimental investigation of the residual resistance of laminated glass with bolted fixings, the manner of any failure, the resistance of specimens with partially and fully broken glass plies, and the effect of the type of glass used on its post-fracture behaviour. For a more detailed description of the load distribution on the glass plies, the stresses at the location of the holes for the bolted connections were determined using strain gauges. The numerical analysis deals with the determination of the stress value estimated at the edge of the hole at the formation of the first crack.

2 EXPERIMENT - MATERIALS AND METHODS

2.1 Specimens and the bolted connections in glass

The test specimens were made from laminated glass consisting of two plies of 8 mm-thick glass and a 1.52 mm-thick PVB interlayer (RB 41 Saflex clear); the total thickness was 17.52 mm. The dimensions of the specimens were 250 x 400 mm. Two 20 mm-diameter holes were placed at half of the width of the sample (125 mm from the edge) and 80 mm from the edge in the longitudinal direction of the sample.

There were 5 specimens made from annealed glass (ANG), which were labelled ANG1 – ANG5, and 5 specimens made from thermally-toughened glass (TTG), which were labelled TTG1 – TTG5. The glass plies were numbered "ply 1" and "ply 2". The lower hole was labelled "A" and the upper hole "B".

The bolted connections in the glass specimen consisted of a M14 bolt with a shank, a bolt grade 8.8, and a polyamid insert (PA6) with an outer diameter of 20 mm and an inner diameter of 14 mm; the thickness of the insert was 3 mm.

2.2 Experimental set-up

The specimens were tested in a Testometric FS500CT testing machine. Steel plates that were 25 mm thick were inserted in the jaws of the machine. Two 6 mm-thick plates were connected to those plates by bolts (M14, bolt grade 8.8). The glass specimen was connected to the 6 mm-thick steel plates by the bolted connections described in 2.1. This set-up created an approximately 3.7 mm-wide gap between the glass and steel plate used to place the strain gauges.

The ANG1, ANG2, ANG3 and TTG1 and TTG2 specimens were equipped with strain gauges on the sides of the holes to capture the stress peaks near their edge. The strain gauges were labelled TA1 - TA4 and TB1 - TB4, see Fig. 1. Due to the chamfer of the edges of the glass and the dimensions of the foil carrier of the strain gauge's measuring grid, the values of the strain could not be measured at the very edge of the hole, but approximately 3 mm further. The type of strain gauge used was HBM 1-LY11-3/120, a linear strain gauge with a measuring grid length of 3 mm.

The signal from the strain gauges was transmitted and recorded by a Spider8 measuring station connected to a computer using Catman software. In the case of the ANG1 specimen, the sampling frequency used was 20 Hz, but for the other specimens, it was 10 Hz.

The samples were loaded in cycles until the breakage of both plies of glass occurred at one hole. The target force in

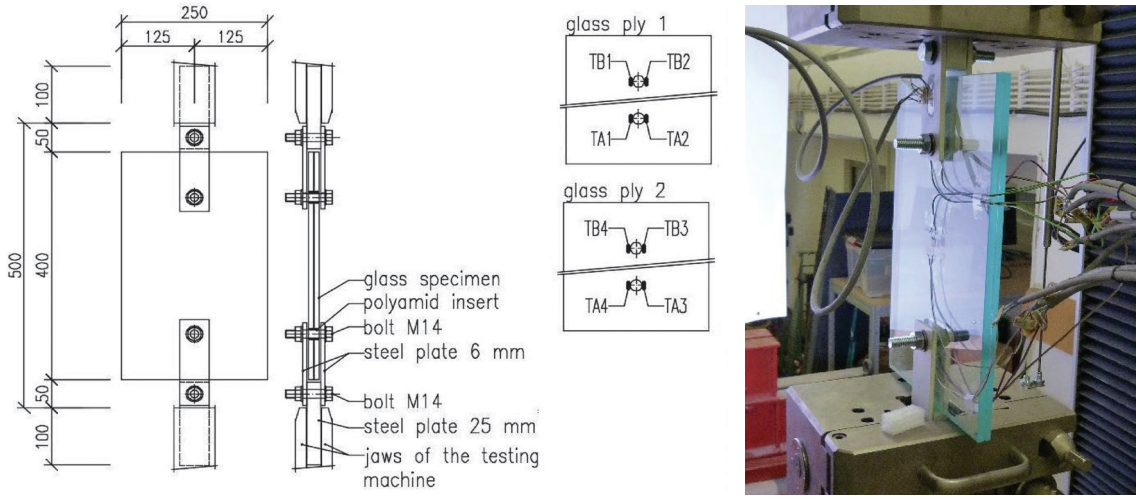

Fig. 1 *Scheme of the experimental set-up and placement of the strain gauges (the glass ply 2 is pictured from the side of the glass ply 1; the TA1 strain gauge is located above the TA4 strain gauge, etc.)*

each cycle was increased by 1 kN (ANG1-ANG5, TTG1), 2 kN (TTG2, TTG5 – up to 20 kN, then increased by 1 kN) or 5 kN (TTG3, TTG4) compared to the previous cycle. After reaching the target force for the given cycle, the testing machine maintained a constant deformation for 20 seconds. Then the specimen was unloaded to 0 kN; after 20 seconds, the next loading cycle began. After the breakage of both plies of glass at one hole (the load was transferred only by the PVB interlayer), the specimen was loaded at the specified speed until the PVB interlayer tore or the limits of possible deformation in the testing machine were reached.

The loading speed used was 2 mm/min, except for the TTG3 and TTG4 samples, where the loading speed used was 4 mm/min.

The test of the partially broken specimens, labelled ANG2-B and ANG3-A (the letter A/B represents the undamaged hole), outside the testing machine was added to the experiment. These specimens made of annealed glass were broken at only one hole. Two mm thick glued steel plates were attached to the remaining part of the specimen. The glue used was Loctite AA 3298 with the Loctite SF 7386 activator.

The bolts were inserted through holes in the glued plates, and the specimen was connected to the eye embedded in the rails using carabines, see Fig. 2. The side of the specimen with intact glass plies at the hole used the same bolted connection and steel plates as in the experiment in the testing machine to connect to the load cell and the crane hook. The sample was loaded manually by pulling the crane chain.

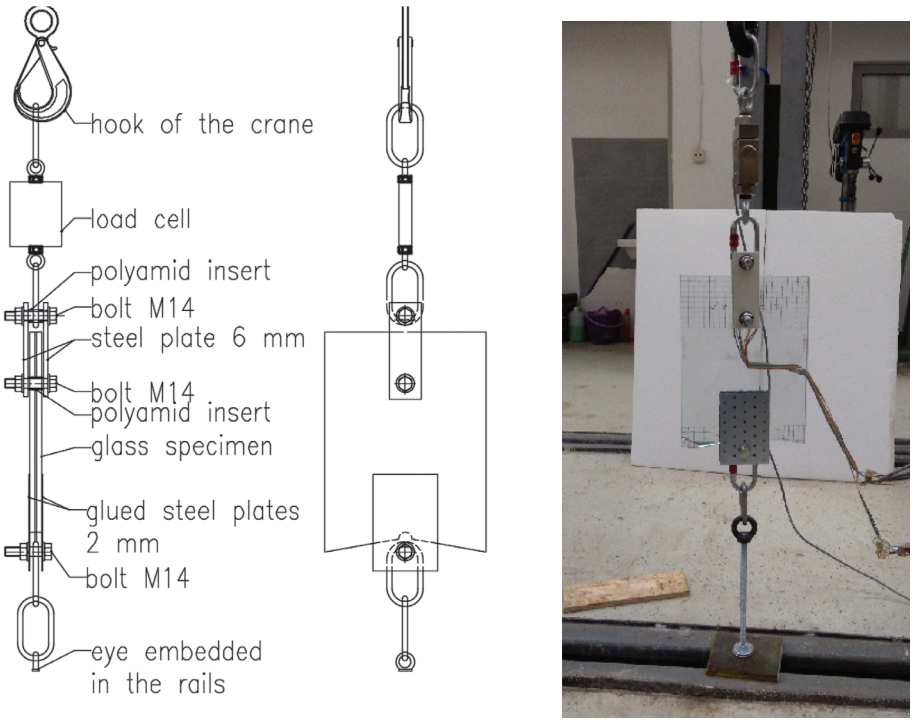

Fig. 2 *Scheme of the experimental set-up for the ANG2-B, ANG3-A partially broken specimens and the specimen prepared for the experimental tests.*

3 RESULTS AND DISCUSSION

The progress of the experiment can be divided into three stages, similar to the stages described by Kott and Vogel (2004):

In the first stage, both plies of glass were intact. In the second stage, only one ply of glass was broken at the hole. The third stage of the specimens made from annealed glass (ANG) occurred when both plies of glass were broken at the same hole. Due to the nature of its breakage, this stage appeared after the complete breakage of both plies of glass on the specimens made from thermally-toughened glass (TTG).

3.1 Stage I. – intact specimens

The purpose of the measurements using strain gauges was to illustrate the behaviour of the specimens in terms of the load distribution on the individual plies of glass. In the "perfect case", the force applied would be evenly distributed on the plies, but the measurements showed that this was rather exceptional: usually one ply of glass carried more of a load than the other. The differences between the measurements varied at the holes of the same specimen. This means that there could be smaller differences between the values measured on the glass plies at hole A than at hole B (and vice versa), or the other ply of glass at hole A could carry more of a load than at hole B. These differences arose despite the efforts to center the specimens.

3.2 The breakage of the glass plies of the specimens and stage II. – specimens with one of the glass plies broken at the hole

Stage II. appeared only on the specimens made from annealed glass (ANG). Both glass plies of the specimens made from thermally-toughened glass (TTG) cracked at the same moment, i.e., they went from stage I directly to stage III.

Two types of crack sequences appeared on the specimens made from annealed glass (ANG). In the first type, both plies of the glass cracked at the same hole, but the other hole remained intact. This type appeared when the higher stresses at both holes prevailed on the same glass plies of the specimen, i.e., specimens ANG2 and ANG3. Based on the crack sequence, it can be assumed that the ANG5 specimen was stressed in the same manner.

When the highest stresses at the holes appeared on the opposite glass plies (e.g., the highest stress at the hole A was on ply 1 and the highest stress at the hole B was on ply 2), the first cracks also appeared in these places, which means that at each hole, one of the glass plies was broken and that these plies were on the opposite side. This distribution of stresses and cracks appeared on the ANG1 specimen, and it can be presumed that the same stress distribution led to the same type of crack sequence on the ANG4 specimen.

The first crack of the specimens made from annealed glass (ANG) appeared at an applied force of 6.25 to 6.86 kN. The exception was the partially broken ANG2-B specimen. Assuming that the "weaker" hole was already broken (first crack – a combination of a critical surface flaw and higher stress), a higher resistance of the remaining hole was expected. Similarly, a higher resistance of the partially broken ANG3-A specimen was expected. In this case the maximum value of the force reached was similar to the ANG 3 specimen, but the stresses by the hole determined using strain gauge measurements were higher. The values of the force applied and stresses reached at the creation of the first crack are summarized in Tab. 1.

For "full" specimens, after the creation of the first crack, there were one or more loading cycles until the last crack appeared. The exception was the ANG2 specimen; the transition from the intact specimen to both glass plies cracked at the hole occurred in 1.01 seconds. In the case of the ANG1, ANG3-A, ANG4, and ANG5 specimens in stage II., they reached even higher values of the load than before the formation of the first crack. These values are summarized in Tab. 2.

It is well known that the strength of glass depends on small surface defects: the first crack originated from a place where the most unfavourable combination of a stress peak and a deeper surface flaw appeared. Based on the strain gauge measurements of the specimens selected, the load was not evenly distributed on the glass plies, but one glass ply carried a significantly higher part of the load. After the rupture of the more loaded glass ply, the remaining ply had the capacity to carry the increased load. The possible explanation for the cases of the higher resistance of a specimen after the creation of the first crack than the resistance of the intact specimen is that the flaws of the surface on the uncracked hole were shallower or more rounded, or that the critical surface flaw was located further from the location of the stress peak.

Both glass plies of the specimens made from thermally-toughened glass (TTG) cracked at the same time. As is

Tab. 1 *Force applied and stresses reached at the creation of the first crack: specimens made from annealed glass (ANG)*

Specimen	Applied force [kN]	Hole „A"				Hole „B"			
		TA1 [MPa]	TA2 [MPa]	TA3 [MPa]	TA4 [MPa]	TB1 [MPa]	TB2 [MPa]	TB3 [MPa]	TB4 [MPa]
ANG1	6.25	-1.60	-1.48	17.74	17.79	15.78	14.31	0.15	-0.41
ANG2	6.68	1.12	2.78	15.32	10.95	6.61	6.61	12.77	9.85
ANG2-B	9.03	-	-	-	-	6.00	4.83	19.83	18.12
ANG3	6.86	10.77	10.13	9.16	11.23	6.23	-	12.68	11.89
ANG3-A	6.86	2.37	4.93	12.90	17.56	-	-	-	-
ANG4	6.58	-	-	-	-	-	-	-	-
ANG5	6.74	-	-	-	-	-	-	-	-

Tab. 2 *Maximum force applied and stresses reached after the creation of the first crack and before the breakage of both glass plies at one hole: specimens made from annealed glass (ANG)*

Specimen	Applied force [kN]	Hole „A“				Hole „B“			
		TA1 [MPa]	TA2 [MPa]	TA3 [MPa]	TA4 [MPa]	TB1 [MPa]	TB2 [MPa]	TB3 [MPa]	TB4 [MPa]
ANG1	8.41	18.51	14.61	-	-	-	-	-9.09	-7.28
ANG2	-	-	-	-	-	-	-	-	-
ANG2-B	9.01	-	-	-	-	3.67	3.54	-	34.242
ANG3	5.45	8.63	8.19	6.41	8.33	2.54	-	-	-
ANG3-A	7.84	-5.92	-3.00	-	-	-	-	-	-
ANG4	12.05	-	-	-	-	-	-	-	-
ANG5	9.05	-	-	-	-	-	-	-	-

Tab. 3 *Force applied and stresses reached upon the breakage of both plies of glass: specimens made from thermally-toughened glass (TTG)*

Specimen	Applied force [kN]	Hole „A“				Hole „B“			
		TA1 [MPa]	TA2 [MPa]	TA3 [MPa]	TA4 [MPa]	TB1 [MPa]	TB2 [MPa]	TB3 [MPa]	TB4 [MPa]
TTG1	28.87	28.15	37.16	32.10	37.47	27.90	28.12	63.00	47.45
TTG2	31.92	58.85	43.91	48.62	46.61	45.61	50.32	53.04	52.66
TTG3	31.91	-	-	-	-	-	-	-	-
TTG4	27.61	-	-	-	-	-	-	-	-
TTG5	23.54	-	-	-	-	-	-	-	-

Fig. 3 *Hole with needle-shaped fragments, where the damage emerged (left); hole with the mosaic fragment pattern (right)*

typical of thermally-toughened glass, the glass ply burst into a large number of small fragments. The hole from which the damage emerged could be identified by radial cracks and needle-shaped fragments, see Fig. 3. The glass fragmentation at the other hole had a typical mosaic pattern. A summary of the force applied and stresses reached at the breakage of these specimens is in Tab. 3. Except for the TTG5 specimen, the value of the force applied on all the other specimens at the moment of breakage ranged from 27.61 to 31.92 kN. On the TTG5 specimen it was 23.54 kN. The cause of the lower resistance of the TTG5 specimen was the mutual shift of the glass plies, i.e., approximately 2 mm.

3.3 Stage III. – specimens with both glass plies broken

When both plies of the glass were broken, the load was carried only by the PVB interlayer. The difference in glass types, i.e., annealed glass versus thermally-toughened glass, had a major impact on the resistance of the specimens after the breakage of both glass plies.

After the appearance of the last crack, the experiment was not stopped, and the load was not completely removed. The loading continued from the value to which the force dropped at the appearance of the last crack. These values are summarised in Tab. 4.

Tab. 4 *Initial force and deformation after breakage of both glass plies*

Specimen	F_0	d_0	Specimen	F_0	d_0
	[kN]	[mm]		[kN]	[mm]
ANG1	0.42	2.30	TTG1	0.85	5.16
ANG2	0.20	0.74	TTG2	0.68	5.06
ANG3	0.88	2.07	TTG3	0.26	5.05
ANG4	0.42	1.68	TTG4	-0.09	4.66
ANG5	0.14	1.39	TTG5	0.62	6.71

The deformation of the glass specimen itself with both plies of glass broken was determined by the subtraction of the deformation of the entire experimental assembly at the moment of the last breakage from the total deformation.

$$d_1 = d_{1.abs} - d_0 \quad (1)$$

Tab. 5 *Maximum forces and corresponding deformations achieved after the breakage of both plies of glass: specimens made from annealed glass (ANG)*

Specimen	Max. force				Max. force – „constant section“				Temp.
	$F_{1.abs}$ [kN]	F_1 [kN]	$d_{1.abs}$	d_1	$F_{2.abs}$ [kN]	F_2 [kN]	$d_{2.abs}$ [mm]	d_2 [mm]	[°C]
ANG1	3.72	3.30	38.50	36.19	-	-	-	-	20
ANG2	2.61	2.41	28.25	27.51	-	-	-	-	21
ANG3	3.67	2.79	29.27	27.20	-	-	-	-	22
ANG4	3.63	3.21	2.76	1.08	3.37	2.95	23.23	21.55	10
ANG5	4.16	4.02	2.44	1.05	3.56	3.43	25.02	23.63	10

d_1 – deformation of the glass specimen itself with both plies of glass broken,
$d_{1.abs}$ – total deformation of the experimental assembly with the specimen with both plies of glass broken,
d_0 – deformation of the entire experimental assembly at the moment of the last breakage of the glass.

Since the loading did not start from a zero level, the value of the force by which the force acting on the specimen was increased compared to the initial force acting on the specimen after the failure of both plies of glass at one hole was determined as:

$$F_1 = F_{1.abs} - F_0 \tag{2}$$

F_1 – the force by which the force applied on the specimen increased, “force increase”,
$F_{1.abs}$ – force exerted by the testing machine,
F_0 – initial force after the moment of the last glass breakage.

The force determined according to Eq. (2) is used to describe the trend in the “force increase”, depending on the deformations of the sample itself (determined according to Equation (1)).

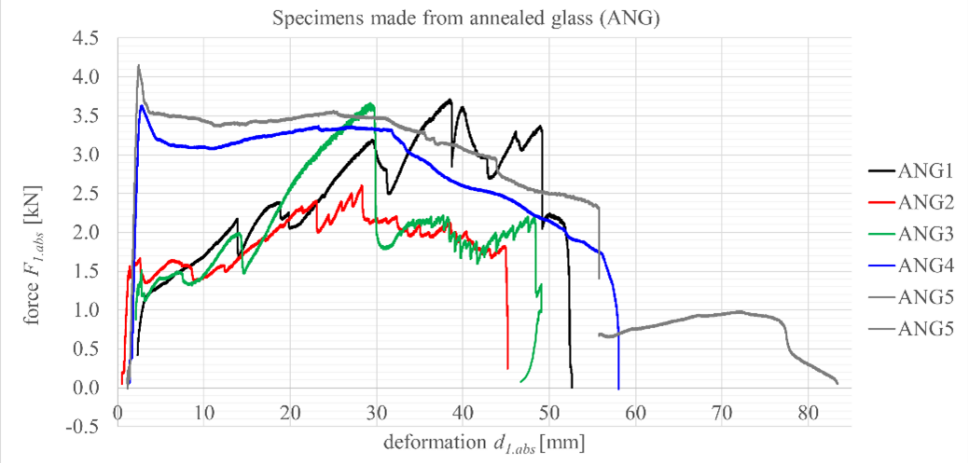

Fig. 4 *Dependence of the force deformation (force exerted by the testing machine $F_{1.abs}$, total deformation of the experimental assembly $d_{1.abs}$) on the specimens made from annealed glass (ANG)*

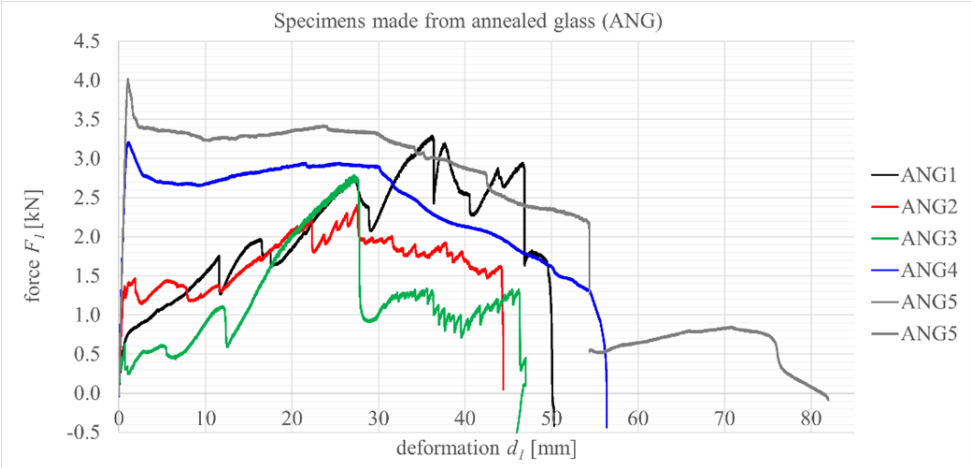

Fig. 5 *Dependence of the force deformation (the “force increase” F_1, deformation of the glass specimen itself d_1) on the specimens made from annealed glass (ANG)*

On the specimens made from annealed glass (ANG), both plies of glass were only cracked by one of the holes. During a further loading of the sample, the PVB interlayer gradually peeled off from the glass, and the glass fragments were falling off. The observed delamination of the PVB interlayer was not symmetrical on both sides of the PVB foil due to the nonidentical pattern of the cracks on the glass plies. On the one side of the specimen, it could be deeper, and on the other side, shallower. The interlayer tearing originated on one or both sides of the hole and spread to the edges of the specimen.

All the specimens made from annealed glass (ANG) were loaded at a speed of 2 mm/min. They were divided into two groups: the specimens ANG1, ANG2, and ANG3 tested at a temperature of 20 °C (+2 °C), and the specimens ANG4 and ANG5 tested at a temperature of 10 °C. The values of the maximum forces achieved and deformations are summarised in Tab. 5.

The temperature had a significant effect on the course of the dependence of the force and deformation of the specimen in stage III, as pictured in Figs. 4 and 5. In the group of specimens tested at 10 °C (ANG4, ANG5), the state of the PVB interlayer below the glass transition temperature was probably reached (Delincé et al., 2008); it resembled the behaviour of the stiffer ionomer interlayer. After the initial surge, the force with the increasing deformation maintained a constant level. The maximum force achieved on this "constant section" is in Tab. 5 and labelled as $F_{2.abs}$. From the 30 mm deformation, the force began to gradually decrease as a result of the tearing of the PVB interlayer.

The PVB interlayer of the ANG5 specimen also started tearing at the outer edge of the specimen. The strip of the PVB interlayer connecting the lower and upper parts of the specimen stretched diagonally; therefore, the ANG5 specimen could reach an 80 mm deformation. The tearing at the edge occurred at the deformation of 54.36 mm and paused the testing machine.

The delamination and falling of the glass fragments from the PVB interlayer on the specimens tested at a temperature of 20 °C were manifested by the formation of small decreases in force. Apart from this, the force was gradually increasing with the deformation and, subsequently, with the formation of a tearing of the PVB interlayer; its slow propagation created a plateau. The maximum force reached ranged between 2.61 and 3.72 kN.

Although the course of the dependence of the force and deformation was significantly influenced by the temperature in the experiment, the maximum forces reached had similar values. As the maximum force was reached on the ANG1, ANG2 and ANG3 specimens the maximum value of the force exerted by the testing machine $F_{1.abs}$ was achieved. As the maximum force was reached on the ANG4 and ANG5 specimens the maximum force achieved in the "constant" section" $F_{2.abs}$ occurred. The lowest value of 2.61 kN was obtained on the ANG2 specimen. The maximum force on the specimens ANG1, ANG3, ANG4, ANG5 ranged between 3.37 and 3.72 kN. These maxima occurred at the deformations from 21.55 to 36.19 mm; subsequently, the PVB interlayer was gradually tearing.

For design purposes it would be helpful to define the limit deformation (or deformation range); before reaching this limit, the prescribed resistance of the laminated glass with both glass plies broken had to be achieved. For the ANG1, ANG2 and ANG3 samples that were tested at a temperature of 20°C, this limit deformation value would be 27.2 mm; for the ANG4 and ANG5 samples tested at a temperature of 10°C, it would be 21.5 mm (the minimum of the deformation values at the maximum forces achieved).

The maximum deformation before the complete tearing of the PVB interlayer ranged from 44.43 to 56.37 mm, with the exception of the value of 81.20 mm, which was achieved on the ANG5 sample.

After breaking both glass plies of the specimens made from thermally-toughened glass (TTG), the experiment continued from the value of the force to which it dropped at the breakage of the glass plies; see the drop of the force exerted by the testing machine $F_{1.abs}$ in Fig. 6. These minima are summarized in Tab. 4. The negative force on the TTG4 specimen was created by automatic control of the testing machine through the sudden release of the specimen during the "explosive" failure. The possible slight expansion of the specimen due to its fracture into small fragments would probably not have such an effect.

Fig. 6 shows the dependence of the absolute force $F_{1.abs}$ exerted by the testing machine and the total deformation $d_{1.abs}$ of the experimental assembly. These data were obtained directly from the testing machine. Fig. 7 shows the dependence of the F_1 "force increase", i.e., the increment of the force from the initial value at the moment after the failure of both glass plies, and the deformation of the d_1 glass specimen itself; see Formulas (1) and (2).

The absolute values of the $F_{1.abs}$ maximum force that the specimen was able to carry ranged from 1.04 to 1.19 kN, except for the TTG4 specimen with a lower value of 0.64 kN, see Tab. 6. The value of the F_1 force by which the load acting on the specimens had a rising trend ranged from 0.35 to

Tab. 6 *Maximum forces and corresponding deformations achieved after the breakage of both plies of glass: specimens made from thermally-toughened glass (TTG)*

Specimen	Max. force				Loading	The failed hole
	$F_{1.abs}$ [kN]	F_1 [kN]	$d_{1.abs}$ [mm]	d_1 [mm]	rate [mm/min]	
TTG1	1.19	0.35	56.79	51.64	2	B
TTG2	1.17	0.49	89.89	84.82	2	A
TTG3	1.06	0.79	95.98	90.92	4	B
TTG4	0.64	0.73	93.24	88.57	4	A
TTG5	1.04	0.43	61.83	55.11	2	A

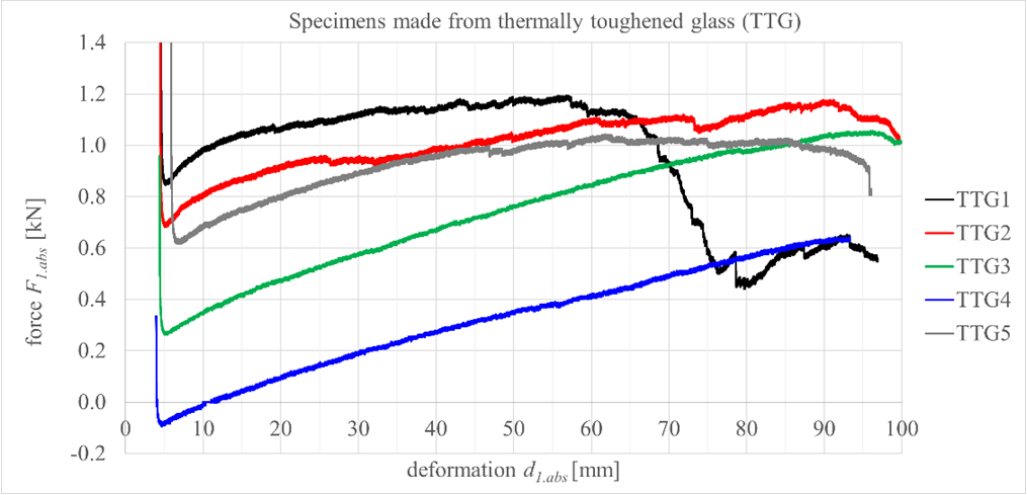

Fig. 6 *Dependence of the force deformation (force exerted by the testing machine $F_{1.abs}$, total deformation of the experimental assembly $d_{1.abs}$) on the specimens made from thermally-toughened glass (TTG)*

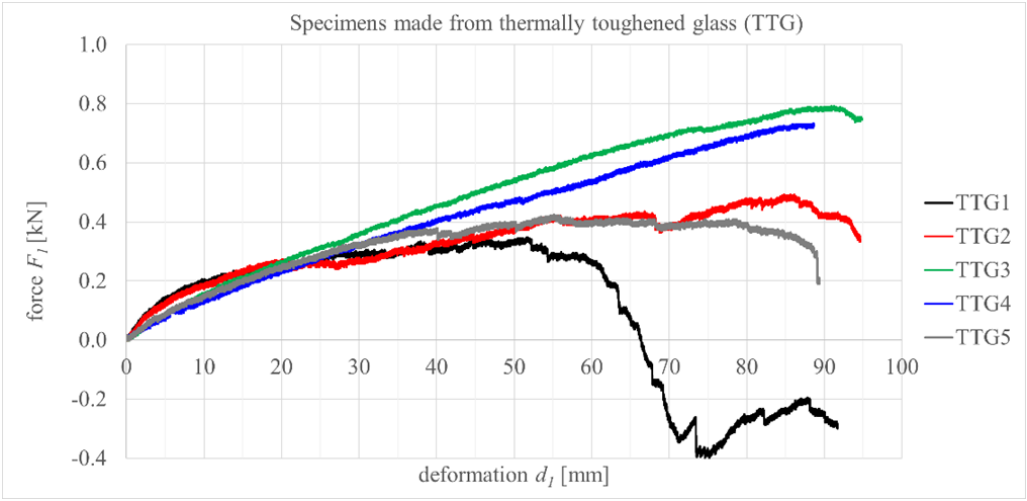

Fig. 7 *Dependence of the force deformation (the "force increase" F_1, deformation of the glass specimen itself d_1) on the specimens made from thermally-toughened glass (TTG)*

0.49 kN for a loading speed of 2 mm/min. On the TTG1 specimen, the breakage emerged at the hole B located at the top and on the TTG2 and TTG5 specimens at the hole A located at the bottom. Because of the difference in the shape of the fragments (in the case of the TTG1 specimen, the narrow needle-shaped fragments were by the upper hole), the area in compression above hole B did not retain its original position and leaned towards the metal plate. This led to a decrease in the force at higher rates of deformation, see Figs. 6 and 7. If there were no steel plates, there would probably be a complete collapse of the area above hole B and thus the complete failure of the specimen.

On specimens loaded at a speed of 4 mm/min (TTG3, TTG4), the force continuously increased with deformations up to a deformation of approximately 85 mm. The force increased by 0.79 kN from the initial value in the case of the TTG3 specimen and by 0.73 kN in the case of the TTG4 specimen. On the TTG3 specimen, a glass fracture emerged at hole B and at hole A on the TTG4 specimen. In the case of a higher loading speed, the location of the initiation of the cracks had no effect on the course of the dependence of the force and the deformation.

3.4 Numerical analysis – calculation of the expected strength of the glass

A 3D model of the system, consisting of steel bolts with a diameter of 14 mm, a polyamide insert with a thickness of 3 mm, and laminated glass with the same dimensions and composition as in the experiment, was created using Ansys Workbench 2019 R1.

The glass, steel, polyamide, and PVB interlayers were defined as linear elastic materials. Fixed support was applied to the shear planes of the bolt in hole A. The force and support that allow movement only in the direction of the force applied were applied to the shear planes of the bolt in hole A. The total force applied was divided on the shear planes in different ratios (50:50, 60:40, 70:30, 81:19, 91:9) to capture any imperfections of the test set-up.

The contact between the bolts and the inserts was defined in all the models as a nonlinear contact, which was only transmitting pressure. The contact between the insert and the glass was defined as a fixed contact or as a nonlinear contact, which was only transmitting pressure.

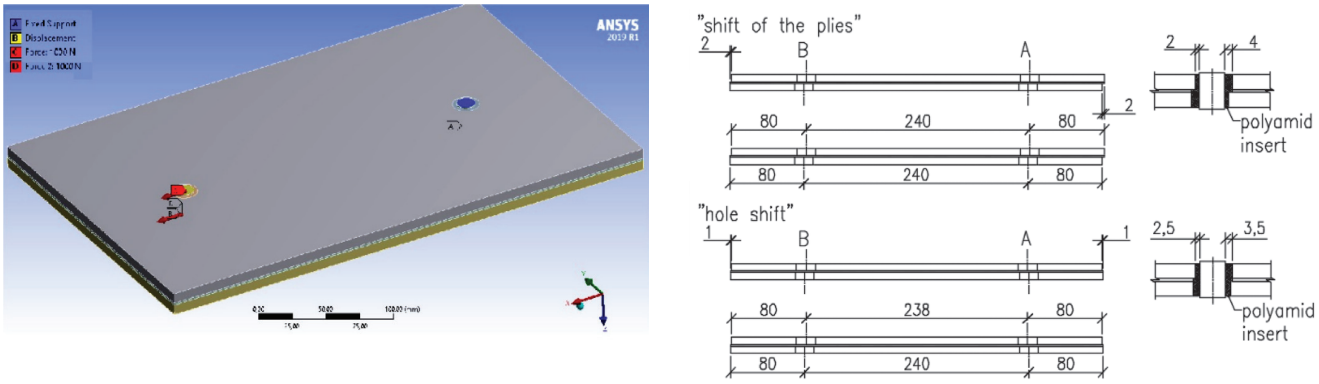

Fig. 8 *Numerical model and variations of the geometry*

To capture the imperfections of the sample, two more geometries of the glass specimen were created, i.e., "shift of the plies" and "hole shift", see Fig. 8.

The highest principal stress σ_1, which was decisive for the design of the glass member, occurred at the edge of the opening. It deviated 90° from the direction of the force applied and was orientated in the x-axis direction. The stresses σ_x in the direction *x* at a distance of 3.25 mm from the edge of the hole (the place of the strain gauge in the experiment) were also evaluated.

The maximum value of the principal stress σ_1 was 2.2 to 3.7 times higher than the value of the σ_x at a distance of 3.25 mm from the edge of the hole (the place of the strain gauge in the experiment). These values of the multiples were determined at forces of 2 kN, 4 kN, 6 kN, and 8 kN. The magnitudes of the loads achieved in the experiments with the specimens made from thermally-toughened glass (TTG) were not considered. Therefore, the following comparison is applicable only to the specimens made from annealed glass (ANG).

Two values of the strength of materials are defined in the Eurocodes, i.e., characteristics and design. The design value of the strength of the material is based on the characteristic value adjusted using several reduction factors, which take into account the possibilities of adverse deviations of the material's strength from its characteristic values, so that the probability of material failure is very low. The characteristic strength of the annealed glass is 45 MPa (thermally-toughened glass of 120 MPa). The design strength of the glass was calculated according to (Feldmann et al., 2023), and its value was 14.8 MPa.

As is shown in Tab. 7, the estimated value of the principal stress σ_1 at the creation of the first crack was 24.10 to 73.38 MPa.

It is necessary to note that, based on the numerical analysis, the ratio σ_1/σ_x at higher values of the load (6 kN, 8 kN) was ~ 4. Therefore, the value 3.7 σ_x (upper strength level) was considered for a comparison with the experiment. These values are in Tab. 7 and highlighted by bolt letters; their range is 35.05 to 73.38 MPa. Of the five specimens tested, only one value (35.05 MPa, ANG2) was lower than the characteristic glass strength $f_{g,k}$ of 45 MPa. In all the cases (also considering σ_1/σ_x = 2.2, where the lowest value was 24.10 MPa), the values of the estimated strength were higher than the design value of the glass strength $f_{g,d}$ of 14.8 MPa.

4 CONCLUSIONS

The focus of this paper was an experimental investigation of bolted connections in laminated glass. All the stages of the specimen were observed, i.e., from the intact state of the specimen to both plies of glass broken. Special attention was paid to the residual resistance of the specimen. An approximate relationship to the strength of the glass at the failure of the annealed glass specimen (ANG) was determined on the basis of the results of the numerical analysis. It is necessary to clarify that this relationship is valid only for the tested configuration in terms of the test set-up and the specimen's geometry.

Strain gauge measurements were used on the intact specimens (stage I.) to determine the stress peaks on the sides

Tab. 7 *Estimated strength of the material at the time of failure*

Specimen	Force* [kN]	Stress in the location of the strain gauge** σ_x [MPa]	Principal stress $\sigma_1 = 2.2\ \sigma_x$ (lower strength level) [MPa]	Principal stress $\sigma_1 = 3.7\ \sigma_x$ (upper strength level) [MPa]
ANG1	6.25	15.78	34.71	**58.38**
ANG2	6.68	10.95	24.10	**35.05**
ANG2-B	9.03	19.83	43.63	**73.38**
ANG3	6.86	12.68	27.90	**46.92**
ANG3-A	6.86	17.56	38.63	**64.97**
	* the force at the creation of the first crack ** stress at the location of the strain gauge placed at the location of the first crack			

of the holes to capture the distribution of the load on the individual plies of glass. As expected, the force was not evenly distributed on both layers of glass. The distribution of the stresses indicated the manner of the crack pattern on the annealed glass, i.e., whether the cracks appeared only by one hole or by both holes.

The first crack on the specimens made from annealed glass (ANG) occurred at approximately 4.5 times lower force applied than on the specimens made from thermally-toughened glass (TTG).

Stage II. included the period from the appearance of the first crack to the appearance of the last crack at the hole with one layer already broken. After the formation of the first crack, four of the seven specimens made from annealed glass (ANG) were able to carry a higher load than in the intact state. In one case of a specimen made from annealed glass (ANG), simultaneous breakage of both plies of glass appeared. In the remaining two cases, the partially broken specimen was able to carry 80% to 99% of the force at the appearance of the first crack.

Since the glass ply that cracked first carried more of a load, the remaining ply had sufficient capacity to carry an increased load after the development of the first crack. It can be assumed that the first crack occurred at the weakest point, which was the result of the combination of the critical surface flaw and the peak of the higher stress at the hole. The holes of the remaining glass ply could have had a higher surface quality or the critical flaw could have been located further from the stress peaks in the hole. These phenomena could be the explanation for the higher resistance of the partially broken sample. Both plies of glass of the specimens made from thermally-toughened glass (TTG) were broken at the same time; stage II. did not occur.

In stage III. the integrity of the specimen was ensured only by the PVB interlayer. On the specimens made from annealed glass (ANG), the effect of the temperature was studied. The temperature had a significant effect on the course of the dependence of the force and deformation, but the values of the maximum forces reached were similar. They were 1.7 to 2.6 times lower than the resistance of the unfractured specimens.

The limit value of the deformation up to which the force acting on the specimen increased or was kept at a constant level was determined to be 27.2 mm for the specimens tested at a temperature of 20 °C and 21.5 mm for the specimens tested at a temperature of 10 °C. After reaching this deformation value, the tearing of the PVB interlayer started, which led to the complete failure of the specimen.

The specimens made from thermally-toughened glass (TTG) showed very low residual resistance. The absolute value of the maximum force reached was 23 to 43 times lower than the resistance of the unfractured specimens. Compared to the specimens made from annealed glass (ANG), the residual resistance of the specimens made from thermally-toughened glass (TTG) was approximately 3.3 times lower. At a loading rate of 2 mm/min, the dependence of the force and deformation was affected by the location of the hole where the failure occurred (the hole where narrow needle-shaped fragments formed). If this opening was placed on the top, there was a collapse of the area above the bolted connection that leaned against the steel plate. Therefore, it can be stated that the difference in the pattern of the glass fragments of the thermally-toughened glass could unfavourably affect the residual resistance. At a higher loading speed of 4 mm/min, this phenomenon did not occur.

It can be concluded that the use of laminated glass consisting of thermally-toughened glass significantly increases the resistance of the intact glass element, but that the residual resistance is low. The specimens made from annealed glass (ANG) with larger fragments performed better in stage III. than the specimens made from thermally-toughened glass (TTG). In practice, the use of annealed glass for glass structural elements with a bolted connection is not recommended due to its low strength. Heat-strengthened or thermally-toughened glass has to be used for the application of laminated glass panels with holes. The advantage of the heat-strengthened glass is a similar type of breakage pattern as for annealed glass and a higher strength compared to annealed glass.

It was considered beneficial to determine the values of the expected strength of the glass by the hole based on the numerical analysis. A set of numerical models with a variety of imperfections was created, and the range of the multiples of the stress at the location of the strain gauge was determined to express the expected principal stress at the edge of the hole of the specimens made from annealed glass (ANG), where the crack originated. Among the five annealed glass (ANG) specimens, there was only one specimen whose value of the upper strength level calculated was lower than the characteristic strength of the glass. In all the cases, the value of the lower strength level was above the value of the design strength of the glass.

Acknowledgements

This work was supported by the Scientific Grant Agency of the Ministry of Education, Science, Research and Sports of the Slovak Republic under the programme VEGA 1/0397/22.

The glass specimens were provided by AGC Glass Europe.

REFERENCES

Belis, J. - Depauw, J. - Callewaert, D. - Delincé, D. - Van Impe, R. (2009) *Failure Mechanisms and Residual Capacity of Annealed Glass/SGP Laminated Beams at Room Temperature.* Engineering Failure Analysis, 16 (6), pp. 1866–1875. DOI: 10.1016/j.engfailanal.2008.09.023.

Bennison, S. J. - Stelzer, I. (2009) *Structural Properties of Laminated Glass.* In: Short Course, Glass Performance Days, Tampere (Finland).

Bennison, S. J. - Smith, C. - Duser, A. - Jagota, A. (2002) *Structural Performance of Laminated Glass Made with a "Stiff" Interlayer.* ASTM Special Technical Publication, pp. 57–65. DOI: 10.1520/STP11056S.

D'Ambrosio, G. - Galuppi, L. - Royer-Carfagni, G. (2019) *Post-Breakage in-Plane Stiffness of Laminated Glass: An Engineering Approach.* Glass Structures and Engineering, 4 (3), pp. 421–432. DOI: 10.1007/s40940-019-00099-1.

Delincé, D. - Callewaert, D. - Belis, J. - Van Impe, R. (2008) *Post-Breakage Behaviour of Laminated Glass in Structural Applications.* In: Challenging Glass 1, Delft (The Netherlands). DOI: 10.7480/cgc.1.

Delincé, D. - Callewaert, D. - Belis, J. et al. (2010) *Influence of Temperature on PostBreakage Behaviour of Laminated Glass Beams: Experimental Approach.* In: Challenging Glass 2 - Conference on Architectural and Structural Applications of Glass, Delft (The Netherlands), pp. 407–414. DOI: https://doi.org/10.7480/cgc.2.2338.

Feldmann, M. - Laurs, M. - Belis J. et al. (2023) *The New CEN/TS 19100: Design of Glass Structures.* Glass Structures and Engineering. DOI: 10.1007/s40940-023-00219-y.

Ferretti, D. - Rossi M. - Royer-Carfagni, G. (2012) *Through-Cracked Tensile Delamination Tests with Photoelastic Measurements.* In: Challenging Glass 3: Conference on Architectural and Structural Applications of Glass, Delft (The Netherlands), pp: 641–652. DOI: 10.3233/978-1-61499-061-1-641.

Galuppi, L. - Royer-Carfagni, G. (2016) *A Homogenized Model for the Post-Breakage Tensile Behavior of Laminated Glass.* Composite Structures, 154, pp. 600–615. DOI: 10.1016/j.compstruct.2016.07.052.

Galuppi, L. - Royer-Carfagni, G. (2018) *The Post-Breakage Response of Laminated HeatTreated Glass under in Plane and out of Plane Loading.* Composites Part B: Engineering, 147, pp. 227-239. DOI: 10.1016/j.compositesb.2018.04.005.

Kott, A., - Vogel. T. (2004) *Controlling the Post-Breakage Behavior of Laminated Safety Glass.* In: Proceedings of International Symposium on the Application of Architectural Glass, Monaco.

Kreher, K. (2004) *Tragverhalten Und Bemessung von Holz-Glas-Verbundträgern Unter Berücksichtigung Der Eigenspannungen Im Glas.* Lausanne: EPFL. 241 pp. DOI: 10.5075/epfl-thesis-2999.

Louter, C. (2007) *Adhesively Bonded Reinforced Glass Beams.* HERON, 52 (1/2). ISSN 0046-7316.

Overend, M. - De Gaetano, S. - Haldimann. M. (2007) *Diagnostic Interpretation of Glass Failure.* Structural Engineering International, 17 (2), pp. 151–158. DOI: 10.2749/101686607780680790.

Palumbo, M. (2005) *A New Roof for the XIIIth Century 'Loggia de Vicari' (Arquà Petrarca -PD – Italy) Based on Structural Glass Trusses: A Case Study.* In: Proceedings of Glass Processing Days. Tampere (Finland).

Pourmoghaddam, N., - J. Schneider, J. (2018) *Experimental Investigation into the Fragment Size of Tempered Glass.* Glass Structures and Engineering, 3 (2), pp. 167–181. DOI: 10.1007/s40940-018-0062-0.

Pourmoghaddam, N. - Kraus, M. - Schneider, J. - Siebert, G. (2018) *The Geometrical Properties of Random 2D Voronoi Tesselations for the Prediction of the Tempered Glass Fracture Pattern.* Ce/Papers, 2 (5–6), pp. 325–339. DOI: 10.1002/cepa.934.

Ryan, P. - Otlet, M. - Ogden, R. G. (1997) *Steel Supported Glazing Systems*. Ascot: The Steel Construction Institute, 1997. 74 pp. ISBN 1 85942070 2.

Slivanský, M. (2012) *Experimental verification of the resistance of glass beams.* Slovak Journal of Civil Engineering, 20 (1), pp. 21-28. DOI: 10.2478/v10189-012-0003-x.

Štiglic, M. (2015) *Optimálny návrh konštrukcií s uvážením jednostranných väzieb [Design optimization of structures with consideration of unilateral bonds]*. [Dissertation thesis, Faculty of Civil Engineering, Slovak University of Technology in Bratislava, SK] [in Slovak].

Wurm, J. (2007) *Glass Structures*. Basel: Birkhäuser Verlag AG., 2007. 255 pp. ISBN 978-3-7643-7608-6.

Zhang, X. - Hao, H. - Ma, G. (2015) *Dynamic Material Model of Annealed Soda-Lime Glass.* International Journal of Impact Engineering, 77, pp. 108–119. DOI: /10.1016/j.ijimpeng.2014.11.016.

Zhao, C. - Yang, J. - Wang, X. - Azim, I. (2019) *Experimental Investigation into the PostBreakage Performance of Pre-Cracked Laminated Glass Plates.* Construction and Building Materials, 224, pp. 996–1006. DOI: 10.1016/j.conbuildmat.2019.07.286.

sciendo

Slovak Journal of Civil Engineering

Vol. 32, 2024, No. 2, 21 – 26
DOI: 10.2478/sjce-2024-0010

EXPERIMENTAL MEASUREMENTS IN SCHOOLS WITH NATURAL VENTILATION

Pavol ŠTEFANIČ[1]*, Zuzana STRAKOVÁ

Abstract

Facilities for children and young people should be established in a healthy environment that is protected from external health-damaging factors, such as noise, air pollution, and negative educational influences. A school building should also be a safe and healthy environment for pupils and students, as legally required. However, although some school buildings have been renovated, most were constructed in the last century, and their indoor microclimate remains unsatisfactory. Schools must maintain optimal thermal and humidity conditions to ensure the healthy development of children and their ability to function properly in a classroom. While natural ventilation through opening windows is a good practice, it may not always guarantee sufficient air exchange, especially for schools located in busy traffic areas. This paper presents experimental measurements and a comparison between two primary schools in Bratislava, which describes the current thermal and humidity conditions in the indoor environment of both schools. Experimental measurements were carried out on five school days in each primary school to determine the thermal-humidity conditions and indoor air quality, depending on the concentrations of carbon dioxide.

Address

[1] Dept. of Building Services, Faculty of Civil Engineering, Slovak University of Technology in Bratislava, Bratislava, Slovakia

* ***Corresponding author:*** pavol.stefanic@stuba.sk

Key words

- Natural ventilation,
- school,
- indoor air quality,
- temperature,
- relative humidity,
- concentration of carbon dioxide.

1 INTRODUCTION

Ventilation, or exchanging air between indoor and outdoor spaces, can occur naturally, artificially, or through a combination of both. Inadequate ventilation poses a significant risk to indoor air quality, which is a crucial factor for the comfort and health of a building's occupants. The effectiveness of ventilation plays a key role in shaping indoor air quality. Slovak regulations specify two ways of measuring ventilation: either as the amount of outside air supplied, for example, in l/s per person or l/s per m^2 of floor area, or as the number of air changes per hour (STN EN 16798-1:2019). Other factors affecting air distribution should also be taken into consideration, particularly the production of pollutants, the number of people in the space, their activities, the materials used, the temperature and relative humidity of the indoor air, and the effectiveness of the ventilation (Junasová and Krajčík, 2020).

The aim of the experimental measurements was:

- To verify whether the temperature and relative humidity of the indoor air and the concentration of carbon dioxide (CO_2) on the premises of primary schools meet the requirements set out in the relevant legal documents and technical standards.
- Assess whether the legal and standard requirements are met, and if not, determine the reasons for the school's non-compliance.

2 NATURAL VENTILATION

A ventilation system provides fresh air to the indoor space of a building and removes air contaminated with harmful substances or excess heat. Natural ventilation is a type of ventilation that occurs through the exchange of air in a room due to natural forces. The forces are a result of external climatic conditions, and they create a difference in pressure between the external and internal environments, thereby causing air movement. These forces include gravitational force (pressure) and wind. These two principles are applied in the natural ventilation of residential and administrative buildings, such as:

- infiltration,
- aeration,
- ventilation through windows (Székyová et al., 2004).

However, in real environmental conditions where a building is located, this transformation is influenced by several other factors. Apart from wind speed and direction, other factors that affect natural ventilation in residential and administrative buildings include the building's shape and position, the configuration of the surrounding terrain, the shape and position of any obstacles in front of the building, etc. (Gebauer et al., 2007; Dokoupilová and Horák,2023).

2.1 Infiltration

Infiltration ventilation is the process of replacing indoor air with outside air. This occurs due to overpressure from the external side created by leaks in a building envelope and the pores of the building materials.

The primary air exchange happens through open windows or external doors. The overpressure is caused by difference in temperature between the indoor and outdoor environments, as well as the action of wind.

The calculation of the volumetric flow rate Q of infiltrated air entering a room through the length l of the joints of the opening sashes of windows and doors is as follows:

$$Q = i \times l \times \Delta p^n \quad (\mathrm{m^3/s}) \tag{1}$$

where:

- i – joint air permeability coefficient ($(\mathrm{m^3/(s.m.Pa^n)})$),
- l – length of the joints (m),
- n – exponent characterising the airflow through the joint (-); normally $n = 0.67$,
- Δp – difference in pressure due to difference in temperature Δp_θ and action of wind Δp_w (Pa),
- $\Delta p_t = h \times g \times (\rho_e - \rho_i)$ (Pa),
- $\Delta p_w = 0.5 \times A \times w_v^2 \times \rho_e$ (Pa),
- ρ_e – density of the outdoor air ($\mathrm{kg/m^3}$),
- ρ_i – density of the indoor air ($\mathrm{kg/m^3}$),
- A – aerodynamic coefficient of the building (-),
- w_v – wind velocity (m/s) (Chyský and Hemzal, 1993).

2.2 Ventilation through windows

Natural ventilation openings consist of windows, doors, dormer (monitor) vents, skylights, roof ventilators, chimneys, and specially designed supply or exhaust vents. Windows allow light and provide ventilation when open. They can be opened vertically or horizontally or can be hinged at the top, bottom, or on the side. The type of rotation used is important for weather protection and affects the velocity of the airflow (ASHRAE Handbook, 2009).

Window ventilation is the most common method of natural ventilation for rooms. The volume flow rate of the supply air Q_t is calculated based solely on the effect of the temperature. This calculation is derived from the issue of aeration, with the assumption that a single opening, i.e., the window, is used for both supply and exhaust air (Fig. 1):

$$Q_t = \frac{2 \times \mu \times a}{3 \times \rho_s} \sqrt{\frac{2 \times \rho_e \times \rho_i (\rho_e - \rho_i) \times g \times b^3}{\left(\rho_e^{0.33} + \rho_i^{0.33}\right)^3}} \quad (\mathrm{m^3/s}) \tag{2}$$

where:

- μ – flow coefficient (-),
- a – window width (m),
- b – window height (m),
- ρ_s – mean air density ($\mathrm{kg/m^3}$),
- ρ_e – outdoor air density ($\mathrm{kg/m^3}$),
- ρ_i – indoor air density ($\mathrm{kg/m^3}$),
- g – gravitational acceleration ($\mathrm{m/s^2}$) (Hirš and Gebauer, 2006).

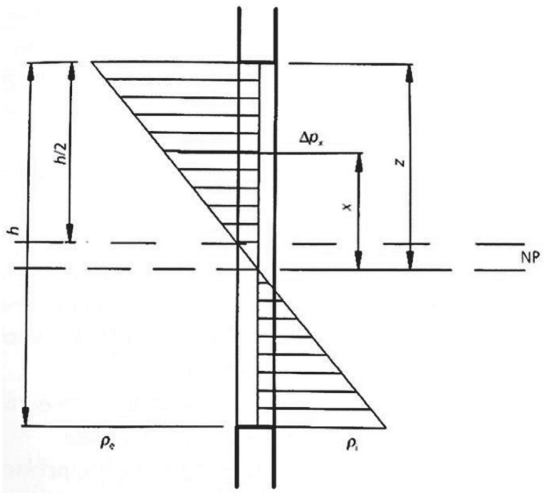

Fig. 1 *The distribution of pressures within a window opening in response to gravitational forces (Székyová et al., 2004)*

Ventilation rates are affected by various aspects of wind, including the average speed, prevailing direction, seasonal and diurnal variations in the speed and direction, and local obstructions such as nearby buildings, hills, trees, and shrubbery. Natural ventilation systems are typically designed for wind speeds equal to half the seasonal average. It is important to note that wind speeds may be lower in the summer than in the winter and that the direction may also vary, depending on the season. Equation (3) provides the air flow rate of wind-displaced air Q_w through ventilation openings or determines the appropriate size of openings to achieve a desired air flow rate:

$$Q_w = C_v \times A \times w_v \quad (\mathrm{m^3/s}) \tag{3}$$

where:

- C_v – efficiency of the openings (C_v is assumed to be 0.5 to 0.6 for perpendicular wind and 0.25 to 0.35 for any diagonal flow through the openings) (-),
- A – free area of the inlet openings ($\mathrm{m^2}$),
- w_v – wind velocity (m/s) (ASHRAE Handbook, 2009).

Fig. 2 *Vaisala sensor on the HOBO data logger case*

3 EXPERIMENTAL MEASUREMENTS

The measurements of the selected indoor environmental parameters were performed in two primary schools. Each measurement lasted for 5 working/school days, from Monday to Friday, in one classroom of each school.

The measurements of the indoor air temperature, relative indoor humidity, and CO_2 concentration were taken using a Vaisala type GMW90 sensor and a HOBO type 4 data logger (Fig. 2).

The Vaisala sensor has an air temperature measurement range of -5 °C to +55 °C with an accuracy of ±0.6 °C at +10 °C to 30 °C. Relative humidity can be measured from 0 - 95 % with an accuracy of ±2.5 % at 0 % - 60 %, ±3.0 % at 60 % - 80 %, and ±4.0 % at 80 - 95 %. The CO_2 concentration can be measured in the range of 0 ppm - 5000 ppm with an accuracy of ±35 ppm at +10 °C to +30 °C (available online: VAISALA).

The HOBO data logger supports the collection, storage, and analysis of data from the Vaisala sensor using the HOBOware software. The operating range of the data logger is from -20 to +70 °C and from 0 to 95 % relative humidity. Recording intervals can be set from 1 second to 18 hours. The logger has a memory of 4 MB, which is equivalent to approximately 1.9 million measurements (available online: HOBO).

The selected variables were measured in Bratislava between 16.–20.01.2023 and 30.01.–03.02.2023, from Monday to Friday in both schools. The measurements were taken from the Monday before school started until the Friday after it began.

The indoor air temperature, relative humidity, and CO_2 concen-tration were recorded every 5 minutes. The outdoor conditions during the experimental measurements i.e., the outdoor air tem-perature and humidity, wind speed are shown in Tab. 1. We assumed the default outside the concentration average is 400 ppm (350 ppm - 500 ppm) (STN EN 16798-1:2019).

The classrooms were ventilated by opening the windows for short periods. However, the exact position of the windows was not determined as the ventilation was based on the subjective feeling of the teacher. There are two types of window openings in the classrooms, i.e., opening and tilting.

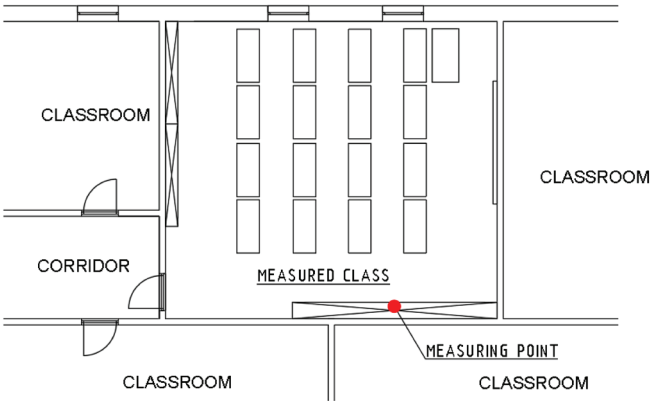

Fig. 3 *Example of placement of a measuring device in a classroom*

Tab. 1 *Outdoor air parameters and number of pupils. Outdoor air temperature and humidity - Source of SHMÚ data. Wind velocity (available online: WUNDERGROUND)*

School	Date 2023	Outdoor air temperature range θ_e (°C)	Outdoor relative humidity range φ_e (%)	Wind velocity w_v (m/s)	Number of pupils
1	16.01. – 20.01.	-2.5 – 6.8	61 – 98	0.56 – 9.72	15
2	30.01. – 03.02.	-3.3 – 6.6	52 - 97	1.94 – 12.22	21

Continuous short-term measurements of the selected variables were taken in Years 5 and 6 of the primary school. In both classrooms, the upper part of a cupboard was chosen as the measurement site (Fig. 3), so as not to disrupt the flow of the classroom. All the students and teachers were informed about the ongoing measurements and asked to take extra care to avoid moving or damaging the measuring equipment.

4 ANALYSIS AND EVALUATION OF RESULTS

The following figures (Figs. 4 to 6) show the recorded waveforms of the physical parameters measured:

Tab. 2 *Results from the experimental measurements in each class*

School	Date 2023	Indoor air temperature range θ_i (°C)	Indoor relative humidity range φ_i (%)	Maximum concentration CO_2 (ppm)
1	16.1.-20.1.	18.7 – 25.9	34.7 – 55.8	2913
2	30.1.-03.2.	18.0 – 23.2	36.1 – 59.1	4649

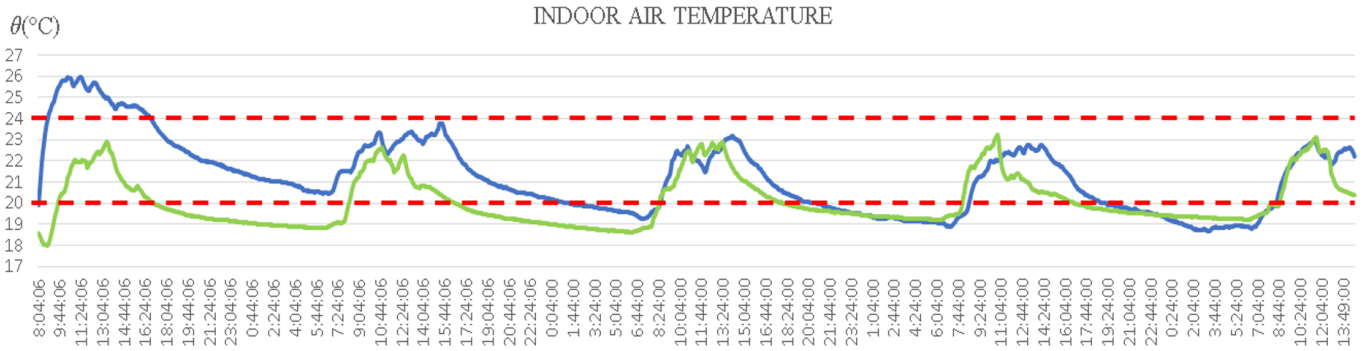

Fig. 4 *Indoor air temperature in both schools with limit values marked*

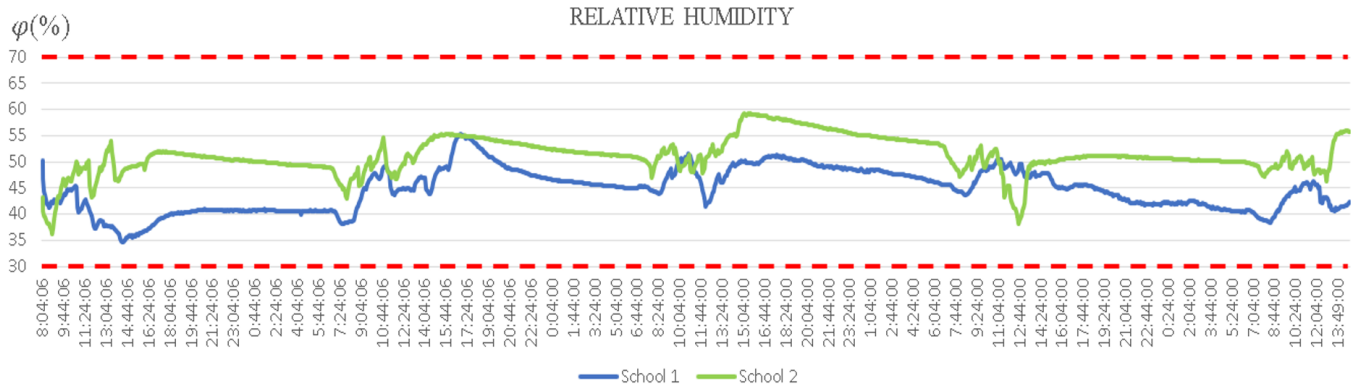

Fig. 5 *Indoor relative humidity in both schools with limit values marked*

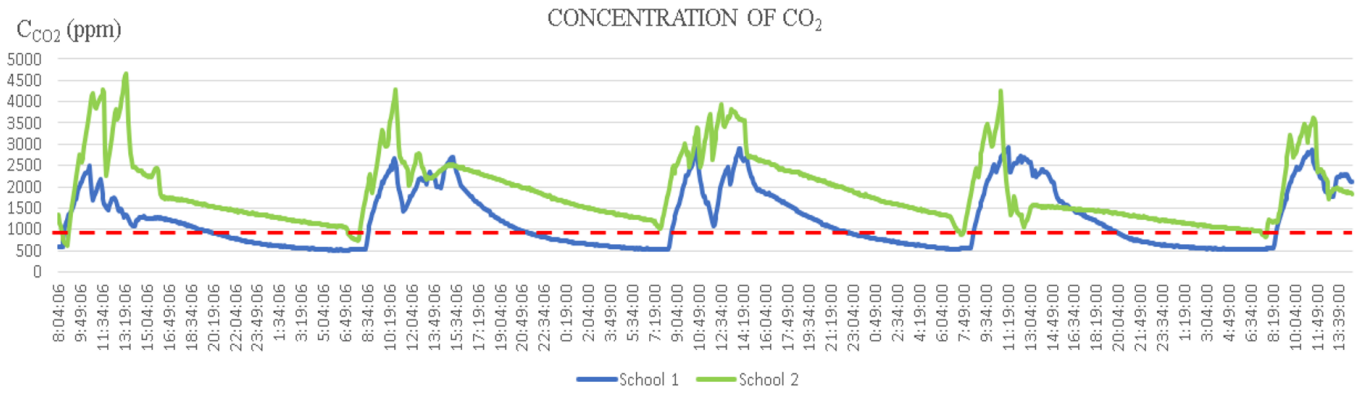

Fig. 6 *CO_2 concentration in both schools with limit values marked*

The temperature in the classrooms (as shown in Tab. 2) met the requirements set out in the relevant legal and technical regulations (Tab. 3), as it remained between 20 °C and 24 °C during the cold season measurements. However, at certain times during the cold season, the indoor air temperature exceeded the recommended values defined by Decree No. 259/2008 Coll., in School 1 on the first day (almost 26 °C) and in both schools in the evening when the pupils had left the classroom, when the temperature dropped outside the optimum range. While that environment could be considered acceptable, it was not ideal in terms of the thermal conditions.

The indoor relative humidity was kept between 30 - 70 % during the measurement period.

The indoor air quality in each classroom was partially acceptable according to the legal and technical requirements, but once the pupils were in the classroom, the CO_2 concentration values were several times higher than the recommended limit (Tab. 4). The CO_2 concentration curve shows a decrease in the CO_2 concentration, which we cannot substantiate because the natural ventilation conditions were not controlled. The reason for the decrease was unknown. The decrease could have occurred when doors or windows were opened, if the number of pupils in the classroom changed, or if the classroom had emptied for a physical education lesson. We can see that in School 2, we would not have achieved the desired CO2 value even after the pupils left the classroom after school.

5 DISCUSSION AND CONCLUSION

The overall quality of the indoor environment in school buildings is crucial, mainly because of the requirements for concentrated work and cognitive functioning in learning. At the same time, ensuring a good indoor environment in schools should be part of a systemic approach to promoting quality education and learning for children, this approach includes the education system itself, healthy eating and sufficient exercise, and the quality of the environment in which children are educated.

According to Heracleous and Michael (2019), thermal comfort in primary schools is not the problem, as these experimental measurements show, but the CO_2 concentration is. In Schibuola et al. (2016), the measures show the criticality of IAQ with values often much higher than the limits specified by the standard, but also the possibility of acting effectively with the manual ventilation without excesses that could create problems of comfort or a waste of energy.

It would also be useful to assess the results while a class was being taught, when the pupils were in the classroom, or on individual days of the week, and record when windows were opened, for how long, and what their position was.

The best and cheapest solution to this problem would probably be to place CO_2 sensors in the classrooms and control the manual ventilation accordingly.

Tab. 3 *Thermal-humidity microclimate parameters for classrooms (Decree of the Ministry of Health of the Slovak Republic No. 259/2008 Coll.)*

Room	Operative temperature θ_o (°C)	Relative humidity φ (%)	Air change rate n (h^{-1})
Facilities for children and youth			
classrooms, games rooms, living rooms	20 to 24	30 to 70	3 to 8

Tab. 4 *Default design CO2 concentration above the outdoor concentration (400 ppm), assuming a standard CO2 emission of 20 l/(h/person) (STN EN 16798-1:2019)*

Category	Corresponding CO2 concentration above ambient air concentration for non-adapted persons (ppm)
I	**550**

Acknowledgements

This work was supported by the Research and Development Support Agency of Slovakia through project APVV-21-0144.

REFERENCES

ASHRAE Handbook (2009) – Fundamentals, SI Edition, American Society of Heating, Refrigeration and Air-Conditioning Engineers, Atlanta, GA, USA. 1000 pp. ISBN: 978-193-9742-54-0

Chyský, J. – Hemzal, K. et al. (1993) *Větrání a klimatizace (Ventilation and air conditioning)* Brno, CZ: Bolit. 560 pp. ISBN 80-901574-0-8

Decree of the Ministry of Health of the Slovak Republic No. 259/2008 Coll. on details of requirements for the internal environment of buildings and on minimum requirements for lower standard flats and accommodation facilities.

Dokoupilová, V. – Horák, P. (2023) *Studie renovace stávajících rodinných domů do energetické kategorie „D" podle budoucích požadavků EU (Study of renovation of existing family houses to energy category "D" according to future EU requirements)* In: TZB-info Available online: https://www.tzb-info.cz/energeticka-narocnost-budov/25380-studie-renovace-stavajicich-rodinnych-domu-do-energeticke-kategorie-d-podle-budoucich-pozadavku-eu

Gebauer, G. – Rubinová, O. – Horká, H. (2007) *Vzduchotechnika (Ventilation)*. Brno, CZ: ERA group, spol. s r.o., 146 pp. ISBN: 978-7366-091-8

Hirš, J. – Gebauer, G. (2006) *Vzduchotechnika v příkladech 1 (Ventilation in exercises 1. Building environment) Prostředí budov*. Brno, CZ: Akademické nakladatelství CERM. 230 pp. ISBN 80-7204-486-9

Heracleous, C. – Michael, A. (2019) *Experimental assessment of the impact of natural ventilation on indoor air quality and thermal comfort conditions of educational buildings in the Eastern Mediterranean region during the heating period.* In: Journal of Building Engineering 2019, Vol. 26, ISSN 2352-7102

HOBO Available online: https://www.onsetcomp.com/products/data-loggers/ux120-006m#specifications

Junasová, B. – Krajčík, M. (2020) *Výpočet dávky vzduchu pre nebytové priestory alebo koľko vzduchu treba na vetranie kancelárií? (Calculation of the air dose for non-residential premises or how much air is needed to ventilate offices?)* In: Vzduchotechnika 2020. Bratislava: SSTP, pp. 34-39. ISBN 978-80-89878-64-2

Schibuola, L. – Scarpa, M. – Tambani, C. *Natural ventilation level assessment in a school building by CO2 concentration measures.* In: Energy Procedia 2016, Vol. 101, pp. 257-264. ISSN 1876-6102

SHMÚ – Slovenský hydrometeorologický ústav (Slovak Hydrometeorological Institute) https://www.shmu.sk/sk/?page=1

STN EN 16798-1:2019 Energy performance of buildings - Ventilation for buildings - Part 1: Indoor environmental input parameters for design and assessment of energy performance of buildings addressing indoor air quality, thermal environment, lighting and acoustics - Module M1-6

Székyová, M. – Ferstl, K. – Nový, R. (2004) *Vetranie a klimatizácia (Ventilation and air conditioning)* Bratislava: Jaga, 2004. 422 pp. ISBN 80-8076-000-4

VAISALA. Available online: https://docs.vaisala.com/v/u/B211296EN-F/en-US

World Health Organisation (WHO) Available online: https://www.who.int/news-room/feature-stories/detail/what-are-the-who-air-quality-guidelines

WUNDERGROUND Available online:

https://www.wunderground.com/weather/sk/bratislava/48.15,17.11

sciendo

Slovak Journal of Civil Engineering

Vol. 32, 2024, No. 2, 27 – 37
DOI: 10.2478/sjce-2024-0011

SOME PROPERTIES OF A CEMENTITIOUS MORTAR CONTAINING GRANULATED RUBBER WASTE AND BRICK FILLERS: AN EXPERIMENTAL STUDY, MATHEMATICAL MODELING AND OPTIMIZATION

Salima BOUKOUR[1,2], Brahim LAFIFI[1*], Mohamed Larbi BENMALEK[1]

Abstract

The objective of this study is to assess the impact of incorporating rubber tire waste and brick fillers as a substitute for sand in cement mortar samples. The evaluation includes measurements of the bending strength, dynamic modulus of elasticity, and displacement. The replacement of sand by rubber waste (RW) and brick waste (BW) at 0%, 10%, 20% and 30% for rubber waste and 0%, 2.5%, 5.0%, 7.5%, and 10% for brick waste by volume was experimentally conducted. According to the findings, the introduction of rubber waste leads to a significant reduction in the flexural strength, dynamic modulus of elasticity, and displacement. The brick waste can be considered a suitable filler, which minimizes the negative effect of rubber tires and tends to result in suitable mixtures. The optimal values (10.10% for the RW and 10% for the BW) showed good agreement with the experimental results, with differences of 1.85%, -4.73%, and -4.48% for the displacement, flexural strength, and dynamic elastic modulus, respectively.

Address

[1] Dept.of Civil Engineering and Hydraulics, University 8 Mai1945 Guelma, Guelma, Algeria.

[2] University Center of Abdelhafid Boussouf, Mila, Algeria.

[*] ***Corresponding author:*** blafifi@gmx.fr

Key words

- Sand,
- Rubber tire waste,
- Brick filler waste,
- Flexural properties,
- RSM,
- Optimization.

1 INTRODUCTION

Due to the rapid development of modern civilization and limited natural resources, which can lead to potential shortages of raw and conventional building materials, recycled materials are becoming increasingly important in the construction industry. Recycled materials used in concrete can help to conserve non-renewable natural resources and decrease the need for costly landfills (Pelisser et al. 2011; Batayneh et al., 2008). Examples of waste materials that can be used in concrete include recycled plastics, rice husk ash, waste glass, and wood ash (R. Mahla, and R.P. Mahla, 2015).

Rubber waste is considered one of the most significant environmental challenges faced by municipalities worldwide because it is not easily biodegradable, even after prolonged treatment in landfills (Strukaret al., 2019). Globally, more than one billion tires are generated annually and have reached the end of their useful lives (Mohajerania et al., 2020). It is expected that more than 5,000 million tires will be discarded each year by 2030 (Sofi, 2018). Discarded scrap tires are often left untreated and accumulate in landfills or stockpiles. These deposits are considered hazardous because they pose potential threats to the environment and can also be fire hazards. Furthermore, these deposits provide suitable breeding conditions for rats, mice, cockroaches, and mosquitoes (Miller and Tehrani, 2017).

Efforts have been made to reduce the number of scrap tires in the environment by finding appropriate disposal methods and implementing recycling operations. Various projects have utilized waste scrap tires, such as in the production of asphaltic concrete mixtures (Rokade, 2012), construction materials (Presti, 2013), sports fields (Buši´ et al., 2018; Valente, 2019), reinforcement material in geotechnical works (Hidalgo and Hernández, 2020), and feed stock for making carbon black

(Thomas and Gupta, 2016). While it is technically possible to use tires as a source of fuel in the cement industry, it is neither economically nor environmentally attractive (Onuaguluchi and Panesar, 2014). Currently, only 5% of scrap tires are recycled into civil engineering applications (Serdaret al, 2014).

Studies have shown that adding tire rubber to concrete can improve its ductility and prevent brittle failures (Valente, 2019). Additionally, it has been shown to have significant performance at high temperatures (Shu and Huang, 2014) and produce lightweight structures compared to other materials (Sukontasukkul and Tiamlom, 2012). It also has excellent sound and thermal insulation properties (Zhang and Poon, 2018).

However, incorporating rubber particles into concrete can lead to undesirable changes in several material properties, such as the loss of mechanical strength (Ma andYue, 2013). These adverse effects have prompted researchers to develop various treatment methods to eliminate the negative effects of adding rubber to concrete.

According to (RedaTaha et al., 2008), the bond between rubber and cement paste can be weakened by the hydrophobic nature and surface texture of rubber, resulting in a decrease in strength. To counteract this negative effect, prior research has investigated different approaches, including improving the hydrophilic properties of rubber particles (Guo et al., 2017; Serdar et al., 2014). A commonly used technique to enhance the interfacial adhesion between rubber and a matrix prior to their incorporation into concrete is by pretreating the surface of rubber particles. Soaking the particles in a saturated NaOH solution has been identified as an effective approach (Guo et al, 2017). The use of alkaline solutions to modify the surface of rubber particles and treat crumb rubber with organic sulfur waste compounds has been a commonly employed technique (Chou et al, 2010). Other methods for improving the interfacial adhesion between rubber and the matrix in concrete include exposing the rubber particles to ultraviolet radiation to enhance their surface roughness characteristics (Alawais and West, 2019), pre-coating them with cement (Cairns et al, 2004), treating the rubber with sulfuric acid (H_2SO_4) (Hernández et al, 2017), and treating it with a Silane coupling agent (SCA)(Dong et al, 2013).

Several studies have shown promising results using different fillers. However, incorporating brick waste (BW) as a replacement for natural sand (NS) has shown potential for strengthening the paste. Nevertheless, determining the optimal brick waste and rubber waste contents that yield maximum mechanical strengths at a lower cost has received little attention in the literature (Sinkhondeet al., 2021). Previous studies have typically analyzed these waste products separately; incorporating brick waste into the elemental composition can help correct the compactness of the aggregate mixture (NS+RW).

The Response Surface Method (RSM) has recently gained popularity in many fields of civil engineering. It has been successfully applied in simulating material behavior, optimizing structural problems, experimentally estimating parameters, and determining optimal concrete mix proportions. The RSM provides an opportunity to achieve suitable values of flexural properties by performing experimental treatments and determining multiple and nonlinear relationships based on the data structures. Several models that relate the composition of the concrete mixture to its density and strength have been proposed using RSM, as demonstrated by (Nambiar and Ramamurthy, 2006). (Bektas and B.A. Bektas, 2014) employed the Box-Behnken design of experiments in conjunction with RSM to examine the effects of a combination of alkali-silica reaction on various concrete properties, including flexural strength, flexural modulus, and compression strength. Similarly, in (Mermerdaş et al, 2017), RSM was utilized to optimize a lightweight geopolymer mortar and analyze the impact of variables such as the binder content, curing time, and temperature on the compressive strength. (Boumaaza et al., 2020) studied the impact of reinforcing plaster mortars with natural fibers, examining varying percentages of NaOH and fiber lengths, using Response Surface Methodology (RSM) and the desirability function.

This paper aims to investigate the possibility of utilizing waste materials as fillers in composite mortar. The incorporation of waste materials presents a sustainable approach for waste reduction, while simultaneously enhancing the mechanical properties of construction materials.

To achieve this, an experimental investigation was carried out to assess the impact of incorporating crushed brick waste and waste tire rubber treated with sodium hydroxide as partial replacements for natural sand in mortar mixtures. The study evaluates various properties of the resulting mortars, including the flexural strength, dynamic elastic modulus, and displacement. Additionally, mathematical models were developed using response surface methodology (RSM) to predict these properties. The investigation also seeks to determine the most efficient ratio of additional components to recommend a cost-effective composite mortar mixture with an optimal composition.

The remaining sections of this work are structured as follows: the second section of the paper will provide a detailed description of the materials used in the study and the experimental program that was designed. This section will include information on the procedures and equipment used to perform the experiments. The third section will focus on the experimental results, the findings obtained from the study, and the model that was developed using RSM and the optimization process. Finally, the concluding section of the paper will summarize the main findings of the study and provide additional remarks on the results obtained.

2 EXPERIMENTAL WORK

2.1 Materials

The materials used for the mortar mixtures are described in detail below:

The mortars were prepared using high-quality and durable CPA CEM I 42.5 Portland type cement, which was supplied by the Ain Touta (GICA) cement industrial group located in Batna, Algeria. The cement used in this study adheres to the Algerian standard NA 442-2008 and has a density of 3.15 g/ cm^3 and a Blaine fineness of 3200 cm^2/g. Table 1 displays the chemical composition and main compounds of the cement employed in this research.

Tab. 1 *Chemical and mineralogical compositions of the Portland cement*

Chemical composition	(%)	Clinker mineralogical composition	(%)
SiO_2	21.62	C_3S	52.48
Al_2O_3	4.49	C_2S	22.69
Fe_2O_3	5.37	C_3A	2.82
CaO	63.91	C_4AF	16.32
MgO	1.66		
SO_3	1.92		
Na_2O	0.08		
K_2O	0.25		

For this research, the fine aggregate utilized was natural siliceous sand, with a maximum particle size of 4 mm. The sand was sourced from the Oum Ali deposit in the province of Tebassa, which is situated in northeastern Algeria. The physical properties of the aggregates required for the proportioning mix are presented in Table 2.

The rubber was obtained by mechanically grinding tire waste automobile and was supplied by a local factory in Batna, a city located in northeastern Algeria. It should be noted that fabric and steel belts were removed from the rubber by magnetic separation during the grinding process.

Tab. 2 *Characteristics of the sand used*

Characteristics	Value
Absolute density (g/cm^3)	2.56
Apparent density (g/cm^3)	1.54
Fineness modulus	2.36
Sand equivalent (%)	82
Water absorption (%)	2.66

The rubber tire particles used in this study were highly irregular and had dimensions ranging from 0.5-4 mm, with an absolute density of 0.94. To remove any impurities on the surface of the tire rubber, which could hinder the adherence of the matrix to the rubber when used as a fine aggregate in mortars, an alkaline pretreatment was carried out using a 10% NaOH saturated aqueous solution. This pretreatment was aimed at eliminating impurities such as dirt, oil, and passive layers. The distribution curves of the particle size for NS and RW were determined in accordance with the NF EN 933-2 standard and are depicted in Fig 1.

The brick waste materials utilized in this study were obtained locally from a brick manufacturing facility situated in the city of Benjdrah in the province of Guelma, which is located in the northern region of Algeria. The materials were eliminated during the production process for not meeting the required size or geometry after calcination at about 850°C and were treated as waste in the brick factory. The larger particles of the brick waste were manually crushed into different sizes and shapes.

After being ground to the required fineness, the crushed brick waste was sieved and passed through a 2 mm sieve. Following the typical classification outlined in the French Standard NF XP 18-540, 74% of the powders were able to pass through the 63 µm sieve. The uniform powder was then placed in a drying oven that was set at 105°C for 24 hours until it reached a constant weight; this resulted in an absolute density of 2.50 g/cm^3. Table 3 provides information on the chemical composition of the crushed brick waste.

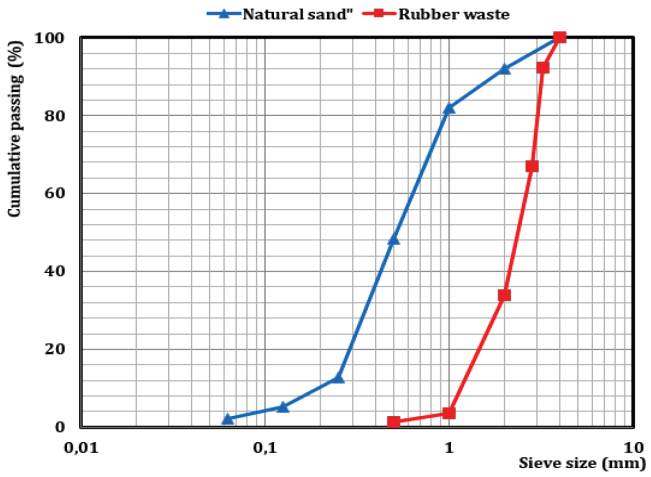

Fig. 1 *Degree of the particle size distribution curves of the and particles*

Tab. 3 *Chemical composition of the used (%)*

SiO_2	Al_2O_3	Fe_2O_3	CaO	MgO	K_2O	SO_3	Na_2O	LoI
69.26	14.17	6.30	4.28	2.25	1.34	0.02	0.28	1.96

Rubber mixes are typically treated with a superplasticizer to achieve the properties desired. In this study, superplasticizer was used at 1.4% of the weight of the cement for the reference mortar and adjusted according to each formulation. To prevent segregation when adding rubber aggregates to the mixture, a powder additive called MEDACOL BSE was added at 0.1% of the weight of the cement.

The addition of the stabilizer makes the mortar more plastic or viscous and has been proven to be very effective in stabilizing the rheological properties. Figs. 2-4 present the raw materials that were employed in the formulation of the mixtures.

2.2 Proportions of the mixture

In order to formulate a mortar composition, which could exhibit the required mechanical performance without any additional materials, a preliminary elemental composition has been proposed based on the mechanical criteria. The main aim of this research work is to find a reliable mixture with high compressive and tensile strength. To explore the impact of modifying the sand/cement ratio (S/C) on the compressive and flexural strength of cement mortars, numerous tests were conducted, while keeping a constant water/cement ratio (W/C) of 0.5. The S/C ratio was varied between 2.6 and 3.0, and it was concluded that the highest compressive and flexural strengths were attained at an S/C ratio of 2.8.

Fig. 2 *Natural sand*

Fig. 3 *Brick waste*

Fig. 4 *Rubber waste*

2.3 Experimental design

Three output responses were measured, i.e. the displacement, flexural strength, and dynamic elastic modulus. The variations of the input factors were considered at four levels for RW and five levels for BW, as shown in Table 4. The experimental study focused on a total of 20 batches of mortar mix, one of which was a control mix. The notation RWXBWY was used, where X is the percentage of rubber content and Y is the percentage of brick filler content.

Tab. 4 *Control parameters and variations of their levels*

Input Factor	Level 1	Level 2	Level 3	Level 4	Level 5
RW (%)	0	10	20	30	-
BW (%)	0	2.5	5	7.5	10

The quantity of superplasticizer was adjusted for the different compositions, based on a consistency index measured with a flow table test in accordance with NF EN 1015-6. The consistency index was set at 160 ± 20 mm, indicating that the mixtures were plastic. Its value was measured by the mean diameter of a sample of free mortar placed using a specific mold on the plate of a defined shaking table and subjected to a given number of vertical shakes by raising the shaking table and letting it fall freely from a given height.

The production of the rubberized mixtures followed the EN 196-1 standard by blending the dry components for 3 minutes, adding the superplasticizer, stabilizer, and 80% water, and then allowing it to blend for 2 more minutes. The remaining water was added and blended for another 2 minutes before resting it briefly to remove any mortar from the mixing container. The mixtures were then mixed for 2-3 minutes until achieving a consistent and homogeneous mix.

After the completion of the mixing steps, all the mixtures were poured into 40 x 40 x 160 mm^3 prismatic steel molds in two layers; each layer received at least 60 shocks each time the vibration table was applied to ensure uniform filling of the mould. To avoid the adhesion of the mortar and promote the evacuation of the cubes, the inner sides of the mould were previously lubricated prior to the moulding. Once the mould was filled, the excess fresh mortar was removed, and the specimen's surface was finished with a steel trowel to obtain a plane surface. After being cast, the mortar specimens were left for 24 hours in the moulds and were wrapped with plastic sheets to avoid any evaporation of the moisture or premature drying out. Twenty-four hours after placing the mortar in the moulds, the specimens were carefully removed and immediately transferred into water for curing. The curing process was conducted at a temperature of 20 ± 2°C and the laboratory's relative humidity until the time of testing.

2.4 Test procedures

2.4.1 Flexural strength

Three-point bending tests were performed to observe the flexural strength of the different mixtures using a standard hydraulic press with a capacity of 150KN (see Fig. 5). These tests were carried out at a loading speed of 50N/s± 10 until failure. The test was conducted according to standard EN 196-1 on prisms with a dimension of 40 × 40 × 160 mm. They cured for *28 days in water* and then dried in an oven until they achieved a constant mass before being tested.

Fig. 5 *The three-point bending lexural test on the 4 x 4 x 16 cm specimens*

The flexural strength values can be obtained from this relation:

$$R_f = \frac{1.5xFxL}{h^3} \quad (1)$$

Where: F, L, and h respectively represent the force recorded at the rupture, the distance between the supports was set equal to 100 mm, and the specimens height, respectively.

2.4.2 Displacement

To determine the displacement values at 28 days, a three-point bending test was conducted on specimens with a size of 40×40×160 mm. A transducer was placed in the center of the samples, and the distance between the lower supports was 100 mm. This allowed for the monitoring of the mid-span displacements and loads during the test. The samples were subjected to an ever-increasing tensile load, and the test was stopped once the post-peak curve was reached. The acquisition chain attached to the machine allowed for the simultaneous recording of the force and displacement throughout the test.

2.4.3 Dynamic modulus of elasticity

Ultrasonic measurements were carried out on specimens of dimensions 15 x 15 x 15 cm^3 (3 samples for each composition). After 28 days of curing, the cubes were weighed and tested for the dynamic modulus of elasticity according to NF EN 12504-4. This test consists of placing an emitter and a receiver on both ends of a specimen to generate longitudinal vibrations parallel to the principal axis, as shown in Fig. 6. The wave propagation time can be read in microseconds. The propagation speed or celerity C (m/sec) can be calculated using the following equation:

$$V = \frac{L}{T} \tag{2}$$

where V is the propagation speed of the ultrasonic waves in the mortar (m/sec); L is the distance between the emitter and receiver in m; and T is the propagation time in μsec.

Once the device is started, the wave propagation time can be read in a microsecond. The following equation gives the propagation speed or the celerity C (m/sec):

There is a correlation between the two parameters, and the following relationship (3) enables the estimation of the modulus of elasticity:

$$E_{dyn} = V^2 \rho \frac{(1+\vartheta)(1-2\vartheta)}{(1-\vartheta)} \tag{3}$$

E_{dyn} is the dynamic elastic modulus (MPa); ρ is the absolute volumetric mass of mortar (Kg/m^3); V is the wave propagation velocity (m/s); and υ is the dynamic Poisson's ratio of the mortar, which is equal to $\upsilon = 0.3$.

Fig. 6 *Measurement of the speed of the propagation of sound on the 15 × 15 × 15 cm specimens*

3 RESULTS AND DISCUSSION

According to a User Defined Design with two input factors, 20 experiments were carried out. The results obtained in terms of the output responses, such as the displacement (y), flexural strength (σ_f), and dynamic elastic modulus (E_{dyn}) are presented in Table 5.

3.1 The effect of the additives on the displacement

The experimental displacement data for the various reinforced cement mortars with different percentage additions (ranging from 0.0% to 10%) of the brick waste filler (BW) and (0% to 30%) of the tire rubber waste (RW) are depicted in Fig. 7a. It can be seen that the substitution of the mortar with brick waste (BW) up to a varying percentage of 10% leads to a decrease in the displacement, thereby indicating an elastic behavior. This decrease can be attributed to the enhanced toughness of the mortar due to the presence of the sand and brick filler. In contrast, the inclusion of rubber tire waste (RW) at percentages of 10%, 20%, and 30% in the mortar results in an enhanced elastic deformation capability during the flexural strength test, as indicated by an observed increase in the displacement. This is followed by a ductile failure, which highlights the improved flexibility and energy absorption capacity of the specimens. These findings suggest that the incorporation of rubber waste contributes to increased energy absorption and reduces the occurrence of cracks at failure in the specimens *(Shahrul et al, 2021).*

The mortars reinforced with RW30BW10 exhibited the highest displacement values, with a corresponding value of 0.565 mm, which signified a substantial increase of 101.78%. It was observed that an increase in RW content in the reinforced mortars resulted in higher deformations, indicating greater sample ductility. This was in contrast to the brittle behavior observed in the reference specimens and those substituted with brick waste (BW) up to a maximum percentage of 10%.

3.2 The effect of additives on the flexural strength

The mechanical properties of the rubberized mortar were evaluated from the the point of view of the flexural strength. The results presented in Fig. 7b shows a systematic drop in flexural strength with the increase in the rubber waste (RW) levels in the mortar, as proved by (Turki et al., 2009; Khalil et al., 2015; Grinys et al., 2012). The extreme values obtained by the experiment were 8.7, 6.1, 4.5, and 3.0 MPa for the RW-0BW0, RW10BW0, RW20BW0, and RW30BW0 compositions, respectively. This decrease in flexural strength can be attributed to several factors, such as the hydrophobic nature and non-polar character of rubber. These characteristics can increase the entrained air content, which in turn can lead to poor adhesion between rubber particles and the cement paste (RedaTaha et al, 2008). Additionally, the development of a weak interfacial transition zone (ITZ) can also result in the reduced stiffness and decreased load-bearing capacity of mortar, as a result of the lower stiffness of the rubber particles in comparison to fine aggregates (Najim and Hall, 2010). The weak ITZ can cause a concentration of internal stress, leading to

Tab. 5 *Experimental results according to the User Defined Design of the experiments*

Run	Input Factors				
	RW (%)	BW (%)	Displacement (mm)	Flexural strength (MPa)	Dynamic elastic modulus (GPa)
RW0BW0	0	0	0.281±0.07	8.7±0.19	19.91
RW10BW0	10	0	0.280±0.06	6.11±0.52	16.12
RW20BW0	20	0	0.437±0.07	4.54±0.47	11.36
RW30BW0	30	0	0.544±0.08	3.012±0.37	9.34
RW0BW2.5	0	2.5	0.28±0.05	7.72±1.47	18.29
RW0BW5.0	0	5	0.276±0.06	7.43±1.05	18.23
RW0BW7.5	0	7.5	0.273±0.09	7.51±0.46	18.48
RW0BW10	0	10	0.269±0.07	7.68±0.39	18.93
RW10BW2.5	10	2.5	0.305±0.05	6.9±0.43	16.46
RW10BW5.0	10	5	0.323±0.09	7.69±1.41	16.96
RW10BW7.5	10	7.5	0.323±0.06	8.22±0.32	17.62
RW10BW10	10	10	0.324±0.03	8.81±0.28	18.37
RW20BW2.5	20	2.5	0.439±0.09	5.18±0.11	11.95
RW20BW5.0	20	5	0.41±0.02	5.556±0.32	12.57
RW20BW7.5	20	7.5	0.426±0.05	6.17±0.36	13.07
RW20BW10	20	10	0.432±0.06	6.72±0.28	13.52
RW30BW2.5	30	2.5	0.516±0.04	3.43±0.16	9.8
RW30BW5	30	5	0.531±0.03	3.95±0.33	10.13
RW30BW7.5	30	7.5	0.546±0.07	4.49±0.35	10.46
RW30BW10	30	10	0.565±0.02	4.93±0.23	10.67

cracking and reduced mechanical performance. However, the study suggests that this effect can be mitigated through various treatments of the rubber particles before mixing, as suggested by (Li et al., 1998; Poon and Chan, 2006). Furthermore, the study found that the addition of brick waste (BW) filler can help increase the flexural strength of the rubberized mortar. The increment in flexural strength was found to be 29.88%, 48.27%, and 65.51%, respectively, compared to the RW0BW0 control mortar. This increase in strength can be attributed to the filling potential of the fine brick waste, which can help densify the structure and compensate for the negative effects of rubber waste on the mechanical properties of the mortar.

The test data presented in Fig. 7b indicated that the incorporation of an increased brick waste (BW) content of up to 5% as a partial replacement of sand had a negative effect on the flexural behavior of the eco-mortars studied at 30 days. However, a slight increase of above 5% without any symmetry was observed, with the highest flexural strength value found with 10.0% BW substituted with a maximum peak of 7.68 MPa. This suggests that the optimum level of BW incorporation may vary, depending on the specific mortar composition and application.

The study suggests that the reduced flexural strength of the rubber aggregates modified mortar can be attributed to the intrinsic properties of rubber, such as its low modulus of elasticity and high deformation capability. This makes it difficult to achieve a dense structure when incorporating rubber aggregates into the mortar, thereby leading to increased porosity and reduced adhesion between the rubber particles and the cement paste. However, incorporating BW filler may be beneficial as it can minimize the loss in strength by filling the voids and densifying the structure, which can be attributed to its filling capacity and pozzolanic potential *(*Poon and Chan, 2006).

Despite the improvement in flexural strength achieved by incorporating BW filler in all of the rates studied, the resistance of the reference mortars was not achieved. This suggests that further research is needed to optimize the incorporation of waste materials in mortar to achieve the desired mechanical properties.

3.3 The effect of additives on the dynamic elastic modulus

Fig 7c examined the evolution of the dynamic modulus of elasticity for three types of mortar, i.e., rubber waste mortar, brick waste mortar, and mixed mortar (RW-BW). The dynamic elastic modulus of the RW specimens was found to decrease as the percentage of rubber waste increased on the order of 16.12 GPa, 11.36 GPa, and 9.34 GPa for 10%, 20%, and 30% of RW, respectively (Fig. 7c). This decrease in the modulus can be attributed to the challenges associated with compacting mixtures containing a higher volume of rubber aggregates, which results in increased porosity, as mentioned in (Uygunoğlu and Topçu, 2010). The existence of air bubbles in the matrix exacerbates this phenomenon, as ultrasonic waves must navigate through these air bubbles to propagate through the cement paste. This results in an elongation of the ultrasonic wave's propagation time and a decrease in its propagation rate. The study found that the rubber-based composite has the ability to attenuate ultrasonic

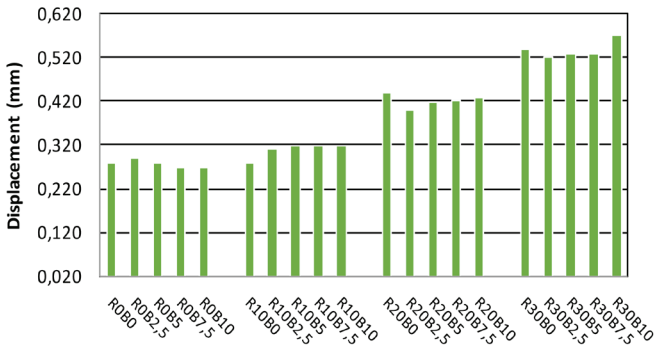

a) Displacement vs. RW % and BW %.

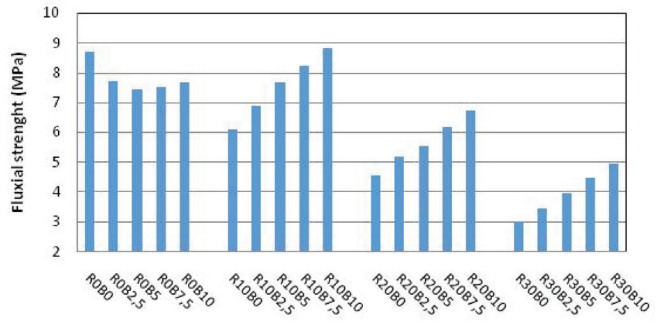

b) Flexural strength vs. RW % and BW %.

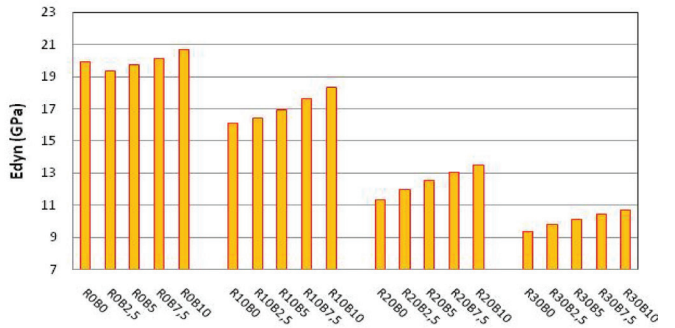

c) Elastic dynamic modulus vs. RW % and BW %.

Fig. 7 *a) Displacement, b) flexural strength, and c) elastic dynamic modulus vs. RW % and BW %*

waves and dampen vibrations, as observed in (Pedro et al, 2013).

The results showed that all the eco-mortars made had a slightly higher dynamic modulus than the eco-mortars with RW alone. The incorporation of brick fillers induced a slight increase in the rate of the dynamic modulus of elasticity with the different levels of the BW and RW studied. The study found that the E_{dyn} of the RW0BW7.5 and RW0BW10 mixtures exceeded that of the RW0BW0 mixture. The improvement in porosities due to the effect of the BW fillers may partly explain this increase. The increase in the dynamic modulus of elasticity observed in the mixed mortar (RW-BW) compared to the rubber waste mortar may be attributed to the filling potential of BW and the densification of the structure. The study suggests that incorporating brick waste filler can help compensate for the decrease in the dynamic elastic modulus caused by the addition of rubber waste.

3.4 Modeling of the experimental results using RSM

The RSM approach is a traditional modeling technique required to find a mathematical function between input variables and output results to explore the effect of these variables on the output responses, and, therefore, to optimize the responses obtained (Barua and Rao, 2010). The following equation provides the formulation of this mathematical function:

$$Y = a_0 + \sum_{i=1}^{n} a_i . x_i + \sum_{i=1}^{n} a_i b_j . x_i x_j + \sum_{i=1}^{n} b_i . x_i^2 \quad (4)$$

where the vector x_i represents the input parameters; n represents the number of these input parameters; and a_i, b_i, and $a_i b_j$ are coefficients that can be displayed.

3.4.1 Regression equations

The regression analysis technique is widely utilized to model the correlation between input variables and output results and is suitable for modeling and resolving an engineering problem. It helps to determine a good approximation for a suitable correlation (Myers and Montgomery, 2002). It is generally approximated by mathematical functions when models are attained by performing a set of organized experiments by utilizing an orthogonal array of experiments (Sahoo and Mishra, 2014). Based on the use of Design Expert V10 Software, the relationship between the inputs (rubber waste RX and brick waste RW) and output responses (displacement (y), the flexural strength (σ_f) and dynamic elastic modulus (E_{dyn}) are modeled by quadratic regression models and presented below by equations 5-7 with the R^2 coefficients of determination of (97.78%, 92.83%, and 95.86%), respectively.

$$Y = 0.036 + 0.014 * RW + 5.809x10^{-4} * BW + \\ + 5.929x10^{-4} * RW * BW + 4.286x10^{-3} * \\ *RW^2 + 3.678x10^{-4} * BW^2 \quad (5)$$

$$\sigma_f = 6.60 - 2.02 * RW + 0.74 * BW + 0.60 * \\ * RW * BW - 0.79 * RW^2 + 0.15 * BW^2 \quad (6)$$

$$E_{dyn} = 14.69 - 4.60 * RW + 0.63 * BW + 0.45 * \\ * RW * BW - 0.42 * RW^2 + 0.32 * BW^2 \quad (7)$$

3.4.2 Graphic validation of the models

Figures 8 to 10 depict the disparities between the experimental and predicted outcomes obtained from equations 5-7. These figures demonstrate that the experimental and estimated values are in close proximity to one another and that the pro-

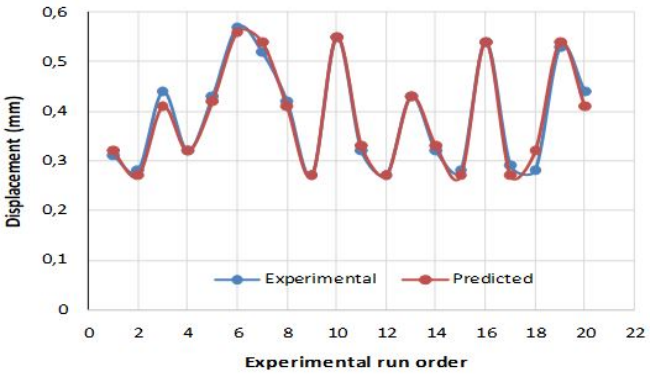

Fig. 8 *Predicted values of the displacement compared with the experimental values*

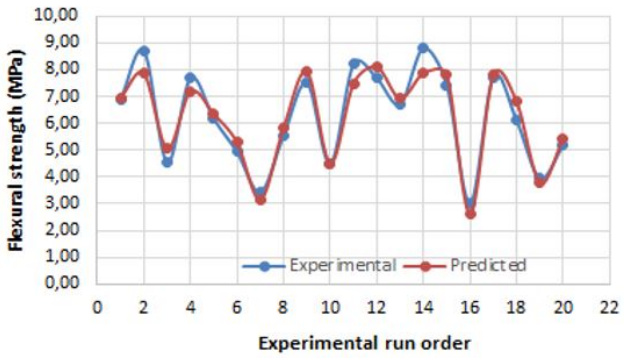

Fig. 9 *Predicted values of the flexural strength compared with the experimental values*

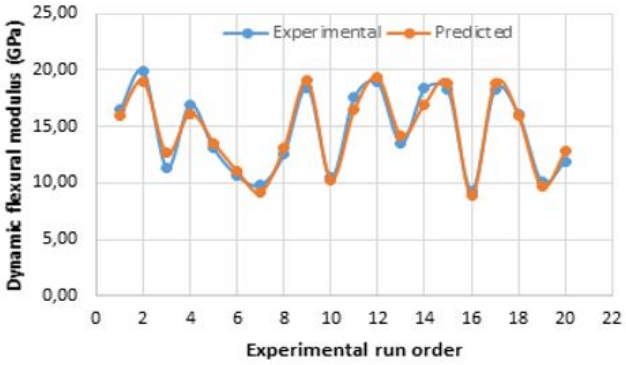

Fig. 10 *Predicted values of the dynamic flexural modulus compared with the experimental values*

posed quadratic models are capable of representing the problem under the experimental domain given.

3.4.3 Optimization of the responses

Multi-objective response optimization aims to compute the values of the input parameters that can be brought to the optimal values of the response outputs (Khellaf et al., 2017). The function desirability approach (FD) was introduced initially by (Derringer and Suich, 1980) and became widely utilized for both single and multi-objective optimization problems. The principle of this method lies in the transformation of the responses studied on its measurement scale into a unified scale of individual desirability (Bouzid et al., 2018). The variation interval of the desirability functions (*di*) is between zero (0.0) and one (1.0). The desirability function with the value 0.0 indicates an unacceptable response or that the response is outside the limits tolerated. A desirability value close to or equal one indicates that the response is considered acceptable (Sahoo and Mishra, 2014; Myers et al., 2016; Tebassi et al., 2017). The gradient algorithm utilized to calculate the desirability function is presented in detail (Lafifi et al., 2019).

The objective of the optimization procedure in this study was to determine the optimal values of the input factors (RW and BW) to maximize the displacement (*y*), flexural strength (σ_f), and dynamic elastic modulus (E_{dyn}). Table 6 provides a summary of the goals and the range of variations for all the optimization process parameters. The RW rate variation ranges from 0% to 30%, while the range of the BW rate is between 0% and 10%.

Tab. 6 *Goals and range variations of the optimization parameters*

Conditions	Goal	Lower Limit	Upper Limit
RW (%)	In range	0	30
BW (%)	In range	0	10
Displacement (**y**) (mm)	Maximize	0.269	0.565
E_{dyn} (MPa)	Maximize	3.012	8.81
σ_f (GPa)	Maximize	9.34	19.91

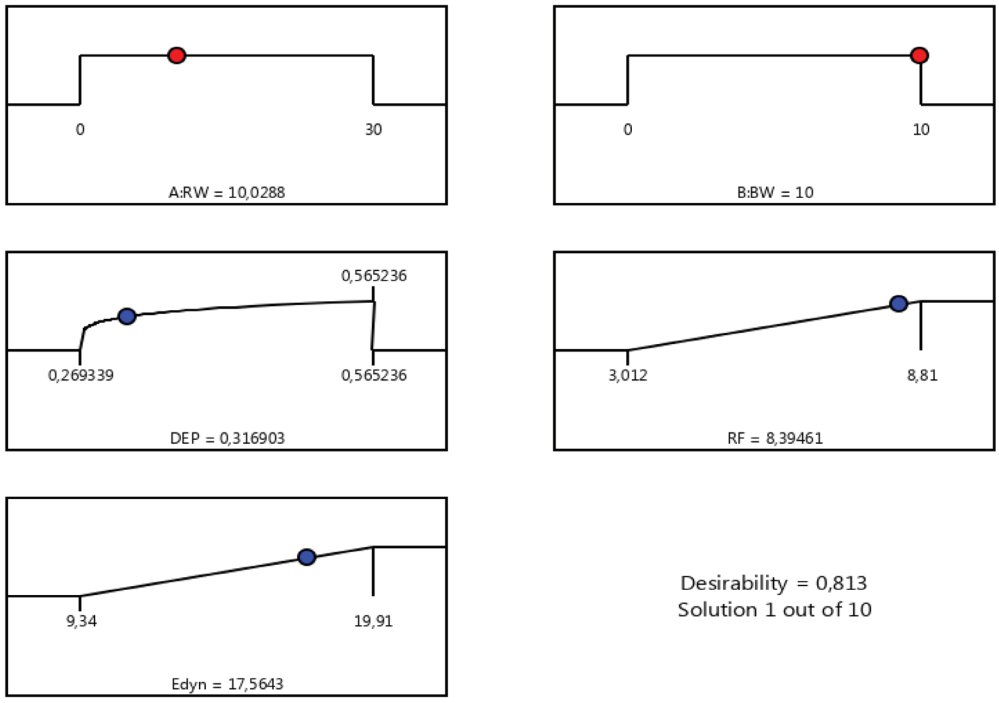

Fig. 11 *Optimization results using desirability function*

Tab. 7 *Results of the optimization process*

Number	**RW** (%)	**BW** (%)	Displacement (***y***) (mm)	σ_f (MPa)	$\mathbf{E_{dyn}}$(GPa)	Desirability	
1	10.029	10.00	0.317	8.395	17.564	0.813	Selected
2	10.250	10.00	0.319	8.389	17.512	0.812	
3	9.827	10.00	0.315	8.399	17.611	0.812	
4	9.002	10.00	0.307	8.409	17.797	0.811	
5	13.715	10.00	0.360	8.199	16.613	0.794	

The optimization results are presented in Fig. 11 and in Table 7, where the optimal values of the two input factors were found to be RW = 10.102% and BW = 10.00%. The optimized responses were: the displacement (y) = 0.317 mm, the flexural strength (σ_f) = 8.395 MPa, and the dynamic elastic modulus (E_{dyn}) = 17.564 GPa.These predicted results are very similar to those obtained using the experiments (for the experiment results: displacement (y) = 0.324 mm, the flexural strength (σ_f) = 8.81 MPa, and the dynamic elastic modulus (E_{dyn}) = 18.37 GPa).

The percentage errors between the experiments and results predicted were: 1.85% for the displacement (y), -4.73% for the flexural strength (σ_f), and -4.48% for the dynamic elastic modulus (E_{dyn}). Based on these results, it can be concluded that the predicted results are in good agreement with the experimental results and that confirmatory tests may therefore not be necessary.

4 CONCLUSIONS

The study aimed to investigate the effects of adding rubber tire waste and crushed brick fillers on the mechanical properties of composite mortar. To achieve this, a series of experiments was conducted using a user-defined orthogonal array, which allowed for the testing of different combinations of input factors systematically.

The response surface methodology was employed to model and predict the output responses, which included the displacement, flexural strength, and dynamic elastic modulus. The desirability function was also used to optimize the responses and determine the optimal input factors.

According to our study, 5% of the BW filler is the optimal percentage when utilized alone; however, 10% is optimal when combined with RW. The dynamic modulus of elasticity slightly increased with an increase in the rate of brick waste filler. The use of brick waste filler can enhance flexural strength, while compensating for losses caused by introducing rubber waste. For an average rate of 20% rubber waste, the flexural strength gains recorded at 30 days were 14.09%, 22.47%, 35.90%, and 48.02%, respectively, with an increase in the brick filler content from 2.5% to 10% compared to the mortar with 20% rubber waste and no brick filler.

The study also found that combining rubber tire waste and crushed brick filler can result in slight enhancements in other properties such as the dynamic modulus of elasticity and displacement. For instance, compared to mortar with 20% rubber waste alone, the dynamic modulus of elasticity increased by 5.19%, 10.65%, 15.05%, and 19.01%, respectively, for mortars with rubber waste and 2.5%, 5%, 7.5%, and 10% brick filler.

The RSM proved its capability as a regression method for modeling and predicting the experiment's results. The optimal values of tire rubber waste and crushed brick filler for maximizing the displacement, flexural strength, and dynamic elastic modulus were found to be 10.102% and 10.00%, respectively.

In conclusion, this study has important implications for the construction industry as it investigates the possibility of using waste materials as fillers in composite mortar. The inclusion of waste materials offers a sustainable solution for reducing waste and simultaneously improving the mechanical properties of construction materials as confirmed experimentally in the work.

Conflict of Interest

The authors declare no conflicts of interest regarding this manuscript, and there is no significant financial support for this work that could have influenced its outcome.

REFERENCES

Alawais, A – West, R.P. (2019) *Ultra-violet and chemical treatment of crumb rubber aggregate in a sustainable concrete mix.* J. Struct. Integr. Maint. 4 144-152.

Batayneh, M.K., - Marie, I., - Asi, I. (2008) *Promoting the use of rubber concrete in developing countries*, Wast. Manag. 28; 2171-2176.

Barua, M.K. – Rao, J.S. (2010) *Measurement surface roughness through RSM: effect of coated carbide tool on 6061-t4 aluminum.* Inter. J. Enterp. Net. Manag. (IJENM). 4; 136-153.

Bektas, F. – Bektas, B.A. (2014) *Analyzing mix parameters in ASR concrete using response surface methodology.* Constr. Build. Mater. 66; 299-305.

Boumaaza, M. – Belaadi, A. – Bourchak, M. (2020) *The Effect of Alkaline Treatment on Mechanical Performance of Natural Fibers-reinforced Plaster: Optimization Using RSM.* Journal of Natural Fibers 1-21.

Bouzid, L. – Berkani, S. – Yallese, M.A. – Girardin, F. – Mabrouki, T. (2018) *Estimation and optimization of flank wear and tool lifespan in finish turning of AISI 304 stainless steel using desirability function approach*. Int. J. Ind. Eng. Comput. 9; 349-368.

Buši´c, R. – Mili˘cevi´c, I. – Šipoš, T.K. – Strukar, K. (2018) *Recycled rubber as an aggregate replacement in self-compacting concrete-literature overview.* Materials. 11; 1-25.

Cairns, R. – Kew, H. – Kenny, M. (2004) *The use of recycled rubber tyres in concrete construction.* Final report.The Onyx Environmental Trust, University of Strathclyde, Glasgow.

Chou, L. – Lin, C. – Lu, C. – Lee, C. – Lee, M. (2010) *Improving rubber concrete by waste organic sulfur compounds.* Wast. Manag. Res. 28; 29-35.

Derringer, G. – Suich, R. (1980) *Simultaneous optimization of several response variables*. J. Qual Techn. 12; 214-219.

Dong, Q. – Huang, B. – Shu, X. (2013) *Rubber modified concrete improved by chemically active coating and silane coupling agent.* Constr. Build. Mater. 48; 116-123.

Grinys, A. – Sivilevic˘ius, H. – Dauksˇys, M. (2012) *Type rubber additive effect on concrete mixture strength. J.* Civ. Eng. Manag. 18; 393-401.

Guo, S. – Dai, Q. – Si, R. – Sun, X. – Lu, C. (2017) *Evaluation of properties and performance of rubber-modified concrete for recycling of waste scrap tire.* J. Clean. Prod. 148; 681-689.

Hernández, E.H. – JGámez, .F.H. – Cepeda, L.F. – Muñoz, E.J.C. – Corral, F.S. – Rosales, S.G.S. (2017) *Sulfuric acid treatment of ground tire rubber and its effect on the mechanical and thermal properties of polypropylene composites*. J. Appl. Polym. Sci. 134; 1-7.

Hidalgo, C.A. – Bustamante-Hernández, J.J. (2020) *A new sustainable geotechnical reinforcement system from old tires: experimental evaluation by pullout tests*. Sustainability. 12; 1-18.

Khalil, E. – Abd-elmohsen, M. – Anwar, A.M. (2015) *Impact resistance of rubberized self-compacting concrete*. Water. Sci. 29; 45-53.

Khellaf, A. – Aouici, H. – Smaiah, S. – Boutabba, S. – Yallese, M.A. – Elbah, M. (2017) *Comparative assessment of two ceramic cutting tools on surface roughness in hard turning of AISI H11 steel: including 2D and 3D surface topography*. Int. J. Adv. Manuf.Techn.89; 333-354.

Khuri, A.I – Mukhopadhyay, S. (2010) *Response surface methodology*. WIREs. Comput. Stat. 2; 128-149.

Lafifi, B. – Rouaiguia, A. – Boumazza, N. (2019) *Optimization of geotechnical parameters using Taguchi's design of experiment (DOE), RSM and desirability function*. Innov. Infrastruct Solut. 35; 1-14.

Li, Z. – Li, F. – Li, J.S.L. (1998) *Properties of concrete incorporating rubber tyre particles*. Mag. Conc. Res. 50; 297-304.

Lo, D. – Presti, (2013) *Recycled tyre rubber modified bitumens for road asphalt mixtures: A literature review.* Constr. Build. Mater. 49; 863-881.

Ma, Q.W. – Yue, J.C. (2013) *Effect on mechanical properties of rubberized concrete due to pretreatment of waste tire rubber with NaOH*. Appl. Mech. Mater. 357-360; 897-904.

Mahla, R. – Mahla, R.P. (2015) *Partial replacement of coarse aggregate by waste tires in cement concrete*. Int. J. Tech. Res. (IJTR).4; 95-98.

Mermerdaş, K. – Algın, Z. – Oleiwi, S.M. – Nassani, D.E. (2017) *Optimization of lightweight GGBFS and FA geopolymer mortars by response surface method*. Const. Build. Mater. 139; 159-171.

Miller, N.M. – Tehrani, F.M. (2017) *Mechanical properties of rubberized lightweight aggregate concrete*. Constr. Build. Mater. 147; 264-271.

Mohajerania, A. – Burnetta, L. – Smitha, J.V. – Markovskia, S. – Rodwella, G. – Rahmana, M.T. – Kurmusa, H. – Mirzababaeib, M. – Arulrajahc, A. – Horpibulsukd, S. – Maghoolc, F. (2020) *Recycling waste rubber tyres in construction materials and associated environmental considerations: A review*. Res. Cons. Recy.155; 1-17.

Myers, R.H. – Montgomery, D.C. (2002) *Response surface methodology: process and product optimization using designed experiments*. 2nd ed. John Wiley and Sons, Inc, New York.

Myers, R.H. – Montgomery, D.C. – AndersonCook, C.M. (2016) *Response surface methodology: process and product optimization using designed experiments*. Wiley, New York.

Najim, K.B. – Hall, M.R. (2010) *A review of the fresh/hardened properties and applications for plain- (PRC) and self compacting rubberised concrete (SCRC).* Constr. Build. Mater. 24 2043-2051.

Nambiar, E.K. – Ramamurthy, K. (2006) *Models relating mixture composition to the density and strength of foam concrete using response surface methodology*. Cem.Concr. Comp. 28; 752-760.

Onuaguluchi, O. – Panesar, D.K. (2014) *Hardened properties of concrete mixtures containing pre-coated crumb rubber and silica fume*. J. Clean. Prod. 82; 125-131.

Pedro, D. – De Brito, J. – Veiga, R. (2013) *Mortars made with fine granulates from shredded tires.* J. Mater. Civ. Eng. ASCE.25; 519-529.

Pelisser, F. – Zavarise, N. – Longo, T.A. – Bernardin, A.M. (2011) *Concrete made with recycled tire rubber: effect of alkaline activation and silica fume addition*. J. Clean. Prod. 19; 757-763.

Poon, C.S. – Chan, D. (2006) *Paving blocks made with recycled concrete aggregate and crushed clay brick*. Const. Build. Mater. 20; 569-577.

RedaTaha, M.M. – El-Dieb, A.S. – AbdEl-Wahab, M.A. – Abdel-Hameed, M.E. (2008) *Mechanical, fracture and microstructural investigations of rubber concrete*. J. Mater. Civ. Eng. (ASCE). 20; 640-649.

Rokade, S. (2012) *Use of waste plastic and waste rubber tyres in flexible highway pavements*. International Conference on Future Environment and Energy IPCBEE, p.105-108.

Sahoo, A.K. – Mishra, P.C. (2014) *A response surface methodology and desirability approach for predictive modeling and optimization of cutting temperature in machining hardened steel.* Inter. J. Indus. Eng. Comp. 5; 407-416.

Serdar, M. – Baričević, A. – Bjegović, D. – Lakušić, S. (2014) *Possibilities of use of products from waste tyre recycling in concrete industry*. J. Appl. Eng. Sci. 12; 89-93.

Shahrul, S. – Mohammed, B.S. – Wahab, M.M.A. – Liew, M.S. (2021) *Mechanical Properties of Crumb Rubber Mortar Containing Nano-Silica Using Response Surface Methodology*. Materials.14; 54-69.

Shu, X. – Huang, B. (2014) *Recycling of waste tire rubber in asphalt and Portland cement concrete: An overview*. Constr. Build. Mater. 67; 217-224.

Si, R. – Guo, S. – Dai, Q. (2017) *Durability performance of rubberized mortar and concrete with NaOH-Solution treated rubber particles*. Constr. Build .Mater. 153; 496-505.

Sinkhonde, D. – Onchiri, R.O. – Oyawa, W.O. – Mwero, J.N. (2021) *Response surface methodology-based optimisation of cost and compressive strength of rubberised concrete incorporating burnt clay brick powder*. Heliyon. 7; e085654.

Sofi, A. (2018) *Effect of waste tyre rubber on mechanical and durability properties of concrete: A review*. Ain Shams Eng. J. 9; 2691–2700.

Sukontasukkul, P. – Tiamlom, K. (2012) *Expansion under water and drying shrinkage of rubberized concrete mixed with crumb rubber with different size*. Constr. Build. Mater. 29; 520-526.

Strukar, k. – Šipoš, T.K. – Miličević, I. – Bušić, R. (2019) *Potential use of rubber as aggregate in structural reinforced concrete element: A review*. Eng Stru.188; 452-468.

Tebassi, H. – Yallese, M.A. – Belhadi, S. – Girardin, F. – Mabrouki, T. (2017) *Qualityproductivity decision making when turning of Inconel 718 aerospace alloy: a response surface methodology approach*. Int. J. Ind. Eng. Comput. 8; 347-362.

Thomas, B.S. – Gupta, R.C. (2016) *A comprehensive review of the applications of waste tire rubber in cement concrete*. Renew. Sust. Energ. Revi. 54; 1323-1333.

Turki,M. – Bretagne, E. – Rouis, M.J. – Queneudec M. (2009) *Microstructure, physical and mechanical properties of mortar–rubber aggregates mixtures*. Const. Build. Mater. 23; 2715-2722.

Uygunog˘lu, T. – Topçu, I.B. (2010) *The role of scrap rubber particles on the drying shrinkage and mechanical properties of self-consolidating mortars*. Constr. Build. Mater. 24; 1141-1150.

Valente, M. – Sibai, A. (2019) *Rubber/crete: Mechanical properties of scrap to reuse tire-derived rubber in concrete; A review*. *J. Appl*. Biomater. *Funct*. *Mater.*7; 1-8.

Zhang, B. – Poon, C.S. (2018) *Sound insulation properties of rubberized lightweight aggregate concrete*. J. Clean. Prod. 172; 3176-3185.

sciendo

Slovak Journal of Civil Engineering

Vol. 32, 2024, No. 2, 38 – 47
DOI: 10.2478/sjce-2024-0012

CONSTRUCTION MANAGEMENT BY CONTROLLING THE DESIGN AND CURING TIME OF A CONCRETE MIX

Hamid Reza DARVISHVAND[1], Seiyed Ali Haj Seiyed TAGHIA[2*], Navid AFSHARI[3]

Abstract

The interval of time after pouring concrete is an important factor, which directly affects the timing and cost of construction. The case study that was investigated in this research, is a tunnel project located in Iran. Eighteen mix designs were prepared using properties such as different water-cement ratios and the use of two types of superplasticizer with different dosages. The optimal mix designs among the samples were separately specified.

Concrete mix designs with different curing ages were made to specify the minimum curing time in which the concrete could gain the required compressive strength. Moreover, the concrete's compressive strength was measured for different ages in order to determine the minimum time interval. For a better insight, two mathematical equations were derived to estimate the minimum curing time and time interval. Finally, a statistical analysis was conducted in order to determine the proper time intervals. Moreover, the analysis specified the impact rate of the research parameters (i.e. the type and dosage of superplasticizer, curing time, and water-cement ratio) on the compressive strength

Address

[1] Dept. of Civil Engineering, Qazvin Branch, Islamic Azad University, Qazvin, Iran, (hr.darvishvand@qiau.ac.ir), ORCID number: 0000-0003-2042-2043.

[2] Dept. of Civil and Environmental Engineering, University of Hawaii at Manoa, Honolulu, USA, (taghia@hawaii.edu), ORCID number: 0000-0002-9304-7427.

[3] Dept. of Civil Engineering, Qazvin Branch, Islamic Azad University, Qazvin, Iran, navidafshari1@gmail.com

* ***Corresponding author:*** taghia@hawaii.edu

Key words

- Time interval;
- Mix design;
- Water-cement ratio;
- Superplasticizer;
- Compressive strength;
- Statistical analysis.

1 INTRODUCTION

Reducing the time and cost of construction projects is one of the main goals of each on-going project. One of the causes that prolong the construction of concrete structures is the time interval for the curing process in order to gain adequate concrete strength. The curing of concrete is crucial regarding its strength and durability characteristics (Felekoglu et al. 2014; Hui et al. 2014; Wu et al. 2012; Yildirim et al. 2015; Zhu et al. 2014). The curing process includes the moisture-curing and curing temperatures (Yu et al. 2015; El-Ashkar et al. 2007).

Kim et al. (1998) studied a change in strength regarding the effect of the curing time at specific temperatures. The results indicated that concrete under a high temperature at an early stage gains higher early-age strength, but actually gains a lower later-age strength. Concrete under a low temperature at an early age shows lower early-age strength, but nearly the same later-age strength. They suggested a model for concrete to gain strength.

Elmoaty et al. (2016) investigated the effects of the curing time and temperature on geopolymer concrete. The results indicated that concrete properties are notably affected by curing conditions.

Haghighatnejada et al. (2016) examined the properties of concrete made with a substitution of natural sand with recycled aggregate subjected to different curing conditions. The results revealed that an irregular curing condition often decreases concrete characteristics, whereas regular water curing provides appropriate curing conditions and improves concrete properties.

Zhu et al. (2016) studied the effect of the curing time on the mechanical properties of engineered cementitious composites (ECCs). The compressive and flexural strengths rise, as the curing time increases. Suitable mechanical properties are gained for cement substituted by 80% fly ash and a water curing time of 7 days.

Da et al. (2017) studied the mechanical behavior of concrete at different curing days (3, 7, 14 and 28 days) subjected to different confining stresses. The curing time lowers with an increase in confinement. They proposed a curing time model.

Madandoust et al. (2019) evaluated the effect of steel and polypropylene fibres on lightweight concrete properties. The specimens were cured subject to different curing conditions. The results showed that the mix designs cured under a 90°C vapour curing reach the highest mechanical strength.

Fang et al. (2020) examined the effect of the curing time (7, 28, 90 and 180 days) on flexural and compressive strengths. Regular curing after 28 days can notably enhance the mechanical properties of concrete with alkali contents of 2–3%.

Formworks should be removed when the concrete is able to bear effective stresses and deformations within a given tolerance. According to the ACI 318-19 standard, no construction loads should be placed on nor should any formwork removed from any part of a structure under construction except when that portion of the structure in combination with the remaining formwork has sufficient strength to safely support its weight and the loads placed thereon and without impairing serviceability.

With reference to these issues, a case study called the Manjil tunnel project was investigated in this article. The main purpose of this research is to adjust concrete curing time and the time intervals to continue concrete work so that a structure can be able to withstand all load types.

1.1 Case Study: Manjil Tunnel Project (Qazvin-Rasht Highway)

The project site is located between the cities of Manjil and Rudbar in the Gilan province of Iran. The 7 km long-project site consists of two separate runways, 5 tunnels, two valley bridges, one ramp bridge (Zeytoun Bridge) and a 4 km-open trench, which commenced in 2015 and was completed in March 2017. This project had a direct impact on reducing traveling and transport times. Therefore, it was of the essence to promptly complete this job. In this project, the conventional and new generations of superplasticizer (SP) that are available on the Iranian market were used to facilitate the concrete works. The other purpose of this research was to separately clarify the optimal mix designs among samples containing both types of SPs. In the following section, the role of SPs utilized in the concrete production of this project is discussed.

1.2 Superplasticizer (SP)

SPs are broadly used to produce workable, strong, and durable mortars and concrete. The hydration role of cement in the presence of an SP has been studied by many researchers. SPs can disperse cement particles and improve the workability, compactness, permeability and carbon resistance of concrete (Yamda et al. 2000; Carazeanu et al. 2002; Kreppelt et al. 2002; Yu et al. 2013; Chen et al. 2016). Two types of SPs are available on the Iranian market and are discussed in this research:

1. Conventional SPs based on polynaphthalene-sulfonate (PNS), melamine (PMS) or lignosulfonate (LS) disperse particles by means of electro sterics.
2. A new generation of SPs such as polycarboxylate-ether (PCEs) disperse particles by forming a steric obstacle.

1.3 Polynaphthalene Sulfonate (PNS)

The PNS is a polymeric molecule formed by the condensation of naphthalene sulfonic acid and formaldehyde in which the hydrophilic groups are mainly sulfonic groups, whereas the hydrophobic part is naphthalene. A PNS can reduce water consumption by up to 20% (Uchikawa et al. 1992).

1.4 Polycarboxylate-Ether (PCE)

The effects of PCE in order to reduce water consumption and raise the workability of concrete have been investigated by many researchers (Mollah et al. 2000; Yamada et al. 2000; Golaszewski and Szwabowski 2004; Puertas et al. 2005; Palacios et al. 2009; Ferrari et al. 2010; Toledano-Prados et al. 2013; Adjoudj et al. 2014; Lange et al. 2014; Li et al. 2014; Cartuxo et al. 2015). In addition, it has been proved that PCE can reduce the plastic shrinkage of concrete (Baghabra et al. 2014). (Zhang and Kong (2014)) and (Perrot et al. (2013)) investigated the role of PCE on the porosity of concrete and understood that SP apparently decreases permeability and increases the compressibility of hardened concrete.

1.5 Significance of Research

Most of the aspects and novelties of the current study can be addressed as follows:

- Determining the optimal mix design regarding two generations of superplasticizer
- Specifying the minimum curing time to meet the required compressive strength
- Estimating the minimum time interval for concrete at different ages
- Deriving mathematical equations to capture the findings of the research
- Conducting parametric studies on the roles of research parameters

2 EXPERIMENTAL PROCEDURE

In this section, the material types, mix design, and sample preparation are separately described.

2.1 Material types

Ordinary Portland cement was used for all the specimens. The class of this cement is 42.5, indicating that it should

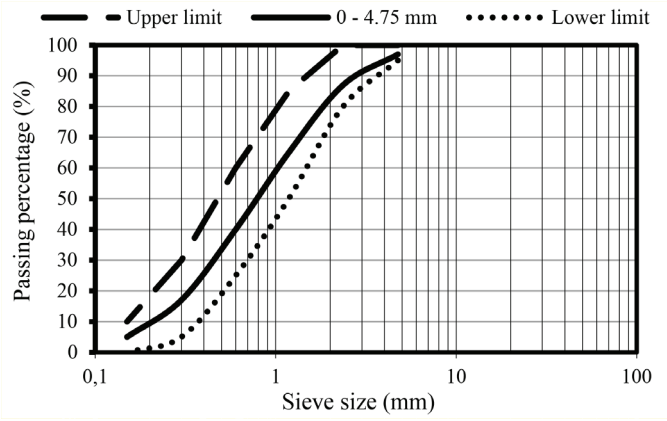

Fig. 1 *Sieve analysis and grading curve and its limits for sand*

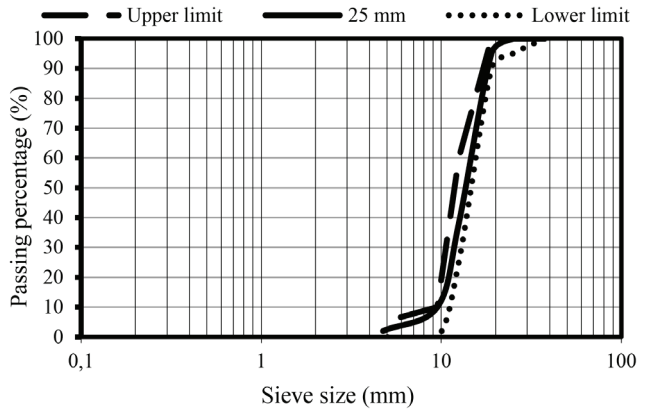

Fig. 2 *Sieve analysis and grading curve and its limits for gravel*

achieve a minimum compressive strength of 42.5 MPa at 28 days. The specimens were made according to ASTM C150 (2004) and the gravel and sand aggregates consisted of river types (available construction materials at the project site) in accordance with ASTM C33 (2003). The sand grain sizes ranged from 0 to 4.75 mm with an apparent weight of 2700 kg/m^3 in the saturated surface dry (SSD) state. A sieve analysis, the grading curves, and their limits for sand and gravel are provided in Figs. 1 and 2, respectively. ASTM C33 (2003) was applied to evaluate the analysis and grading. The lower and upper limits of this standard are specified in these figures.

Data from the figures suggest that all the aggregates satisfy the grading requirement because they fall within the allowable limits of ASTM C33 (2003). Therefore, they are appropriate for the production of concrete. As mentioned above, two types of SPs based on PNS and PCE have been used. The technical specifications for the SPs are given in Table 1.

Tab. 1 *The specifications of SPs*

Properties	PNS	PCE
Ingredient	Polynaphthalene sulfonate	Polycarboxylate
Color	Dark green	Dark brown
State	Liquid	Liquid
Density g/ml (20˚C)	1.2 ± 0.02	1.1 ± 0.02
PH (20˚C)	8	7
Total chloride (%)	<0.1	<0.1
Ionic nature	Anion	Anion

Tab. 2 *Mix design characteristics*

Code	Cement (kg/m^3)	Sand (kg/m^3)	Gravel (kg/m^3)	Water-cement ratio	SP (%)	
					PCE	PNS
W4P2	400	910	1080	0.4	0.2	-
W4P4	400	910	1080	0.4	0.4	-
W4P6	400	910	1080	0.4	0.6	-
W5P2	400	910	1080	0.5	0.2	-
W5P4	400	910	1080	0.5	0.4	-
W5P6	400	910	1080	0.5	0.6	-
W6P2	400	910	1080	0.6	0.2	-
W6P4	400	910	1080	0.6	0.4	-
W6P6	400	910	1080	0.6	0.6	-
W4N2	400	910	1080	0.4	-	0.2
W4N4	400	910	1080	0.4	-	0.4
W4N6	400	910	1080	0.4	-	0.6
W5N2	400	910	1080	0.5	-	0.2
W5N4	400	910	1080	0.5	-	0.4
W5N6	400	910	1080	0.5	-	0.6
W6N2	400	910	1080	0.6	-	0.2
W6N4	400	910	1080	0.6	-	0.4
W6N6	400	910	1080	0.6	-	0.6

2.2 Mix design

In this study, eighteen mix designs, which are summarized in Table 2, were prepared. The sequence of mixing the materials was as follows: First, the mixture of sand and gravel was mixed with three-fourths of the required water for 15 minutes. Then, cement was added to the mixture, and lastly, one-fourth of the remaining water, which was previously mixed with the superplasticizer, was gradually added to the mixture. Each mix design includes three samples. Tab. 2 provides the abbreviations for all the specimens.

In the nomenclature of the mixing design, numbers 4, 5, and 6 following the letter W indicate the water-cement ratios (W/C ratios) of 0.4, 0.5, and 0.6, respectively. Th1e letters P and N represent the polycarboxylate-ether and polynaphthalene sulfonate (the SPs), respectively. Also, the numbers 2, 4, and 6 after P and N show the SP dosage as a fraction of the cement's weight (equal to 0.2, 0.4, and 0.6 percent, respectively). Generally, SPs are used to compensate for a low W/C ratio and increase the workability of concrete. However, in this study, a higher W/C ratio of 0.6 was studied to simulate the operational faults during concrete production.

2.3 Preparation of the Sample

The concrete was initially prepared and followed by inserting it into the pre-prepared molds. The samples were then set to harden. The shape of a cubic mold was used with each 15 cm dimension (Fig 3). After 24 hours, the molds were removed, and the samples were cured for a duration of 1, 3, 7, 14, and 28 days. The curing time for concrete highly depends on the weather conditions and varies at different project sites. The ambient conditions in this field study were a temperature of 17°C, humidity of 65%, and a wind speed of 20 . In order to simulate the curing conditions of the samples with the real situations at the site, the curing process was performed in open air by covering them with gunny sacks together with watering them daily.

Fig. 3 *Preparing the samples on site*

3 RESULTS AND DISCUSSION

This research was conducted in two steps:

1: Dealing with the effect of the curing time on the concrete's compressive strength at the age of 28 days. Also, the optimal mix designs were determined. Afterwards, the concrete's strength was studied at different ages (1, 3, 7, 14, and 28 days). In this way, for a quantification of the results, two mathematical equations have been proposed.
2: Conducting the statistical analysis to reach a comprehensive conclusion on this research.

3.1 The effect of the curing time on the concrete's compressive strength at the age of 28 days

The compressive strength of the cubic samples cured at different ages of 1, 3, 7, 14, and 28 days are provided in Table 3.

The compressive strength tests were performed at the age of 28 days according to ASTM C39 (2014). As presented in Table 2, samples W4P4 (W/C ratio= 0.4 and PCE=0.4%) and W5N6 (W/C ratio= 0.5 and PNS= 0.6%) resulted in the highest level of compressive strength. These samples are defined as the optimal mix designs with two different types of SPs.

In Figures 4 to 9, the compressive strength of the 28-day concrete is depicted for different W/C ratios and various SP percentages (obtained from Table 3). The increasing rates of the compressive strength are plotted with reference to the corresponding samples with a one-day curing time. The data presented in these figures were extracted from Table 3. As expected, Figs. 4 to 9 show an increase in the 28-day compressive strength due to the increase in the curing time. However, its growth rate declines by increasing the curing time. In other words, the required strength in the concrete can be gained be-

Tab. 3 *Compressive strength of the samples for different curing periods at the age of 28 days (MPa)*

No.	Mix design code	Period of curing (days)				
		1	3	7	14	28
1	W4P2	24.1	25.6	26.2	28	30
2	W4P4	28.9	31.2	32.5	33.2	34
3	W4P6	26.1	28	28.9	29.7	32
4	W5P2	23.4	24.8	25.8	27.4	29
5	W5P4	27.2	29.5	30	31	32.5
6	W5P6	24.2	25.8	26.2	27.5	30
7	W6P2	21.7	22.9	24.4	25.2	27
8	W6P4	21.8	22.2	24	26	29.5
9	W6P6	18.2	19.1	20.4	21.5	26
10	W4N2	21	22.5	23.1	24.5	27
11	W4N4	22.9	24.4	25.8	26.9	29
12	W4N6	24.6	26.1	27.5	28.4	30.5
13	W5N2	23	24.8	25.6	26.4	28.5
14	W5N4	25.5	27.4	28.3	29.2	31
15	W5N6	26.8	28.8	29.7	30.8	31.8
16	W6N2	21.2	22.5	23.6	24	26.5
17	W6N4	23.4	25	25.9	26.5	28
18	W6N6	21	24.3	26.2	27.1	29.5

fore the age of 28 days, without any significant reduction in the characteristic strength.

In order to quantify the effect of the curing time on the 28-day concrete's strength, the following equation is proposed for the two optimal mix designs of W4P4 and W5N6 by adding the curve fitting of the data provided in Table 3:

$$C = 0.044 \ln (d_r) + 1 \quad (1)$$

C is the reduction coefficient of the 28-day strength of the concrete, and d_r are the normalized curing days (the number of curing days divided by 28 days as related to the full curing time). The diagram of Eq. (1) is shown in Fig. 10 along with the data for the W4P4 and W5N6 optimal mix designs.

The graph shows good agreement between Eq. 1 and the experimental results (correlation coefficient: R^2 is 0.99). As shown in Fig. 10, the concrete reaches 90% of its characteristic strength in d_r=0.1, which is equivalent to 0.1*28 days ≈ 3 days. Therefore, 3 days of curing is appropriate for time management of the project and achieving the required strength at 28 days.

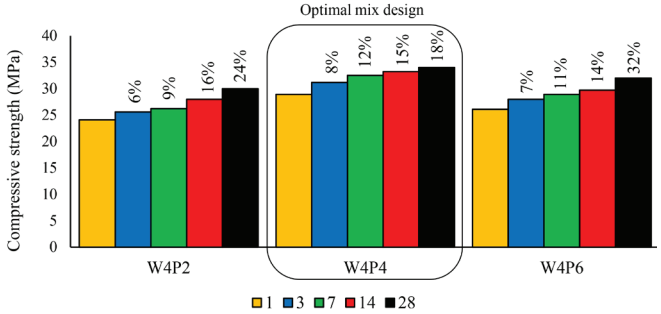

Fig. 4 *Compressive strength of the mix designs at the age of 28 days for the different curing periods (SP type: PCE and W/C ratio= 0.4)*

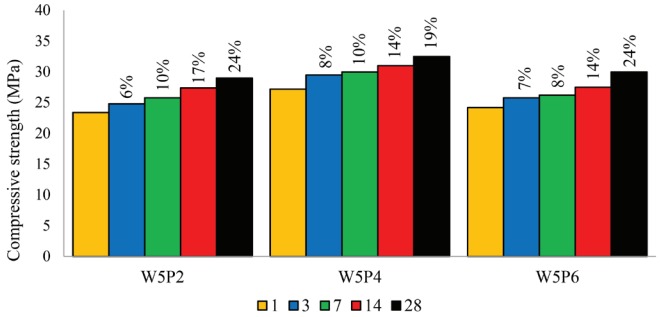

Fig. 5 *Compressive strength of the mix designs at the age of 28 days for the different curing periods (SP type: PCE and W/C ratio=0.5)*

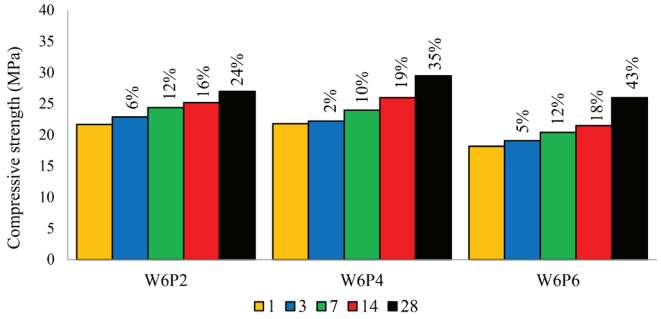

Fig. 6 *Compressive strength of the mix designs at the age of 28 days for the different curing periods (SP type: PCE and W/C ratio=0.6)*

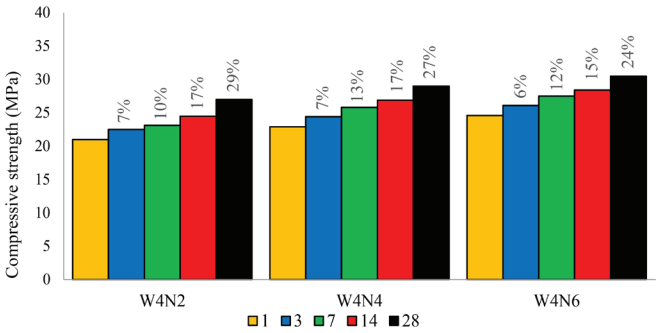

Fig. 7 *Compressive strength of the mix designs at the age of 28 days for the different curing periods (SP type: PNS and W/C ratio=0.4)*

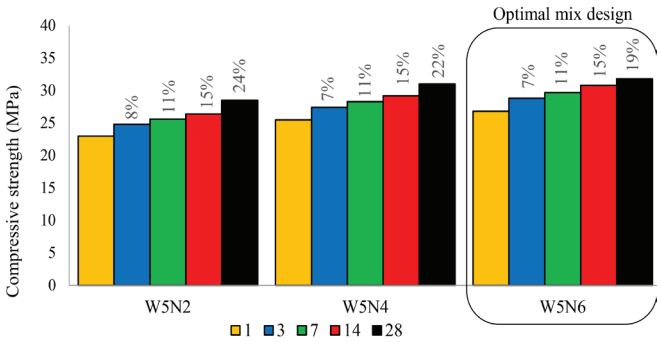

Fig. 8 *Compressive strength of the mix designs at the age of 28 days for the different curing periods (SP type: PNS and W/C ratio=0.5)*

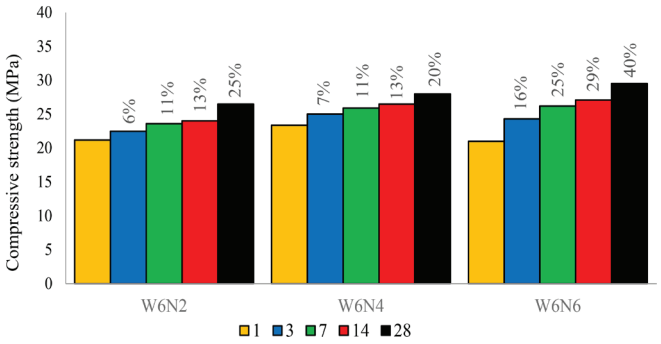

Fig. 9 *Compressive strength of the mix designs at the age of 28 days for the different curing periods (SP type: PNS and W/C ratio=0.6)*

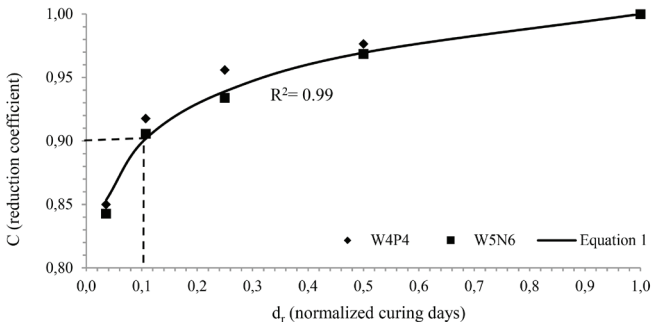

Fig. 10 *The reduction coefficient (C) of the strength of the 28-day concrete in terms of the normalized curing days (d_r)*

3.2 Evaluation of the concrete's strength at different ages

Regarding the test results (they are not reported herein), the ratios of the concrete's compressive strength at the specified age relative to the full setting of the 28-day concrete's strength are estimated and shown in Figs. 11 and 12. The strength was gained at different ages by considering the complete curing for two different types of SP (PCE and PNS).

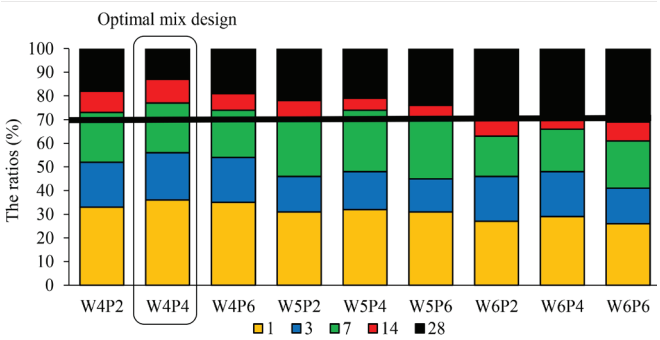

Fig. 11 *The ratios of the concrete's compressive strength at the specified age relative to the full setting of the 28-day concrete (SP type: PCE)*

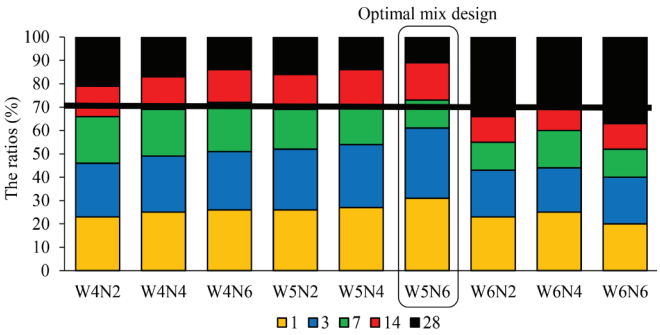

Fig. 12 *The ratios of the concrete's compressive strength at the specified age relative to the full setting of the 28-day concrete (SP type: PNS)*

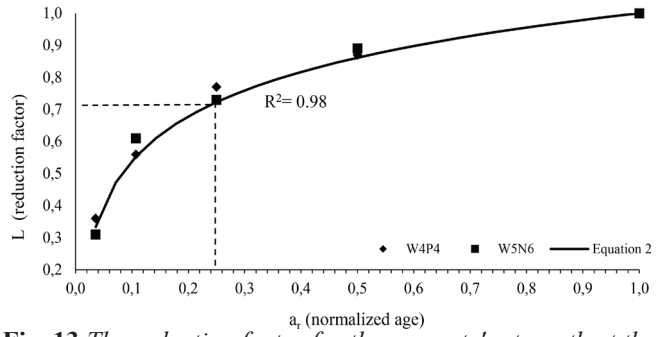

Fig. 13 *The reduction factor for the concrete's strength at the specified age relative to the 28-day strength in terms of the normalized age*

Based on recent field investigations in Iran, 70% of the design load consists of the dead load and anticipated construction loads. Therefore, 70% of the concrete's characteristic strength in the current research was considered as the main criterion for removing the formworks and shoring system. In this way, the structure is stable in the case of the loads applied. The 70% ratio line is plotted in these figures as well.

As shown in Figs. 11 and 12, it was observed that in the case of the W4P4 and W5N6 samples (optimal mix designs), the concrete at the age of 7 days shows adequate compressive strength and provides the possibility for removing the formworks and shoring system. Therefore, we have concluded that 7 days curing time shall be considered as the proper time interval to interrupt concrete works between the different parts of a structure.

In order to quantify the test results and estimate the compressive strength at different ages, the following equation is proposed for the two optimal mix designs (W4P4 and W5N6). This equation was obtained by curve fitting, the data for which are presented in Figs. 11 and 12 (see Fig. 13).

$$L = 0.2 ln a_r + 1 \quad (2)$$

where

L is the reduction factor for the concrete's strength at the specified age relative to the 28-days strength, and a_r is the normalized age (the age of the concrete at the time of the breaking test divided by 28 days for the complete setting).

Again, the diagram displays good agreement between Eq. (2) and the experimental results (correlation coefficient: R^2 is 0.98). Moreover, according to Fig. 13, the concrete reaches 70% of the full 28-day setting in a_r=0.25, which is equivalent to 0.25*28 days ≈ 7 days. It confirms that 7 days is appropriate as the time interval.

3.3 Statistical analysis

The aim of this section is to investigate the impact rate of parameters such as the SP type and its dosage, curing time, and W/C ratio on the 28-day concrete's compressive strength and the evaluation of strength at different ages in terms of the probabilistic approach. Since the data are in the form of paired observations, a two-sample t-test was used for the statistical analysis.

In this method, the two-sample problem is essentially reduced to a one-sample problem by using the computed differences $d_1, d_2, \ldots, d_n$. Thus, the hypothesis is reduced to

$$H_0: \mu_1 - \mu_2 = d_0 \quad (3)$$

where μ_1 and μ_2 represent the population means.

H_0 is rejected at the significance level of α when the computed t-statistic

$$t = \frac{\bar{d} - d_0}{s_d/\sqrt{n}} \quad (4)$$

exceeds $t_{\alpha/2,\, n-1}$ or is less than $-t_{\alpha/2,n-1}$ (Critical regions). A level of significance of α = 0.05 was chosen for this research. Variable n, is the sample size to perform the test.

In Eqs. (3) and (4), $\bar{d}$ and S_d are random variables representing the sample mean and standard deviation of the differences of the observations (Walpole et al. 2016). The experimental data form the observations in this research. Variable d_o, shows the value of the improvement or decline in the aforementioned parameters. In this way, the statistical analysis is separately conducted in the two following sub-sections:

3.3.1 The impact rate of the SP type and its dosage, curing time and W/C ratio on the compressive strength of the 28-day concrete

In this sub-section, the impact rate of the SP type and its dosage, curing time and W/C ratio on the compressive strength of the 28-day concrete are examined respectively. It should be noted that all the data illustrated in this phase of the statistical analysis were extracted from Table 3.

3.3.1.1 The impact rate of the SP type on the compressive strength of the 28-day concrete

In Table 4, the mean values ($\bar{d}$) and standard deviations (S_d) were estimated for an increase in the compressive strength of the 28-day concrete at different ages of the curing time for the samples containing the PCE type with reference to the PNS type. The improvements in the compressive strength (d_0) are reported as well by equalizing Eq. (4) with $t_{\alpha/2,n-1}$=2.306 (for the sample size of n=9).

Figure 14 displays the rate of increase in the compressive strength for the samples containing the PCE type relative to the PNS type. The rate is defined as variable d_0 divided by the average value of the 28-day concrete's compressive strength for the samples containing the PNS type. All the data are reported for the different ages of the curing time. According to Figure 14, the SP type can be effective on the concrete's compressive strength up to 10%.

3.3.1.2 The impact rate of the SP dosage on the compressive strength of the 28-day concrete

In Table 5, the mean values ($\bar{d}$) and standard deviations (S_d) of the increase in the compressive strength of the 28-day concrete are reported for samples with different SP dosages regarding the sample containing 0.2% SP. The improvement values (d_0) in the compressive strength are reported as well by equalizing Eq. (4) with ($t_{\alpha/2,n-1}$=2.045 for the sample size of n=30).

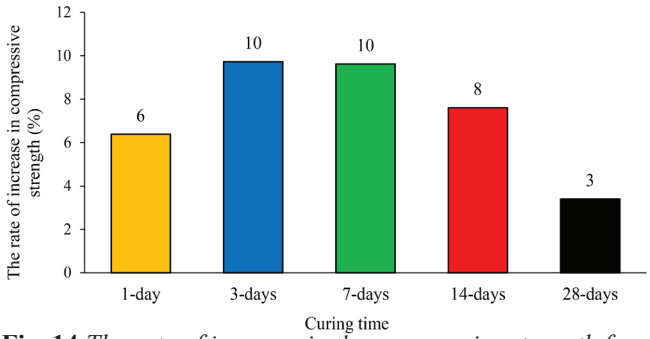

Fig. 14 *The rate of increase in the compressive strength for the samples containing the PCE type relative to the PNS type*

Tab. 5 *Mean values ($\bar{d}$) and standard deviations (S_d) for the increase in the compressive strength of the 28-day concrete along with their improvements (d_0) for the samples with different SP dosages regarding the samples containing 0.2% SP (MPa)*

0.4% SP			0.6% SP		
$\bar{d}$	S_d	d_0	$\bar{d}$	S_d	d_0
2.77	1.64	2.2	1.57	2.56	0.6

To estimate the rate of increase in the 28-day compressive strength for the samples containing different dosages relative to the samples with 0.2% SP, it was required to divide the variable d_0 by the average value of the 28-day concrete's compressive strength for the samples with 0.2% SP. These rates are estimated at 8% and 2% for the samples with 0.4% and 0.6% SPs, respectively (indicating an effect on the concrete's compressive strength of up to 8%).

3.3.1.3 The impact rate of the curing time on the compressive strength of the 28-day concrete

In Table 6, the mean values ($\bar{d}$) and standard deviations (S_d) are reported for the increase in the compressive strength of the 28-day concrete for the samples with different days curing relative to the samples with one-day curing. The improvements in the compressive strength (d_0) are reported as well by equalizing Eq. (4) with ($t_{\alpha/2,n-1}$=2.11 for the sample size of n =18).

Figure 15 indicates the rate of increase in the 28-day concrete's compressive strength for the samples with different days of curing compared to one-day curing. The rate is defined as variable d_0 divided by the average value of the compressive strength of the 28-day concrete for the samples with one-day curing. According to Figure 15, the complete curing of the concrete can improve the concrete's strength by up to 23%.

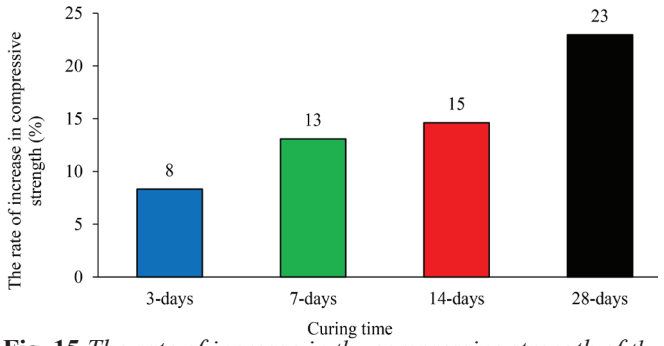

Fig. 15 *The rate of increase in the compressive strength of the 28-day concrete for the samples with different curing times regarding the samples with one-day curing*

Tab. 4 *Mean values ($\bar{d}$) and standard deviations (S_d) for the increase in the 28-day concrete's compressive strength along with their improvements (d_0) at different ages of the curing time for samples containing the PCE type with reference to the PNS type (MPa)*

Curing Time														
1-day			3-days			7-days			14-days			28-days		
$\bar{d}$	S_d	d_0	$\bar{d}$	S_d	d_0	$\bar{d}$	S_d	d_0	$\bar{d}$	S_d	d_0	$\bar{d}$	S_d	d_0

Tab. 6 *Mean values ($\bar{d}$) and standard deviations (S_d) for the increase in the compressive strength of the 28-day concrete along with their improvements (d_0) for the samples with different curing days regarding the samples with one-day curing (MPa)*

Curing Time											
3-days			7-days			14-days			28-days		
$\bar{d}$	S_d	d_0	$\bar{d}$	S_d	d_0	$\bar{d}$	S_d	d_0	$\bar{d}$	S_d	d_0
1.66	0.62	2.0	2.73	0.73	3.1	3.79	0.69	3.5	5.93	1.04	5.4

3.3.1.4 The impact rate of the W/C ratio on the compressive strength of the 28-day concrete

In Table 7, the mean values ($\bar{d}$) and standard deviations (S_d) are reported for the decrease in the compressive strength of the 28-day concrete for samples with different W/C ratios compared to the samples with a 0.4 W/C ratio. The decrease in values (d_0) in the compressive strength are estimated by equalizing Eq. (4) with ($t_{\alpha/2,n-1}$=2.045 for the sample size of n =30).

Tab. 7 *Mean values ($\bar{d}$) and standard deviations (S_d) for the decrease in the compressive strength of the 28-day concrete along with their decrease (d_0) for the samples with different W/C ratios regarding the samples with 0.4 W/C ratio (MPa)*

0.5 W/C ratio			0.6 W/C ratio		
$\bar{d}$	S_d	d_0	$\bar{d}$	S_d	d_0
0.31	2.04	0.45	-3.27	3.37	2.00

To estimate the rate of decrease in the 28-day compressive strength for the samples with different W/C ratios compared to the samples with a 0.4 W/C ratio. It is necessary to divide the variable d_0 by the average value of the compressive strength of the 28-day concrete for the samples with 0.4 W/C ratio. These rates are estimated at 2% and 7% for the samples with 0.5 and 0.6 W/C ratios, respectively (indicating the effect on the concrete's compressive strength of up to 7%).

3.3.2 The evaluation of the concrete's compressive strength at different ages

All the data used in the statistical analysis of this subsection were obtained from Figures 11 and 12. In Table 8, the mean values ($\bar{d}$) and standard deviations (S_d) of the decrease in the concrete's compressive strength at different ages are compared to the 28-day concrete's compressive strength. The decrease in values (d_0) in the compressive strength are estimated by equalizing Eq. (4) with ($t_{\alpha/2,n-1}$=2.11 for the sample size of n=18). The rate of the gain in strength (R) is defined as the difference between the average value of the full setting of the 28-day concrete's strength and d_0 divided by the average value of the full setting of the 28-day concrete's strength (%).

In Figure 16, the rates of the gain in strength (R) are plotted to enable a better visualization. This figure also shows a 70% ratio line in which the molds and shoring systems can be removed. It corresponds to the concrete's age in 7 days with complete curing during this period. In confirmation of what was stated in the section "The evaluation of concrete strength at different ages" above, a 7-day time interval for stopping the pouring of concrete with the complete curing process during this period is proposed.

4 CONCLUSIONS

This paper proposes a practical and state-of-the-art solution for the time management of construction. It should be emphasized that all the results were valid for the ambient conditions in this project. Considering the experimental results and statistical analysis, the following conclusions may be drawn:

1. In a mix design containing SP of the carboxylate type with a cement percentage of 0.4 and a W/C ratio of 0.4, the maximum compressive strength can be obtained. Therefore, it is defined as the optimal mix design for this type of SP.

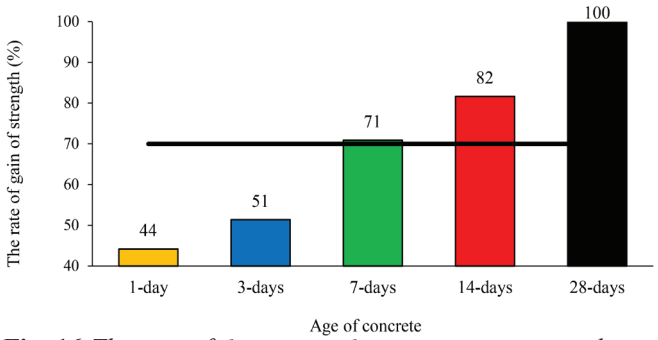

Fig. 16 *The rate of the gain in the compressive strength at different ages regarding the full setting of the 28-day concrete's strength*

Tab. 8: *Mean values ($\bar{d}$) and standard deviations (S_d) of the decrease in the concrete's compressive strength along with their rates (R) at different ages regarding the 28-day concrete's compressive strength (%)*

Curing Time														
1-day			3-days			7-days			14-days			28-days		
$\bar{d}$	S_d	R	$\bar{d}$	S_d	R	$\bar{d}$	S_d	R	$\bar{d}$	S_d	R	$\bar{d}$	S_d	R
58.50	5.34	44	51.33	5.50	51	32.50	6.88	71	22.22	7.80	82	0.00	0.00	100

2. In a mix design containing SP of the naphthalene type with a cement percentage of 0.5 and a W/C ratio of 0.6, the maximum compressive strength can be obtained. Therefore, it is selected as the optimal mix design for this type of SP.
3. The results indicate that 3 days of curing is appropriate for the time management of the project and for achieving the required strength at 28 days. Moreover, it is concluded that 7 days' curing time can be considered as the proper time interval to interrupt concrete works between different parts of a structure. For this purpose, two formulas were suggested.
4. The statistical analysis shows that the change in SP type, its dosage, and W/C ratio have an impact rate on the compressive strength of up to 10%, whereas the change in the curing time is effective up to 23%.
5. Considering the statistical analysis derived based on the experimental data, 7 days has been determined as the time interval for concrete works between different parts of a structure. This interval time has been specified for the two optimal mix designs. Consistent curing is essential during this time period, as it ensures that the structure will be stable and support all the loads imposed.

Acknowledgments

The authors would like to acknowledge the mechanical testing facilities at Pey Azma Beton Kouhestan Laboratory in Rasht, Iran, for their assistance.

REFERENCES

ACI Committee 318: Building Code Requirements for Structural Concrete (ACI 318-19) and Commentary (ACI 318R-19). American Concrete Institute, Farmington Hills. MA, USA 2019.

ASTM C150: Standard specification for Portland cement. American Society For Testing And Materials. 2004.

ASTM C33: Standard Specification for Concrete Aggregates. 2003.

ASTM C39: Standard Test Method for Compressive Strength of Cylindrical Concrete, Specimens. 2014.

Adjoudj M. H. - Ezziane K. - Kadri E. H. - Ngo T. T. – Kaci A. (2014). *Evaluation of rheological parameters of mortar containing* various *amounts of mineral addition with polycarboxylate superplasticizer.* Constr. Build. Mater. 70 (2014): 549–559. https://DOI:10.1016/j.conbuildmat.2014.07.111.

Aliabdo Ali A. - Abd Elmoaty M. Abd Elmoaty - Hazem A. Salem. (2016). *Effect of cement addition, solution resting time and curing characteristics on fly ash based geopolymer concrete performance.* Construction and Building Materials. 123 (2016): 581–593. http://dx.doi.org/10.1016/j.conbuildmat.2016.07.043

Baghabra Al-Amoudi O. S. - Abiola T. O. - Maslehuddin M. (2006). *Effect of superplasticizer on plastic shrinkage of plain and silica fume cement concretes.* Constr. Build. Mater. 20 (9): 642–647. http://DOI:10.1016/j.conbuildmat.2005.02.024.

Carazeanu, I. - Chirila E. - Georgescu M. (2002). *Investigation of the hydration process in 3CaO–Al2O3–CaSO4–2H2O–plasticizer–H2O systems by X-ray diffraction*. Talanta, 57 (4): 617–623. https://doi.org/10.1016/S0039-9140(02)00100-5.

Cartuxo, F. - de Brito J. - Evangelista L. - Jiménez J. R. - Ledesma E. F. (2015). *Rheological behaviour of concrete made with fine recycled concrete aggregates – influence of the superplasticizer.* Constr. Build. Mater. 89 (2015): 36–47. https://DOI:10.1016/j.conbuildmat.2015.03.119.

Chen, S. - Ting-shu H. - Zhang G. – Wang X. – Yanyan H. (2016). *Effects of superplasticizers on carbonation resistance of concrete.* Construction and Building Materials. 108 (2016): 48–55. https:// DOI:10.1016/j.*conbuildmat*.2016.01.037.

Da C. - Xiao-tong Y. - Jun S. - Ying-di L. - Yan Z. (2017). *Investigation of the curing time on the mechanical behavior of normal concrete under triaxial compression.* Construction and Building Materials. 147 (2017): 488-496. https://doi.org/10.1016/j.conbuildmat.2017.04.180.

El-Ashkar N. - Nanko H. - Kurtis K. (2007). *Effect of moisture state on mechanical behavior and microstructure of pulp fiber-cement mortars.* J. Mater. Civ. Eng. 19(8), https://doi.org/10.1061/(ASCE)0899-1561(2007)19:8(691).

Fang S. - Lam S. S. E. - Li B. - Wu B. (2020). *Effect of alkali contents, moduli and curing time on engineering properties of alkali activated slag.* Construction and Building Materials. 249 (2020): 118799. https://doi.org/10.1016/j.conbuildmat.2020.118799.

Ferrari, L. - Kaufmann, J. – Winnefeld F. – Plank J. (2010). *Interaction of cement model systems with superplasticizers* investigated *by atomic force microscopy, zeta potential, and adsorption measurements.* J. Colloid Interface Sci. 347 (1): 15–24. https://doi.org/10.1016/j.jcis.2010.03.005.

Felekoglu B. - Tosun-Felekoglu K. – Ranade R. – Zhang Q. – Li V. C. (2014). *Influence of matrix flowability, fiber mixing procedure, and curing conditions on the mechanical performance of HTPP-ECC.* Compos. PART B-Eng., 60: 359–370.

Gołaszewski J. - Szwabowski, J. (2004). *Influence of superplasticizers on rheological behaviour of fresh cement mortars.* Cem. Concr. Res. 34 (2): 235–248. https://DOI:10.1016/j.cemconres.2003.07.002.

Haghighatnejad N. - Yasin Mousavi S. - Jalal Khaleghi S. - Tabarsa A. - Yousefi S. (2016). *Properties of recycled PVC aggregate concrete under different curing conditions.* Construction and Building Materials. 126 (2016): 943–950. http://dx.doi.org/10.1016/j.conbuildmat.2016.09.047.

Hui M. - Qian S. - Zhang Z. (2014). *Effect of self-healing on water permeability and mechanical property of medium-early-strength engineered cementitious composites.* Constr. Build. Mater., 68(15): 92–101.

Kim J.-K. - Moon Y.H. - Eo S.H. (1998). *Compressive strength development of concrete with different curing time and temperature.* Cement and Concrete Research. PP: 28 (12): 1761-1773. https://doi.org/10.1016/S0008-8846(98)00164-1.

Kreppelt F. – Weibel M. – Zampini D. – Romer M. (2002). *Influence of solution chemistry on the hydration of polished clinker surfaces—a study of different types of polycarboxylic acid-based admixtures.* Cem. Concr. Res. 32 (01): 187–198. https://DOI: 10.1016/S0008-8846(01)00654-8.

Lange A. - Hirata T. - Plank J. (2014). *Influence of the HLB value of polycarboxylate superplasticizers on the flow behavior of mortar and concrete.* Cem. Concr. Res. 60 (2014): 45–50. https://DOI: 10.1016/j.cemconres.2014.02.011.

Li Y. – Yang C. - Zhang Y. – Zheng J. – Guo H. – Lu M. (2014). *Study on dispersion, adsorption and flow retaining behaviors of cement mortars with TPEG-type polyether kind polycarboxylate superplasticizers.* Constr. Build. Mater. 64 (2014): 324– 332. https://DOI:10.1016/j.conbuildmat.2014.04.050.

Madandoust R. - Kazemi M. - Khakpour Talebi P. - de Brito J. (2019). *Effect of the curing type on the mechanical properties of lightweight concrete with polypropylene and steel fibres.* Construction and Building Materials. 223 (2019): 1038–1052. https://doi.org/10.1016/j.conbuildmat.2019.08.006

Mollah M. Y. A. – Adams W. J. – Schennach R. – Cocke D. L. (2000). *A review of cement– superplasticizer interactions and their models*. Adv. Cem. Res. 12 (4): 153–161. https://DOI:10.1680/adcr.2000.12.4.153

Palacios M. - Puertas F. – Bowen P. – Houst Y. F. (2009). *Effect of PCs superplasticizers on the rheological properties and hydration process of slag-blended cement pastes.* J. Mater. Sci. 44 (10): 2714–2723. https://DOI:10.1007/s10853-009-3356-4.

Perrot A. - Rangeard D. - Picandet V. – Mélinge Y. (2013). *Hydro-mechanical properties of fresh cement pastes containing polycarboxylate superplasticizer.* Cem. Concr. Res. 53 (2013): 221–228. http://DOI:10.1016/j.cemconres.2013.06.015

Puertas F. - Santos H. - Palacios M. - Martínez-Ramírez S. (2005). *Polycarboxylate superplasticiser admixtures: effect on hydration, microstructure and rheological behaviour in cement pastes.* Adv. Cem. Res. 17 (2): 77–89. https://DOI:10.1680/adcr.17.2.77.65044.

Toledano-Prados M. - Lorenzo-Pesqueira M. - González-Fonteboa B. - Seara-Paz S. (2013). *Effect of polycarboxylate superplasticizers on large amounts of fly ash cements.* Constr. Build. Mater. 48 (2013): 628–635. https://DOI:10.1016/j.conbuildmat.2013.07.069.

Uchikawa H. - Hanehara S. – Shirasaka T. – Sawaki D. (1992). *Effect of admixture on hydration of cement, adsorptive behavior of admixture and fluidity and setting of fresh cement paste.* Cem. Concr. Res. 22 (6): 1115–1129. http://dx.doi.org/10.1016/0008–8846(92)90041-S.

Yamada K. – Takahashi T. – Hanehara S. - Matsuhisa M. (2000). *Effects of the chemical structure on the properties of polycarboxylate-type superplasticizer.* Cem. Concr. Res. 30 (2): 197–207. https://DOI: 10.1016/S0008-8846(99)00230-6.

Yu Y. - Liu J. - Ran Q. - Qiao M. - Zhou D. (2013). *Current understanding of comb-like copolymer dispersants impact on the hydration characteristics of C3A– gypsum suspension.* J. Therm. Anal. Calorim. 111 (2013): 437–444. https://DOI: 10.1007/s10973-012-2430-3.

Yu K. - Dai J. - Lu Z. - Leung C. (2015). *Mechanical properties of engineered cementitious composites subjected to elevated temperatures.* J. Mater. Civ. Eng. 27 (10). https://doi.org/10.1061/(ASCE)MT.1943-5533.0001241.

Yildirim G. - Sahmaran M. - Ahmed H. (2015). *Influence of hydrated lime addition on the self-healing capability of high-volume fly ash incorporated cementitious composites.* J. Mater. Civ. Eng. 27 (6). https://doi.org/10.1061/(ASCE)MT.1943-5533.0001145.

Walpole R. E. – Myers R. H. - Myers S. L. - Ye K. E. (2016). *Probability & Statistics for Engineers & Scientists. Ninth ed.*

Wu M. - Johannesson B. – Geiker M. (2012). *A review: Self-healing in cementitious materials and engineered cementitious composite as a selfhealing material.* Constr. Build. Mater., 28(1): 571–583. https://doi.org/10.1016/j.conbuildmat.2011.08.086.

Zhu Y. - Zhang Z. C. - Yang Y. Z. - Yao Y. (2014). *Measurement and correlation of ductility and compressive strength for engineered cementitious composites (ECC) produced by binary and ternary systems of binder materials: Fly ash, slag, silica fume and cement.* Constr. Build. Mater., 68: 192–198. https://doi.org/10.1016/j.conbuildmat.2014.06.080.

Zhu Y. - Zhang Z. - Yao Y. - Guan X. - Yang Y. (2016). *Effect of Water-Curing Time on the Mechanical Properties of Engineered Cementitious Composites.* Journal of Materials in Civil Engineering. 28 (11) 04016123-1. DOI: 10.1061/(ASCE)MT.1943-5533.0001636.

Zhang Y. – Kong X. (2014). *Influences of superplasticizer, polymer latexes and asphalt emulsions on the pore structure and impermeability of hardened cementitious materials.* Constr. Build. Mater. 53 (2014): 392–402. http://DOI:10.1016/j.conbuildmat.2013.11.104.

sciendo

Slovak Journal of Civil Engineering

Vol. 32, 2024, No. 2, 48 – 57
DOI: 10.2478/sjce-2024-0013

A METHODOLOGY FOR A COMPREHENSIVE EVALUATION OF AN URBAN TRANSPORT NETWORK STRUCTURE USING GEOGRAPHICAL INFORMATION SYSTEMS (GIS)

Kurre Sai Sahitya[1]*, C.S.R.K. Prasad[2]

Abstract

The transportation network is the most important component of an urban infrastructure. The efficiency of a region's transportation system can be understood by the effectiveness of its transport network arrangement. The current study employs Geographical Information Systems (GIS) to assess the structure of a transport network in various clusters of the Hyderabad Metropolitan Area (HMA). The study focuses on a thorough assessment of the transport (or) road network structure in terms of various criteria such as connectivity, accessibility, maturity, and development. The study also categorizes each Transport Network Structural Evaluation Criteria (TNSEC) level as "very low, low, medium, high, or very high". The goal of this research is to create a Road Network Structural Performance Index (RNSPI), which is usually used to measure the efficiency of a study area's transportation network structure. The study's findings serve as a foundation for city transportation planners to put efforts in the planning to enhance network facilities in the study region. The study also investigates the utility of Arc GIS software in assessing the structure of an urban transport network.

Address

[1] Assistant Professor, Department of Civil Engineering, VNR Vignana Jyothi Institute of Engineering and Technology, Hyderabad, Telangana, India

[2] Professor, Department of Civil Engineering, National Institute of Technology, Warangal, Warangal, Telangana, India

* ***Corresponding author:*** saisahitya_k@vnrvjiet.in

Key words

- Comprehensive;
- Evaluation;
- Transport network;
- RNSPI;
- GIS.

1 INTRODUCTION

Urban road networks are described as the supporting structures for our society and economy (Shang, 2017). Urban road networks can be described as typically complex networked systems as there are many spatial components with complicated structures and interactions between different components (Goh et al., 2016). An excellent urban road network can be chiefly defined by four significant criteria: connectivity, accessibility, maturity, and development (Sreelekha et al., 2020).

An evaluation of a road network is necessary to understand the situation of an existing road network. The Road networks can be evaluated concerning their topological spatial structure and performance characteristics. Topological characteristics can be represented by the spatial structure of the networks, whereas performance characteristics are related to the operational issues in a network (Mohammadi, 2013). Road networks have different structural characteristics that exhibit geometrical and topological variations.

"Topology" is defined as "the arrangement and connectivity of nodes and links" in the road network (Xie and Levinson, 2007). The topological structure of networks can be evaluated concerning their accessibility, "connectivity", hierarchy, and morphology (Mohamamdi, 2013). An evaluation of connectivity is based upon indices extracted from a graph of a road network analysis (Kansky, 1963; Marshall, 2005). The hierarchy of road networks is the classification of roads in a network based on the function of the roads (Xie and Levinson, 2007). The "hierarchy" of a road network can be classified into a functional hierarchy and an operational hierarchy. Generally, link-

based measures evaluate the operational and functional hierarchies of road networks by using the concept of entropy (Xie and Levinson, 2005). Generally, "accessibility" is evaluated concerning the attractiveness component (usually measured as having several opportunities at destinations) or an impedance function (usually measured in terms of distance or travel time) (Ingram, 1971). The "morphology" of a road network which is represented with the shape or pattern of the network, is generally evaluated and analyzed using fractal geometry or fractal dimension analysis (Rodin and Rodina, 2000).

Road network performance characteristics are evaluated based on the dynamic and functional characteristics of the network. The most critical measures to evaluate the functional characteristics of road networks are the road index (which is a function of a road's density, length, condition, population coverage, and traffic load) and the inter-nodal distance index (Santosa and Basuki, 2005), commercial speed and frequency (Gattuso and Miriello, 2005), capacity-volume ratio (Dhenadayalu et al., 2004), vehicle-kilometres (Scot et al., 2005) and robustness index of the network (function of the capacity, flows and topology) (Scot et al., 2006). The performance of road networks can also be measured in terms of their reliability, criticality, efficiency and vulnerability (Mohammadi, 2013). An evaluation of a road network provides a clear insight as to the situation of an existing road network which gives an understanding of the measures to be taken to improve it. The evaluation of a road network with respect to multi-dimensional criteria provides a base to balance a road network's structural growth in a city to improve the transportation system's efficiency.

Urban roads are a fundamental infrastructure that allows city dwellers to access various urban emergency, education, infrastructure, and recreational services. To reap significant benefits from urban areas, there must be a satisfactory level of accessibility, which includes the connectivity of various roads to various urban services. There is a need to address various issues in urban transportation and improve modernization to meet people's increasing demands. Inadequate network planning causes problems with connectivity, accessibility, mobility, and safety on the transport network. To enhance the quality of a transportation framework, it is necessary to make better use of the existing infrastructure. In the current scenario, an evaluation of a transport network is becoming increasingly important for planning an effective and efficient transportation system. An evaluation of a transport network may assist transportation planning authorities in implementing better planning practices to improve the network, develop its functional efficiency, make better use of existing infrastructure, and reduce network disparities. The current study is aimed as providing a detailed methodology for evaluating the structure of a transport network in terms of its connectivity, accessibility, maturity, and development. The present study also aims to show the quality of the study area's road network structure.

2 LITERATURE REVIEW

The problems in the connectivity, accessibility, mobility, and safety of a road network are caused due to the improper planning of networks. In order to enhance the efficiency of a transportation system, there is a need to use the existing infrastructure efficiently. The evaluation and modelling of a road network are becoming more prominent for planning an effective and efficient transportation system. An evaluation of a road network may help transportation planning authorities implement better planning practices to improve the network, develop its functional efficiency, effectively use the existing infrastructure, and decrease any network disparities.

There are several criteria and methods available in the literature to evaluate the structure of a road network. Some of them are direct empirical methods, while some are indirect methods. The direct empirical methods are generally estimated using nodes and links in the transportation network. The indirect methods are quantified using various components such as land use, time, distance, length and area. The study's have identified that a road network's connectivity, accessibility, maturity, and development are the essential criteria to be evaluated to understand the performance of a road network's structure. Some of the studies related to the methods used to evaluate a road network's connectivity, accessibility, maturity and development are reviewed in a detailed manner.

Connectivity refers to the density of connections in path or road networks and the directness of any links. A well-connected network has many short links, numerous intersections, and minimal dead ends (cul-de-sacs). As connectivity increases, travel distances decrease, and route options increase, allowing for more direct travel between destinationsand thereby creating a more accessible and resilient system (Victoria Transport Policy Institute, 2017). The interconnectedness of a road in a transportation network could be evaluated in terms of a connectivity index. Generally, a connectivity index is obtained by dividing the number of links by the number of nodes (Ewing, 1996). Graph theory measures are most commonly used in measuring road network connectivity (Hanson, 1986). There are three primary connectivity measures: alpha, beta, and gamma indices, which are based on the graph theory. These indices were computed concerning the number of nodes and links present in a road network. They are used to describe the structural connectivity of the road network. However, they are also applicable for explaining the changing structure of networks (Kansky, 1963). Generally, the connectivity indices are expressed on a scale of 0.0 to 1.0. An index over 0.75 is desirable and shows a greater degree of connectivity (Hanson, 1986). Other connectivity measures such as a street network's density (miles per square mile.), connected-node ratio, intersection density, and link-node ratio were subsequently evaluated for increasing bicycling and walking.

Preliminary results have been presented by applying such connectivity measures to the Portland, Oregon region. The connectivity measures were positively correlated but showed inconsistencies in assigning the same level of connectivity for a tract. The alpha index increased connectivity by providing multiple and alternative routes (Dill, 2004). Researchers have described some more connectivity measures along with graph theory measures to evaluate the overall network connectivity of China's railway network. The alpha index, beta index, gamma index, Cyclomatic number, distance matrix, and nodal accessibility coefficient were measured to analyse the expansion of the railway network. The greater the value of the above indices, the better a network is connected. An expansion in the railway network indicates a perfect correlation with the economic and urban development of a region (Wang et al., 2009).

The Aggregate Transportation Score (ATS), which is simply the summation of the Cyclomatic number and the alpha, beta and gamma indices, describes a road network's overall connectivity. A higher value of ATS indicates better road network connectivity (Ghosh, 2016).

Accessibility can be explained in many ways, including "the potential opportunities for interaction" (Hansen, 1959), "the ease with which any land use activity can be reached from a location using a particular transportation system" (Dalvi and Martin, 1976), "the freedom of individuals to decide whether or not to participate in different activities" (Burns, 1979), and "the benefits provided by a transportation or land use system" (Ben- Avika and Lerman, 1977). Accessibility may be chiefly classified in two ways: relative and integral accessibility. Relative accessibility is defined as "the degree to which two places or points on the same surface are connected" and integral accessibility as "the degree of interconnection with all the other points on the same surface." Ameasure based on the normal or Gaussian curve is the most suitable form for determining the integral accessibility at a given point (Ingram, 1971). There are different types of accessibility measures. The authors have tried to classify accessibility measures into three classes: 'infrastructure-based measures,' which focus on features of an infrastructure such as a road network's density, speeds on roads, 'opportunity-based measures' which are concerned with the opportunities for working, shopping, recreation, etc., and 'mixed measures', which integrate both network measures and opportunity measures (Wee et al., 2001). Accessibility can be estimated as the cost of moving people or goods from one place to another. Distance and travel time are two aspects considered in the measurement of accessibility. The centre of an urban area is where the highest degree of accessibility exists because of the convergence of different routes and systems (Lean and Goodall, 1977). Different studies have modelled accessibility in different ways such as a 'utility-based measure' (Ben-Avika and Lerman, 1977), a 'topological measure' (Mackiwicz et al., 1996), a 'gravity measure' (Hansen, 1959), an 'cumulative opportunity measure' (Ahmad Geneiddy and David Levinson, 2006), and a 'constraint based measure' (Wu and Miller, 2002).

An ***accessibility*** measure broadly integrates land use and transportation components. The quantification of accessibility has several uses, such as understanding the existing situation of a transportation system to examine the changes caused by inaccessibility because of the diversions in routes (or) changes in land use. The quantification and analysis of accessibility help policymakers take specific measures to improve the accessibility to different locations based on the results obtained from different accessibility indices. The addition of attractions accounts for the land-use aspect of an accessibility measure. Accessibility measures must include a behavioural component to be analysed. Accessibility can also be evaluated by other means such as the degree of a node, an associated number, and Shimbel's accessibility measure. Accessibility measures such as cumulative opportunities, gravity, and utility measures can measure accessibility to the maximum possible extent. A cumulative opportunity measure considers the distance and purpose of a trip to quantify its accessibility. It specifies a particular travel time or distance and uses the number of essential activities within that distance or time as the accessibility for that point. A gravity measure considers an attraction factor and separation factor continuously to examine the accessibility of different locations. The gravity model has an attraction factor weighted by the travel time or distance raised to some exponent. These models consider all the individuals as the same, which is the major limitation. A utility measure considers an individual's perceived utility for different travel choices. The time-space measure is a new dimension of accessibility that considers the individuals' time constraints travelling to a particular location. It is necessary to include all the dimensions such as the mode, time of day, type of activity, and spatial detail to measure the accessibility more precisely (Chandra Bhatt et al., 2000). A new planning paradigm necessitates a more thorough accessibility assessment. As transportation and land use planners develop better tools for quantifying accessibility impacts, such as multi-modal level-of-service indicators and models that measure the travel distances, time, and costs required by various types of transport system users to access various types of services and activities, the ability to evaluate accessibility is improved (Litman, 2021).

The ***maturity*** of road networks is analysed using fractal dimensions (Mohammadi et al., 2013). The term 'fractal' was first used by Mandelbrot (1975). Fractal geometry is applied in much of the literature to analyse the spatial pattern or morphology of a road network. A road network is one of the spatial phenomena which are complex in their nature and orientation. Many authors have stated that 'fractal geometry' is an efficient method to define the complexity of road networks. It is used to analyse the dissimilarities of networks which are utterly confused in nature (Frankhauser, 1992; Batty and Longley, 1994; Battylf, 1996; Falconer, 2004; Mandelbrot, 1977, 1982, 1967; Pietgen and Saupe, 1988; Shen, 1997; Mandelbrot, 1983; Falconer, 1986; De Cola and Lam, 1993; Hastings and Sugihara, 1993). Hausdorff's method (1918), which is specifically called fractal dimension, calculates a road network's coverage index, analyses the calculation results, and suggests optimising the road network. The geometry of urban residential development was fractal. Estimating fractal dimensions is based on the varying size of cities and the scale on which their form is identified. Space-filling was computed concerning the "size" and "scale." The increase in the radius or distance increases the size of the object measured. The required parameters are estimated using the least-squares regression method. The analysis of a size to the scaling relations was done only for the CBD area. The study indicated that this kind of analysis might be helpful to classify cities concerning their shape and density.Batty and Xie, (1996) tried to explain that when these parameters were integrated with economic and behaviour patterns, the functioning of the cities could be analysed in a much better way, which is essential for good planning. A transport network in a city exhibits fractal characteristics such as irregularity, self-similarity, and scale invariance. Thus, fractal analyses could be an efficient method for assessing and characterising a road network (Rodin and Rodina, 2000). The fractal aspect of urban transportation networks is generally analysed using the box-counting method (Sreelekha et al., 2017) and the mass-radius fractal method (Mohammadi et al., 2013). Later, a distributive continuous fractal analysis to evaluate a road network was introduced. There is a need to examine the fractal properties of cities on both "macro" and "micro" scales. A city is considered a continuous space, and fractal analysis is applied to every section of the city.

A new algorithm has been proposed for the box-counting fractal dimension method to continuously compute the fractal

dimension values on each section of a city. The mesh formed from the rectangular box dimension method is moved to the required place with a specified distance, and thus, fractal dimension values were calculated for different city sections. The conventional method could not describe the relationship between the fractal dimension and the city's geography, whereas the modified method can explain that relationship. Higher fractal dimension values indicate a better transportation network and a more developed economy (Sun et al., 2007). The complexity of road networks is concerned with the development of built-up areas and the network. A high fractal dimension value indicates the higher maturity of the transportation network in that area and vice-versa (Mohamamdi et al., 2013). The capability of using fractal dimensions as a method of "quantifying the qualitative" in terms of urban character helps find novel and innovative development techniques for a street network (Copper and Watkinson, 2010). The fractal characteristics of urban forms and road networks provide useful information for urban planning (Wee et al., 2017).

The ***development*** of a road network is evaluated using "coverage measures." Coverage measures describe the density aspect of the elements of a network, i.e; intersections and links. The higher the value, the more the network is developed. The growth of the transport network is described based on the network's length (Levinson, 2012) and density (Bento et al., 2003). A network's density and intersection density are attributable to its coverage in an area. A pattern analysis of the developemnt of a road network provides an empirical guide for planning and policy issues of urban development (Sreelekha et al., 2017). The compactness ratio, also known as a road network density, is the most widely accepted method for analysing urban sprawl (Purevtseren et al., 2018).

In recent years, GIS has been widely used as a powerful tool for road network analysis. GIS is the most efficient tool in solving various road network problems with promptness and accuracy (Adwani et al., 2005). GIS is used to maintain the road network data, integrate the data with other attributes, and visualise the results (Nijagunappa et al., 2007). The transport network analysis performed using GIS provides resilient and reliable results, which can be used as a base for transportation departments to enhance their techniques and analysis system (Arora and Kumar, 2011). ArcGIS-based network analysis provides solutions for different road network problems such as finding the most efficient travel route, generating travel directions, locating the closest facility, and defining service areas based on the travel time and distance covered (Kumar and Kumar, 2016). The merits and demerits of an existing transportation system can be evaluated using GIS. The need to improve the existing road network can be recognized with the help of a GIS-based road network analysis (Nalawade et al., 2015). A study was conducted to discuss the conditions of Slovakia for the common use of traffic engineering and urban planning. The main issue is the need for the preparation and rehabilitation of local urban roads and public spaces in cities in a complex 3D design. The study explained the integration of GIS and BIM. The integrated results would help in fulfilling the requirements of "sustainable mobility" and "smart cities" (Schlosser et al., 2022).

This section reviewed the literature on road network evaluation criteria and its methods. Road network analysis in different parts of the world help improve the road network facilities in those areas. The evaluation of road networks was limited only to small regions or small parts of the cities. There is a need to evaluate a road network in multi-dimensional aspects such as connectivity, accessibility, maturity, development, safety, and mobility. A city-level comprehensive transport network analysis in multi-dimensional aspects is necessary to understand the efficiency and performance of a network structure in an entire city.

3 DETAILED METHODOLOGY

The present study has been carried out in four phases. The first phase involves identification of the study area; the second phase focuses on evaluation of a transport network structure with respect to connectivity, accessibility, maturity and development; the third phase deals with the categorization of clusters in the study area with respect to the level of the structural evaluation criterion of the transport network and the fourth phase describes the development of a Road Network Structural Performance Index (RNSPI). The methodology adapted in the study is presented in Figure 1. The description of each phase of the study is explained in the following sections.

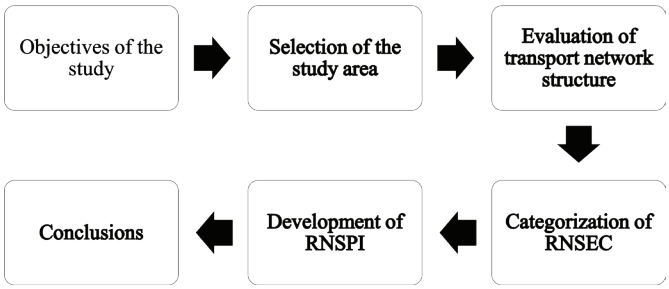

Fig.1 *Methodology adapted in the study*

3.1. Description of Study Area

Hyderabad, the capital of the state Telangana in India, was selected as the study location. The Hyderabad Metropolitan Area (HMA) is one of India's fastest-growing metropolises. With 9.5 million people, it is the country's sixth-largest metropolitan region (as per the 2011 census). The study area has a transport network that spans 5400 kilometres and covers an area of 7200 square kilometres. Figure 2 depicts the location of the study area.

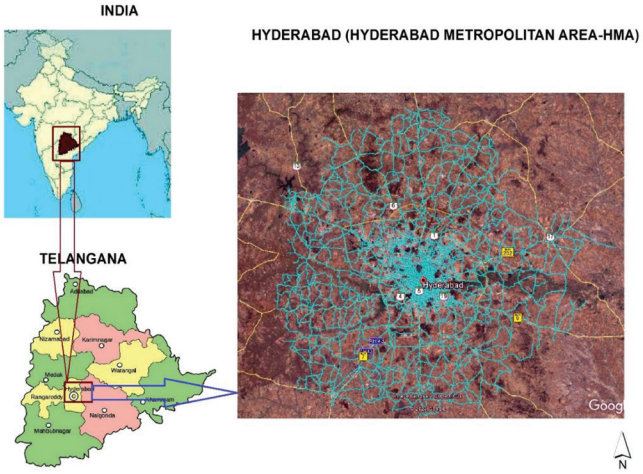

Fig. 2 *Location of the Study Area*

The transport network in 21 clusters of HMA was chosen for analysis. The clusters along with the transport network are shown in Figure 3. The classification of the clusters was considered from the Draft Final Report of the Comprehensive Transportation Study (CTS) for HMA, 2013.

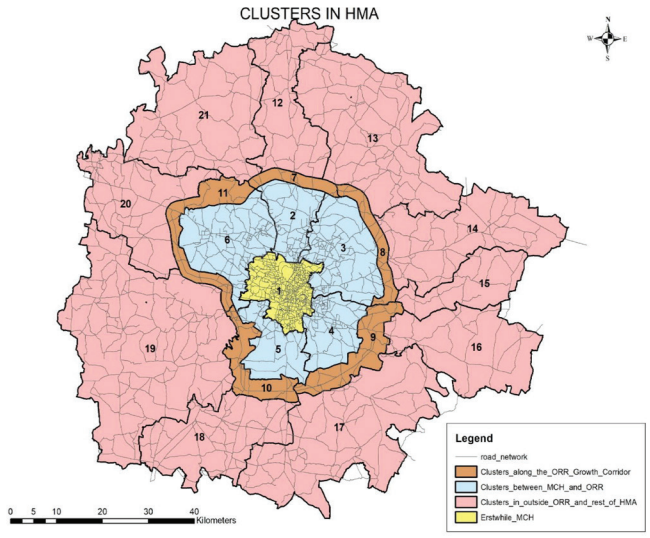

Fig. 3 *Map showing the transport network in different clusters of HMA*

3.2 Structural Evaluation Criteria of the Transport Network

Four key criteria are used to evaluate the transport network structure in the study area: connectivity, accessibility, maturity, and development of the network. Arc GIS 10.1 software was used to extract the features needed for the study, such as the number of nodes, the number of links, the length of the transport network, the size of the transport network, the built-up area, the number of utilities (or) urban services, and the distances. The methods for quantifying each of these criteria are given in detail below.

3.2.1 Connectivity of the Transport Network

To analyse the connectivity of the transport network, the study employs graph theory measures such as alpha, beta, gamma, Cyclomatic, and Aggregate Transportation Score (ATS). The greater the value of the indices, the better the transport network's connectivity. The alpha index, beta index, gamma index, and Cyclomatic Number were added together to form the ATS. As a result, the ATS can interpret the overall transport network's connectivity in a cluster. The empirical equations used to calculate the different connectivity measures are given in Eqs. (1) to Eq. (5).

$$\text{Alpha Index } (\alpha) = (e\text{-}v+1)/(2v\text{-}5) \quad (1)$$

$$\text{Beta Index } (\beta) = e/v \quad (2)$$

$$\text{Gamma Index } (\gamma) = e/3(v\text{-}2) \quad (3)$$

$$\text{Cyclomatic number } (\mu) = e\text{-}v+1 \quad (4)$$

$$\text{Aggregate Transportation Score } (ATS) = \beta+\alpha+\gamma+\mu \quad (5)$$

Where, e= number of edges / links, v= number of nodes / vertices

3.2.2 Accessibility of the Transport Network

The Accessibility Index (AI) is used to evaluate the accessibility of a study area's transport network. The number of utilities or urban services such as schools, colleges, ATMs, banks, hospitals, police stations, petrol stations, bus stops, parks, and theatres are computed in different clusters. The Weighted Scoring Model (WSM) was used to assign weights to various utilities. Different weights were assigned to the utilities, with an emergency receiving the highest priority, education coming in second, infrastructure coming in third, and recreation coming in fourth [9]. The accessibility index for different locations and clusters was computed using Eq. 6. The weights assigned to the different utilities are given in Figure 4.

$$\text{Accessibility Index } (AI) = \Sigma (W_i * N_{ir}) \quad (6)$$

Where,
W_i= Weights assigned to i^{th} utility (or) urban service and
N_{ir} = number of i^{th} opportunity at r^{th} radius

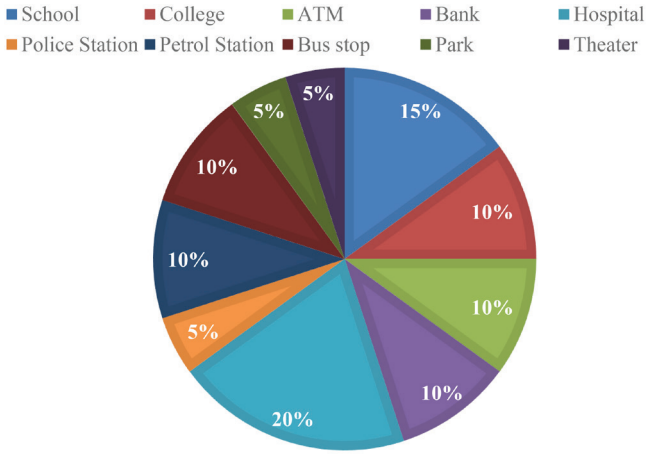

Fig. 4 *Weights Assigned to Different Utilities*

3.2.3 Maturity of Transport Network

Using fractal geometry, the maturity of the existing transportation network was quantified. The Box-Dimension method was used to calculate the fractal dimension. To evaluate the fractal dimensions in Arc GIS, a mesh with a grid size of 1km is created using Arc GIS's fishnet tool. Then, the transport network map within each cluster, was overlaid by this mesh, and the number of boxes covering the network was calculated. The same holds true for grid sizes of 2km, 3km, 4km, and 5km. The grid size and box count were calculated. As a linear plot, a double logarithmic plot of an inverse grid size and box count was created, yielding the box fractal dimension. The fractal dimensions (FD) of the 21 clusters were computed.

3.2.4 Development of the Transport Network

The density of a transport network is used to quantify its development. The length and area of a transport network in

Tab. 1 *Descriptive statistics of the road network parameters*

Cluster	Number of Nodes	Number of Links	Built-up area (sq. km)	Road network length (km)	Area of the cluster (sq.km)	Weighted accessibility index
1	1135	1709	591	118	175	4954
2	153	238	49	591	146	625
3	525	555	92	425	277	2267
4	176	257	57	332	161	1784
5	98	144	44	200	169	457
6	270	382	84	164	287	1510
7	19	32	2	331	48	54
8	36	60	3	56	73	84
9	47	81	10	93	140	153
10	37	67	9	155	113	151
11	36	64	6	124	135	99
12	84	129	22	142	353	227
13	94	155	20	326	743	272
14	76	118	32	467	483	518
15	22	37	8	319	215	47
16	46	68	35	129	419	397
17	127	184	41	193	740	425
18	91	146	57	447	405	385
19	211	305	44	337	1112	463
20	76	129	38	701	400	307
21	72	111	17	285	693	222

different clusters must be calculated. The Transport Network Density (TND) is used to calculate the development of a cluster's transport network. The higher density values indicate a higher development of a network. The transport network's density was calculated using Eq. 7.

TND = *Transport Network's Length (km) / Area (sq.km)* (7)

The descriptive statistics of the parameters required to compute the transport network's connectivity, accessibility, maturity, and development are given in Table 1.

3.3 Categorization of the Structural Evaluation Criteria of the Transport Network (TNSEC)

The values are normalized to a scale of 0 to 10 after the computation of various structural evaluation criteria of the transport network for different clusters. There are five categories of the transport network's connectivity, accessibility, maturity, and development. The clusters are then classified based on the categorization proposed in Table 2 based on their levels of the transport network's connectivity, accessibility, maturity, and development.

Tab. 2 *Categorization for the Level of the Structural Evaluation Criteria of the Transport Network*

Range of ATS, AI, FD and TND	Level of connectivity, accessibility, maturity, and development
0.00 – 2.00	Very Low
2.01 - 4.00	Low
4.01 – 6.00	Medium
6.01 - 8.00	High
8.01 – 10.00	Very High

3.4 Development of the Structural Performance Index of the Road Network (RNSPI)

The present study proposed a Road Network Structural Performance Index (RNSPI) in order to identify the quality of the transport networks in the HMA. RNSPI is the sum of all the normalized values of the Aggregate Transportation Score (ATS), Accessibility Index (AI), Fractal Dimension (FD) and Transport Network Density (TND). A higher value of the RNSPI indicates the excellent performance of the transport network in the HMA. The RNSPI of different clusters in the HMA is computed using Eq. 3.12.

$$RNSPI = ATS + AI + FD + TND \quad (8)$$

The RNSPI values indicate the performance standards of the transport network in each cluster of the HMA. The transport network's structural performance in the HMA is classified into five categories: very *weak, weak, average, good* and *very good* based on the RNSPI values; the ranges are presented in Table 3. These values help identify the clusters with weak

transport networks so that measures can be taken to implement better planning practices to improve the network's performance.

Tab. 3 *Categorisation of the Level of the Road Network's Structural Performance*

RNSPI Range	Level of performance
0-8	Very Weak
9-16	Weak
17-24	Average
25-32	Good
33-40	Very Good

4 RESULTS AND DISCUSSIONS

According to the empirical procedures described in the previous section, the transport network in different clusters of the study area was evaluated with respect to different RNSEC. The transport network structure in the clusters was classified into five categories based on connectivity, accessibility, maturity, and development: *very low, low, medium, high, and very high*. Figure 5 depicts the level of the transport network's connectivity, accessibility, maturity, and development in various HMA clusters.

The highest values of the ATS, accessibility index, fractal dimensions, and density values are noted in Cluster 1. The transport network in Clusters 7 and 15 have very low degrees of connectivity and accessibility. The transport network in Cluster 8 has very low maturity. The transport network's density values are very low in Clusters 16 and 21. The lower connectivity values are due to smaller links available in a particular cluster. If there are fewer links, the direct route options to the users decrease, which lowers the network's connectivity. The very high accessibility index in a particular cluster is due to the higher availability of utilities like hospitals and schools, which are given more weightage. The transport network's maturity is higher in clusters with more coverage of the transport network. The transport network's development is less in clusters having very low transport network density values, there by indicating the lack of compactness of the transport network.

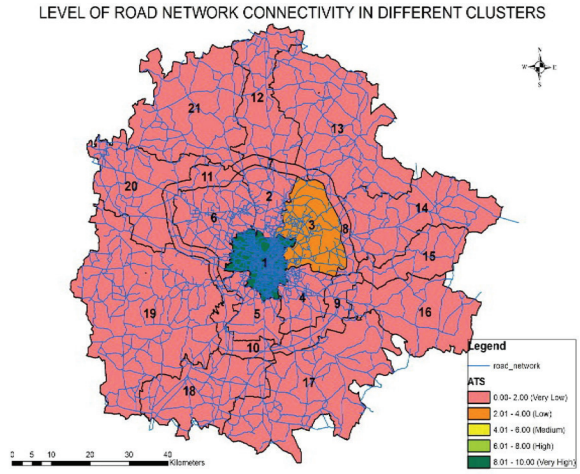

(a) *Level of road network's connectivity*

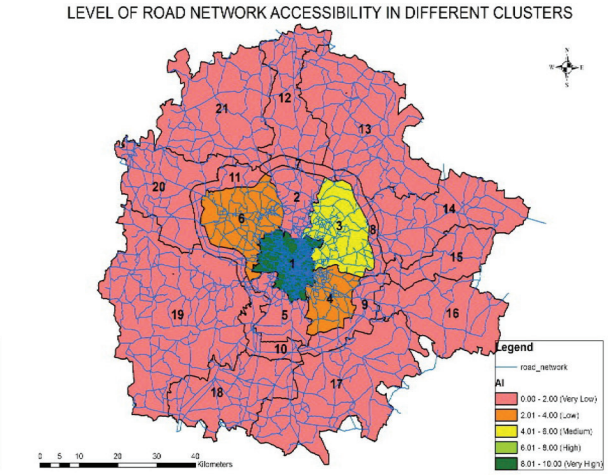

(b) *Level of road network's accessibility*

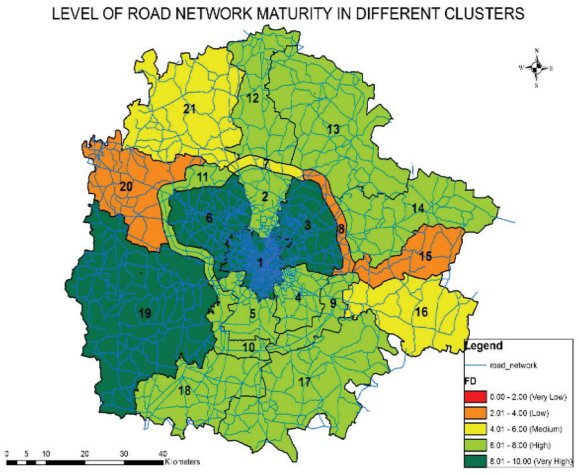

(c) *Level of road network's maturity*

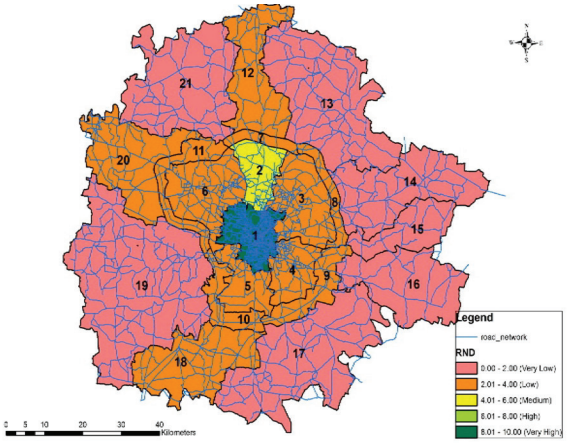

(d) *Level of road network's development*

Fig. 5 *Level of road network's structure (a) connectivity, (b) accessibility, (c) maturity and (d) development*

4.1 Structural Performance Index of the Road Network (RNSPI)

The HMA urban transport network structure was evaluated for different aspects such as its connectivity, accessibility, maturity, and development in the previous sections. The evaluation of the transport network results indicates that the transport network in some locations and clusters has low connectivity and high accessibility, very high maturity and average development, very low maturity, and high accessibility. That is due to different structural evaluation criteria which were based on different transport network structural components. Therefore, to understand the overall performance standards of the transport network in a particular location or cluster, a Road Network Structural Performance Index (RNSPI) has been developed. RNSPI is an integrated measure of four structural evaluation criteria of an urban transport network. The higher value of RNSPI indicates the excellent performance of the transport network in the study area. The transport network's structural performance level of each cluster is evaluated based on the categorization of the RNSPI values provided in Table 2 and is presented in Figure 6.

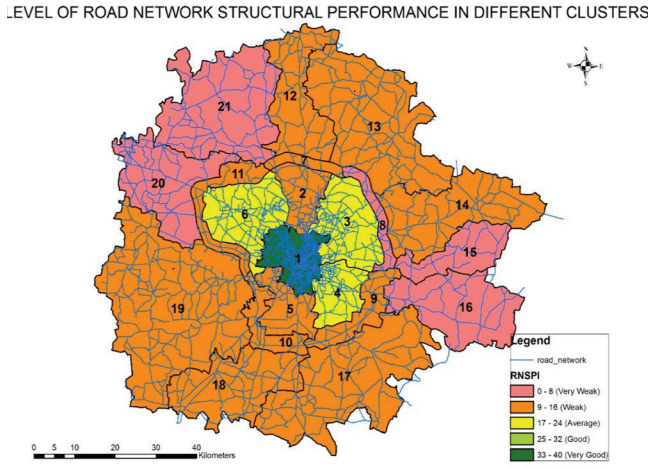

Fig. 6 *Level of road network's structural performance in different clusters*

Figure 6 presents the clusters in different colors falling under five different ranges of RNSPI values. The clusters are shown based on their levels of the transport network's structural performance. It also indicate that RNSPI values are higher for the clusters present in the central region of the city, when compared to the clusters away from the center of the city.

5 CONCLUSIONS

The following are the methodological conclusions drawn from the present study:

1. The study proposed a methodology for a comprehensive analysis of the road network structure in a city that involves the evaluation and modelling of different variables with reference to a specific case study of the Hyderabad Metropolitan Area (HMA). The methodology is applicable to similar cities.
2. The clusters occupying the central region of the city have high road network connectivity, accessibility, maturity and development versus the locations and clusters away from the central part of the city. The development authority, can promote the optimization of the different structural evaluation criteria of the road network by adding links and locating different types of opportunities wherever necessary. This improves the uniformity of the road network's structural growth in the entire city. The balance in the growth of the development in the city has many benefits, like reducing congestion on major arterials, trip lengths, travel time, and environmental degradation.
3. The categorisation of the road network's structural evaluation criteria proposed in the study is useful for interpreting the level of road network's connectivity, accessibility, maturity and development in a city. This categorization provides a base for the development authorities in understanding the locations where there is a need for improvement with respect to each criterion.
4. The Road Network Structural Performance Index (RNSPI), developed in the study is an analytical measure for comprehending the overall road network's structural performance. This index presents the locations where there is a need for the improvement in the network's structure to the development authorities.

The following are the case-specific conclusions drawn from the study:

1. According to the study, the transport network in Cluster 1 has higher levels of connectivity, accessibility, maturity, development, and structural performance for the overall transport network. According to the study, all of the transport network's structural evaluation criteria are high in clusters occupying the city's central region when compared to the peripheral clusters.
2. According to the study, the network facilities are concentrated in clusters located in the city center and decrease as one moves away from the center of the city. It demonstrates the non-uniformity in the development of the transportation network's structural facilities throughout the city, which may be due to a lack of proper planning during the early stages of the city's development. The road network in the city of Hyderabad requires a balance between the availability of direct routes, urban services, built-up areas and a dense road network to optimise the growth of the transport network in the city.
3. The study also demonstrated the utility of Arc GIS software in assessing the structure of an urban transport network with regard to connectivity, accessibility, maturity, and development.

The present study is limited to an analysis of the existing structure of the road network in the study area; the operational features of the network were not considered. The study is also limited to an analysis of the clusters of the city of Hyderabad. Future studies can be carried out in cities with similar road network characteristics by adapting the methodology proposed in the present study. The dynamic features of the road networks' such as traffic flow, speed, capacity, etc., should be considered in future studies and structural measures to provide an overall understanding of the road network conditions in a study area.

REFERENCES

Adwani, M. - Srirama, B. and Pathan, S.K. (2005). Improvement in transit service using GIS – case study of Bhavnagar State Transport Depot. In *Proceedings of ESRI National Conference 2005, NOIDA*, India.

Ahmed, M.E.I. Geneidy and David, M. Levinson. (2006). Access to destinations: Development of accessibility measures. Minnesota Department of Transportation, MN, USA.

Arora, A. and Pandey, M. K, (2011). Transportation network model and network analysis of road networks. *12th Esri India User Conference* 2011.

Batty, M. and Longley, P.A. (1994). Fractal Cities: Geometry of form and function, Academic Press.

Batty, M., and Xie, Y. (1996). Preliminary evidence for a theory of the fractal city. *Environment and Planning A*, 28, 1745–1762.

Ben-Avika and Lerman. (1977). Disaggregate travel and mobility choice models and measures of accessibility. Behavioural Travel Modelling, eds. Hensherd and Stopher, P., London: Croom Helm, pp: 654-679.

Bento, A.M. - Cropper M.L. - Mobarak A.M., and Vinha, K. (2003). The impact of urban spatial structure on travel demand in the United States. *World Bank Policy*, 2003, Research Paper No. 3007.

Bhat, C. - Handy, S. - Konckelman, K. - Mahmassani, H. - Chen, Q. - and Weston, L. (2000). Urban Accessibility Index: Literature review. Research Report TX 01/ 7-4938-01, Texas Department of Transportation, TX, USA.

Burns, L.D. (1979). Transportation, Temporal and Spatial Components of Accessibility. Lexington, MA: Lexington Books.

Copper, J.C. - Watkinson, D., and Oskrochi, R. (2010). Fractal analysis and perception of visual quality in everyday street vistas, *Environment and Planning B: Planning and Design*, Vol. 37, pp: 808-822.

Dalvi, M.Q. and Martin, K.M. (1976). The measurement of accessibility: Some preliminary results. Transportation, Vol.5, pp.17-42.

De Cola, L. - Lam, N. (1993). Introduction to fractals in geography. Fractals in Geography (Prentice-Hall, Englewood Cliffs, NJ, USA) pp: 3-22.

Dheenadayalu, B. - Wilshon, and Wilmot, C. (2004). Analysis of link capacity estimation methods for urban planning models, Journal of Transportation Engineering, Vol 130, pp: 268-275.

Dill, J. (2004). Measuring network connectivity for bicycling and walking. Joint Congress of ACSP-AESOP.

Falconer, K. (2004). Fractal geometry: mathematical foundations and applications, Wiley.

Falconer, K.J. (1986). The geometry of fractal sets, Cambridge University Press.

Frankhauser, P. (1992). Fractal properties of settlement structures. In First International Seminar on Structural Morphology.

Gattuso and Miriello. (2005). Compared analysis of metro networks supported by Graph Theory, Networks and Spatial Economics, Vol. 5, No. 4.

Ghosh, S. (2016). Spatial pattern of road transport connectivity in Puncha block, Puruliya District, West Bengal. Indian Journal of Spatial Science, 7(1), 42–47.

Hansen, W. (1959). How accessibility shapes land use. Journal of the American Institute of the Planners, 25, 73–76.

Hanson, S. (1986). The Geography of Urban Transportation. New York: Guilford.

Hastings, H.M. and Sugihara, G. (1993). Fractals. A user's guide for the natural sciences. Oxford Science Publications, Oxford University Press, New York, 1993, 1.

Ingram, D.R. (1971). The concept of accessibility: A search for an operational form. Regional Studies, Vol.5, pp.101-107.

Kansky, K.J. (1963). Structure of transportation networks: relationships between network geometry and regional characteristics. University of Chicago, Dept. Of Geography.

Kumar, P., and Kumar, D. (2016). Network Analysis using GIS Techniques: A Case of Chandigarh City, *International Journal of Science and Research (IJSR),* Vol. 5, No. 2, pp: 409-411.

Lean, W., and Goodall, B. (1977). Aspects of land economics. London: The Estate Gazette Ltd., 135-141.

Levinson, D. (2012). Network Structure and City Size. *PLOS ONE Journal*, 7(1):e29721. DOI:10.1371/journal.pone.0029721, 2012.

Litman, T. (2021). Evaluating accessibility for transport planning, Victoria Transport Policy Institute, https://www.vtpi.org/access.pdf.

Mackiewicz, A. and Ratajczak, W. (1996). Towards a new definition of topological accessibility. Transportation Research, Part B, Vol. 30 (1), pp. 47-79.

Mandelbrot, B.B. (1977). Fractals: Form, Chance, and dimension. San Francisco: WH Freeman & Co.

Mandelbrot, B.B. (1982). The fractal geometry of nature. 1982. WH Freeman & Co.

Marshall, S. (2005). Streets and patterns. New York, Spon Press.

Mohammadi, A. - Rao, K.M.L, and Baseer, M.A.K. (2013). Fractal view policy development on road infrastructure in urban areas. International Journal of Earth Sciences and Engineering, Volume 6, No.4 (01).

Nalawade, D.B. - Kashid, S.D. - Dhumal, R.K. - Nagne, A.D., and Kale, K.V. (2015). Analysis of Present Transport System of Aurangabad City Using Geographic Information System, *International Journal of Computer Sciences and Engineering*, Vol 3, No. 6, pp: 124-128.

Nijagunappa, R. - Shekhar, S. - Gurugnanam, B. - Raju, P.L.N. and De, P. (2007). Road Network Analysis of Dehradun City Using High-Resolution Satellite Data and GIS. *Journal of the Indian Society Of Remote Sensing*, Vol. 35, No. 3.

Pietgen, H.O. and Saupe, D. (1988). The science of fractal images. In. Springer-Verlag, NY.

Purevtseren, M. - Tsegmid, B. - Indra, M. - and Sugar, M. (2018). The fractal geometry of urban land use: the case of Ulaanbaatar city, Mangolia, *Land*, 7, 67.

Rodin, V. and Rodina, E. (2000). The fractal dimension of Tokyo's streets. Fractals, 8, 413-418.

Santosa, W. and Basuki, T.J. (2005). An evaluation of road network performance in Indonesia, Proceedings of Eastern Asia Society for Transportation Studies, Vol. 5, pp: 2418-2433.

Schlosser, T. - Schlosser, P. - Zuzulová, A. - Cápayová, S. - Bálint, G. (2022). Traffic Planning as a Preliminary Tool in Project Documentation for BIM. Buildings 2022, 12, 381. https://doi.org/10.3390/buildings12030381.

Scott, D.M. - Novak, D. - Aultman-hall, L. and Gua, F. (2005). A new method for identifying critical links and evaluating the performance of transportation networks. In working paper series 009 of Center for Spatial Analysis, McMaster University, Hamilton, Ontario, Canada.

Scott, D.M. - Novak, D. - Aultman-Hall, L. and Gua, F. (2006). Network robustness index: A new method for identifying critical links and evaluating the performance of transportation networks, Journal of Transport Geography, Vol. 14, pp: 215-227.

Shen, G. (1997). A fractal dimension analysis of urban transportation networks. Geographical and Environmental Modelling, 1, 221-236.

Sreeleka, M. G. - Krishnamurthy, K., and Anjaneyulu, M.V.L.R. (2017). Fractal assessment of road transport system. *European transport/ Transporti Europei*, No. 65, paper No. 5.

Sreelekha, M. G. - Krishnamurthy, K., and Anajaneyulu, M. V. L. R. (2020). Urban road network and its topology: A case study of Calicut, India. European Transport / Trasporti Europei, No. 78, Paper No. 6, ISSN 1825-3997.

Sun, Z. - Jia, P. - Kato, H., and Hayashi, Y. (2007). Distributive Continuous Fractal Analysis for the Urban Transportation Network. *Journal of the Eastern Asia Society for transportation studies*, Vol. 7.

Wang, J. - Jin, F. - Mo, H., and Wang, F. (2009). Spatiotemporal evolution of China's railway network in the 20th century: An accessibility approach, Transportation Research Part-A, Vol. 45, pp:765-778.

Wee, B.V. - Hagoort, M., and Anne, J.A. (2001). Accessibility measures with the competition. Journal of Transport Geography, 9, 199-208.

Wu, Y.H. and Miller, H.J. (2002). Computational tools for measuring space-time accessibility within transportation networks with dynamic flow. Journal of Transportation Statistics, Vol.4, No.2/3, pp: 1-14.

Xie, F. (2005). The evolution of road networks: A simulation study based on network degeneration, Master's thesis, University of Minnesota at Twin Cities, USA.

Xie, F., and Levinson, D. (2007). The topological evolution of road networks, Presented at Transportation Research Board (TRB) in Washington, DC.